ACADEMY OF SCIENTIFIC AND INNOVATIVE RESEARCH

Exploring Membrane Materials for High Temperature Fuel cell Applications from Quantum Chemical Calculations and Molecular Simulations

by

Swagata Pahari
Registration Number: 10CC11A26012

Under the Guidance of

Dr. Sudip Roy

Dr. Kumar Vanka

A thesis submitted in partial fulfillment for the degree of Doctor of Philosophy

in the

Chemical Sciences

CSIR-National Chemical Laboratory

August 2015

Certificate

This is to certify that the work incorporated in the Ph.D. thesis entitled **" Exploring Membrane Materials for High Temperature Fuel cell Applications from Quantum Chemical Calculations and Molecular Simulations"** submitted by Ms. Swagata Pahari to Academy of Scientific and Innovative Research (AcSIR) in fulfillment of the requirements for the award of the Degree of **DOCTOR OF PHILOSOPHY**, embodies original research work under our guidance. We further certify that this work has not been submitted to any other University or Institutions on part or full for the award of any degree or diploma. Research material obtained from other sources has been duly acknowledged in the thesis. Any text, illustration, table, etc., used in the thesis from other sources, have been cited and acknowledged.

Signed:	Signed:	Signed:
Swagata Pahari	Dr. Sudip Roy	Dr. Kumar Vanka
(Research Fellow)	(Research Supervisor)	(Research Co-Supervisor)
Date:	Date:	Date:

Physical and Materials Chemistry Division
CSIR-National Chemical Laboratory
Pune-411008.

ACADEMY OF SCIENTIFIC AND INNOVATIVE RESEARCH

Abstract

Chemical Sciences
CSIR-National Chemical Laboratory

Doctor of Philosophy

by Swagata Pahari

This thesis presents research investigation carried out with motivation of developing potential polyelectrolyte membrane material, having better proton conductivity than existing materials, for high temperature fuel cell. Proton transport in a polyelectrolyte membrane is essential for fuel cell applications. Proton transfer through the membrane occurs via two mechanisms: i) Grotthuss mechanism in which proton hops along the hydrogen bonding network, occurs in picosecond time scale. ii) vehicular mechanism in which proton carrier diffuses in between hops, occurs in nanosecond times scale. Therefore, to accurately characterize the proton transfer process and the structure of the hydrogen bonding network, we have used multiscale modeling techniques which include quantum mechanics, *ab initio* molecular dynamics (MD) and classical MD.

Poly [2, 2′-(p-Phenylene)-5, 5′-bibenzimidazole (PBI) and poly(2, 5 Benzimidazole) (ABPBI) doped with phosphoric acid are considered as potential polymer electrolyte membrane for high temperature fuel cell. Phosphoric acid acts as proton conducting media and PBI or ABPBI gives the mechanical stability to the membrane. In first two working chapters (chapter 3 and 4) of the thesis, classical MD simulations are performed to study hydrogen bond network formation and vehicular motion properties of phosphoric acid (PA) doped monomer (BI) of PBI. The effects of PA doping level are evaluated. The results indicate several types of hydrogen bond formation between BI and PA. Highly ordered hydrogen bonding network, which can restrict the intramolecular motion are observed to form in the BI-PA systems. Bridging hydrogen bonds are found which reduce the mobility of the system constituents which in turn decreases the diffusion of BI as well as PA. Structural heterogeneity is found to be entirely responsible for the heterogeneous dynamics of membrane constituents (BI and PA) which is quantitatively estimated in this thesis. We have then extended our study from monomer to polymer system. To understand the influence of different polybenzimidazole structures on PA uptaking capacities, we present comparative structural and conformational properties of two most investigated polybenzimidazoles (PBI and ABPBI) in presence of PA

using classical MD in chapter 5. The results reveal that PA doped ABPBI is more elongated compared to PA doped PBI. The conformations of PA solvated PBI and ABPBI are observed to be significantly different. The structural arrangement of PA molecules are found to be distinguishable for ABPBI and PBI. PA forms more number of hydrogen bonds per benzimidazole moiety along the ABPBI chain than PBI. This explains why PA absorbing capacity of ABPBI is more than PBI. Some PA molecules are found to form hydrogen bonds with two adjacent benzimidazole moieties in case of ABPBI which is absent in PBI. This type of sharing hydrogen bonds give rigidity to ABPBI which attributes to the mechanical strength of the chain. These conformational and structural properties of ABPBI and PBI chains provide insight to explain the experimental findings about proton conduction.

Since classical MD can not deal with bond breaking and making phenomenon, in chapter 6, *ab initio* MD has been performed to understand the proton transport mechanism in PA-imidazole mixture. The role of triazole in proton transfer is also explored while it is doped with PA or PA-imidazole mixture. The results indicate that proton conductivity of the membrane increases in presence of triazole. Quantitative estimation of the structural diffusion and vehicular motion of protons reveal that upon addition of triazole in PA and PA-imidazole mixture, structural diffusion increases significantly. The mechanism of proton transport is found to be different in presence of triazole. Constructive and non-constructive paths for structural diffusion are identified which contribute to long and short range proton transfer respectively. The study suggests that PA doped triazole is a better proton conductor compared to PA doped imidazole.

In our final working chapter (chapter 7), a large number of N-containing aromatic heterocyclic compounds are explored in search of a promising membrane material. Using density functional theory based quantum mechanical methodologies, gas phase proton affinity, interaction energy and proton transfer activation energy barriers are calculated for these compounds in presence of PA. The possibility of back and forth proton transfer and stability of the systems are revealed from these properties. In this study, 1,2,3-triazole-1H, 1,2,4-triazole-4H and oxazole are found to be promising membrane materials.

Acknowledgements

The research work discussed in this thesis has been kept in track and seen through to completion with the encouragement and support of numerous people including my friends, colleagues and well wishers. It is a pleasant task to express my thanks to all those who contributed in various ways to the success of this research and made it an unforgettable memory for me.

First of all, I would like to express my sincere gratitude to my supervisor, Dr. Sudip Roy, for his support and guidance and encouragement throughout my research carrier. I would like to thank him for giving me independence and freedom in my research work. His nobel ideas always influenced me. Under his guidance, I have successfully overcome many difficulties and learned a lot.

I am also grateful to my co-guide, Dr. Kumar Vanka for his valuable suggestions and insightful discussions which enriched my Ph. D. work.

I thank my doctoral advisory committee members, Dr. Neelanjana Sengupta, Dr. Ashish Orpe, Dr. Pankaj Doshi for their constructive comments during the process of evaluation. Their hard questions helped me to widen my research from various perspectives.

I have been blessed with a friendly and cheerful group of colleagues who provided me a nice working environment. I am thankful to Mr. Prithvi Raj Pandey, Mr. Souvik Chakraborty, Mr. Sujit Sarkar, Mr. Anil Mahshal and Mr. Subhadip Das for the stimulating scientific discussions, for the sleepless nights we were working together before deadlines and for all the fun we had in the last five years. I had a nice experience of working with Mr. Santu Biswas. I thank Mrs. Sheelan Sengupta, Mr. Bappa Ghosh, Mr. Nilesh Choudhury, Ms. Pragti Sharma and Ms. Prajakta Nakate for their encouragement. A special thanks to Mr. Chandan Kumar Choudhury for many scientific and nonscientific discussions. Thanks for guiding me through hard times and always motivating me. In many ways, I have learnt much from him.

I take this opportunity to thank all the faculty members of Student Academic Office (SAC) for their help and support. Thanks to Ms. Deepa and Mrs. Kohle Ma'am for their continious help in official documentations .

I thank Dr. Sarika Maitra Bhattacharyya and Dr. Sourav Pal for their classes on statistical mechanics and quantum chemistry. It was very helpful throughout my Ph. D work.

I would like to express huge, warm thanks to my roommates, Nivedita di, Debarati Di and Veena for their valuable help and constant support. I am thankful to them for many

scientific and non-scientific discussions and many things impossible to mention. They have always given me confidence to take up challenges. Thanks for many unforgettable memories and making my stay memorable which I will cherish forever. I am thankful to Kamalika to be by my side during my difficult years and constantly supporting me. Thanks to Sutapa di for encouraging me.

I would like to thank my parents and brother for their encouragement, support and attention. Their support and care helped me to stay focused on my research.

Contents

[1]This chapter is adapted from the publication Swagata Pahari, Chandan Choudhury, Prithvi Raj Pandey, Minal More, Arun Venkatnathan, S. Roy, Molecular Dynamics Simulation of Phosphoric Acid Doped Monomer of Polybenzimidazole: A Potential Component of Polymer Electrolyte Membrane of fuel cell, J. Phys. Chem. B, 116 (2012) 7357

[2]This chapter is adapted from the publication Swagata Pahari and S. Roy, Evidence and Characterization of Dynamic Heterogeneity in Binary Mixtures of Phosphoric Acid and Benzimidazole, J. Chem. Phys., 2013, 139, pp 154701-154706

List of Figures

List of Tables

Dedicated to my parents...

Chapter 1

Introduction

Energy is essential for sustaining global socio-economic development. Therefore, global interests are drawn towards power generation. Today major source of energy comes from fossil fuels which are non-renewable source and limited on earth. Besides, these fossil fuels emit CO_2 on burning, which is responsible for increasing global temperature. [1] Therefore, the world-wide concern is about replacing the fossil fuel by renewable, carbon-free energy source. Fuel cells appeared as a good replacement for energy source with higher efficiency and environmental protection. [2–5] Polyelectrolyte membrane fuel cell (PEMFC) technology particularly offers reliable power generation to a wide range of stationary, portable and transport applications. The polymer electrolyte membrane (PEM) is an important constituent of PEMFC. It plays a crucial role in determining the efficiency of a PEMFC by selectively transporting protons from anode to cathode. Therefore, researches are going on to find a promising polyelectrolyte material to be used as a membrane in PEMFC. Taking into consideration some economical challenges such as production and storage of fuel, water-thermal management, fast electrode kinetics, and increased tolerance to impurities in the PEMFC system, increasing attention is drawn for choosing membranes, which can function at high temperature. For designing potential membrane operating at high temperature PEMFC, researchers examined a varieties of polymer materials which show high proton conductivity and good mechanical strength with the inclusion of acid in the polymer matrix at elevated temperature. The polymer materials based on N-containing aromatic heterocyclic compounds such as imidazole, triazole, pyrazole etc are found to be particularly efficient membrane in presence of phosphoric acid (PA) as a solvent. However, experimental studies on PA doped N-containing aromatic heterocyclic compound based polymers leave many questions unanswered such as nanostructure of the membrane, dynamics of proton and solvent and so on. This is because proton transfer, rearrangement of the solvent proton network and polymer dynamics occurs on different length and time scales. Therefore, multiscale

simulation techniques including density functional theory (DFT) based quantum mechanical (QM) methodologies for calculating quantum chemical properties which govern proton transport (PT) events, *ab initio* molecular dynamics (MD) to accrately model the PT mechanism, classical MD for understanding the hydrogen bonding (H-bonding) network formation which serves as PT path in the membrane, coarse-graining to model the large scale morphology of PEM, are essential to use. Based on such understandings, PEM can be modified by tuning polymer chemistry, adding substituents or dopant to the system. In this way, computational studies assist in designing the potential membrane. These studies can also be integrated with experiment in a feedback loop to improve the efficiency of fuel cell. Therefore, in this thesis, we have used various computational techniques (DFT based quantum chemical calculations, *ab initio* MD, classical MD) in order to understand the structural and dynamical properties of the PEM, accurately predict the PT mechanism and to design new PEM material with improved proton conductivity compared to existent materials.

1.1 Fuel cell

Sir William Grove in 1839 introduced the first fuel cell technology though no practical use was found for another century. Thereafter, a large amount of work had been done on fuel cell to enhance its efficiency and reduce its cost. [5–8] Considering the environmental safety, major advantage of fuel cell is that it can operate on various types of carbon-free fuels like hydrogen, methanol etc and emits no pollutants. [9, 10] New technology can enhance the saving of fuel. Besides, relative to batteries, it has higher energy densities. In recent times, fuel cells are being investigated extensively as a potential power source for automobiles and stationary applications. [11–13] But there are still many market and technical issues to be overcome. Many challenges are still in progress to improve the durability, performance and reduce the cost which are necessary to commercialize the fuel cell.

1.1.1 Characteristics of fuel cell

Fuel cell is an electrochemical device that transforms chemical energy of the fuel to electrical energy for generating power. The advantage of fuel cell over batteries is that it can provide power as long as fuel is supplied. Fuel cell consists of three parts: i) cathode (positive electrode), ii) anode (negative electrode) and an electrolyte membrane in between the electrodes. Fuel cell has following characteristic features which makes it a potential alternative to energy conversion system:

High efficiency: Fuel cell directly converts chemical energy to electrical energy. Therefore, the performance of fuel cells are not limited by Carnot cycle. Hence, these are more efficient than combustion engine. [14] The present fuel cell plants are 50-60 % efficient whereas hybrid fuel cell/gas reheat turbines are more than 70 % efficient. [15] Considering the fuel cell car, if the fuel is H_2, it can be upto 64 % efficient. Honda's FCX concept vehicle was reported to be 60 % energy efficient.

Low CO_2 emission: Fuel cell operated on H_2 fuel emits only water as by-product, no pollutant. [16] However, some stationary fuel cells, where hydrocarbon or natural gas is used as fuel, emit small amount of CO_2, CO, NO_x, SO_x etc. But these are significantly lower in amount compared to what are emitted from internal combustion engine.

Fuel flexibility: Fuel cell in most of the cases use H_2 as fuel where source of H_2 does not matter. A reformer is present in the fuel cell to generate H_2 from a wide range of fuel sources such as methanol, ethanol, propane, natural gas. [17, 18]. H_2 produced from electrolysis of water is known to be the cleanest fuel pathway. Fuel cell continues to generate power as long as fuel is supplied.

Silent operation: Fuel cell operates silently compared to internal combustion engine. Therefore, it can be used in hospital, academic institutions where noise pollution must be controlled.

Energy security: Fuel cell does not require standard fuels for example oil or gas. Therefore, economic dependence on oil producing countries are reduced. As a result, user country gets higher energy security.

Low maintenance cost: Due to the presence of very few moving parts in the fuel cell, it requires minimum maintenance and which in turn minimizes the downtime of the system.

Scalability: Fuel cells can be scaled up or down depending on the power needs, ranging from few watt to multi-megawatt. Therefore, it can serve as a power source in a wide range of applications for example smaller one at residential, telecommunications etc and larger one at vehicles, large power plants.

Reliability: In recent times, the need of highly reliable power source is almost everywhere. Stationary fuel cells are used to generate power at the place of use which generate decentralized stable power grid. On the other hand, since H_2 can be produced anywhere where water supply is provided, production of fuel can be distributed and need not to be grid-dependent.

Cogeneration application High temperature operation of fuel cell produces heat in addition to electricity which can be used to cogeneretion applications for example in residential use.

1.1.2 Applications of fuel cell

Fuel cells are used in a wide range of applications as discussed below due to its scalability, flexibility and simplicity. [19]

Transport Due to the increasing alarm of global warming, scientists are concerned about it's impact on surrounding environment. In this scenario, fuel cell is one of the best choice as it addresses environmental issues by reducing the CO_2 emission, not compromising the power supply and fuel economy. Fuel cell provides power to a wide range of vehicles including buses, trains, trucks, ferries, small boats, light aircraft, scooter etc. Fuel cell car is being of limited use till date due to it's high cost. However, automakers are trying to commercialize their fuel cell car in near future when the price of these cars will be comparable to diesel-driven car. Considering the fuel cell buses, Japan, Europe, Canada, USA successfully launched it though the high cost issue is the barrier for widespread acceptance.

Stationary Other than transports, fuel cells are widely used for stationary applications. For example, it produces electricity and heat for small as well as large scale applications. These fuel cells are sized to provide power ranging from 0.5 kW to 5 MW. Considering the low power stationary applications, fuel cells are used in telecommunication sectors, construction department, emergency residential use. One of the advantage of fuel cell is that it also generates heat in addition to electricity. Therefore, the overall efficiency of the fuel cell increases by using this heat in several other applications. High temperature operated fuel cells are used in large scale applications where it generates multi megawatt unit powers.

Portable Portable fuel cells are made in the purpose of charging up products which can be moved. Portable products include military applications, various small and large electronics for personal use e.g., mobile, torches, mp3 player, cameras, laptops, printers etc. Portable fuel cell generates power in range of 5 W - 500 KW. The advantages of fuel cell that drive the portable applications are short starting time, longer run-time, rapid recharging, low weight, reliability and off-grid operations.

Military Various fuel cells are used as power generation engine in military camp. Less amount of fuel is needed to operate fuel cell compared to any combustion engine. Therefore, soldiers required to carry the fuel tank into the battlefield are reduced in number

which motivated military department to use fuel cell. The high efficiency, silent operations and longer runtime make the fuel cell a potential power generation system for marine operations.

Space Fuel cell was first used in the space mission in 1960s. It provided electrical energy and also drinking water throughout the mission. The high efficiency, light weight and flexibility make it a better choice compared to combustion engine or battery for short time operation of the mission. Regenerative fuel cell system was also used to store energy on the space station. Researchers are now trying to use the same concept in Moon and Mars missions.

1.1.3 Classifications of fuel cell

Fuel cells are classified according to the electrolyte it uses for proton conduction. There are five leading types of fuel cells:

i) Molten carbonate fuel cell (MCFC) MCFC uses molten carbonate salt solution as an electrolyte suspended in a ceramic matrix, usually $LiAlO_2$. Commonly used salts are Lithium or Potassium carbonate. This type of fuel cell operates at high temperature ($\sim 650°C$). The half-reaction in MCFC at anode and cathode are as follows:

$$Anode : H_2 + CO_3^{2-} \longrightarrow H_2O + CO_2 + 2e^- \tag{1.1}$$

$$Cathode : 1/2O_2 + CO_2 + 2e^- \longrightarrow CO_3^{2-} \tag{1.2}$$

MCFC is used in huge stationary power production for example power plants of megawatt capacity. However, one of the disadvantage of this type of fuel cell is that it uses liquid rather than solid electrolyte. Besides, CO_2 needs to be injected at cathode as CO_3^{2-} is consumed at cathode.

ii) alkaline fuel cell (AFC) An AFC uses alkaline electrolyte as membrane, in most of the cases, potassium hydroxide (KOH) aqueous solution. The operating temperature of this type of fuel cell is in between 150-200°C. Pure H_2 is used as fuel. The half reactions occur in AFCs are as follows:

$$Anode : H_2 + 2OH^- \longrightarrow 2H_2O + 2e^- \tag{1.3}$$

$$Cathode : 1/2O_2 + H_2O + +2e^- \longrightarrow 2OH^- \tag{1.4}$$

There must be continuous supply of electrolyte to compensate the evaporation due to the high temperature operation of the system. As a result, OH^- groups are continuously

transported from anode to cathode which in turn governs the electronic charge flow in AFC.

iii) phosphoric acid fuel cell (PAFC) PAFC uses phosphoric acid aqueous solution, a promising proton conducting medium, as electrolyte. These cells operate at moderately higher temperature (150-200°C). Half-reactions at anode and cathodes are:

$$Anode : H_2 \longrightarrow 2H^+ + 2e^- \tag{1.5}$$

$$Cathode : 1/2O_2 + 2H^+ + 2e^- \longrightarrow H_2O \tag{1.6}$$

This type of fuel cells are used in stationary applications and generate power in the range of 100 KW to 400 KW. Before 2001, PAFC was most widely used across the world specially to generate power (5 MW) in large scale plants.

iv) solid oxide fuel cell (SOFC) SOFC uses a solid oxide for example zirconium oxide, yttrium oxide as electrolyte. SOFC works at very high temperature (800-1000°C), highest among all the fuel cell types. The half-cell reactions in a SOFC are:

$$Anode : H_2 + O^{2-} \longrightarrow H_2O + +2e^- \tag{1.7}$$

$$Cathode : 1/2O_2 + 2e^- \longrightarrow O^{2-} \tag{1.8}$$

Because of such high operating temperature, cell materials should be chemically and thermally resistant to circumvent corrosion and degradation issues. SOFCs are extensively used in stationary power generation. Micro SOFCs, generating power in watt range, have been developed for portable charger.

v) polymer electrolyte membrane fuel cell (PEMFC) PEMFC can use various fuels like hydrogen, methanol, formic acid etc. However, PEMFC using hydrogen as a fuel is most widely studied. In PEMFC, a solid proton conducting polyelectrolyte is used as a membrane. In this fuel cell, hydrogen, used as fuel, dissociates into proton and electron at anode. The proton is transported through the polyelectrolyte membrane whereas electron passes through the external wire which generates power to be used in automobile and stationary applications. Considering the operation of PEMFCs, like in all other fuel cells, an oxidation and a reduction reaction occurs at anode and cathode respectively. These electrochemical reactions generate potential gradient between electrodes. The electrolyte membrane placed between electrodes conducts ion and at the same time it acts as a barrier for reactant gases. The electrochemical reactions also result potential gradient for electron flow through the external circuit connected to the electrodes which serves as a source of electrical current. The electrons reach at the cathode through the external circuit. At the cathode, oxygen gets reduced in presence of

electron and combines with proton which produces water as a byproduct. The half-cell reactions at anode and cathode as well as overall cell reactions are given below:

$$Anode : H_2(g) \longrightarrow 2H^+ + 2e^- \tag{1.9}$$

$$Cathode : 1/2O_2(g) + 2H^+ + 2e^- \longrightarrow H_2O(l) \tag{1.10}$$

$$Overall\ reaction : H_2(g) + 1/2O_2(g) \longrightarrow H_2O(l) \tag{1.11}$$

Both of the reactions at electrodes take place in presence of catalyst.

The first new PEMFC was developed by General Electric in 1965, called Gemini V , which doubled the flight time compared to similar battery-powered missions. At that time it had two drawbacks: i) very high cost ii) short lifetime of the membrane used. In the late 1960s, interest grew towards the application of PEMFC outside space program and E.I. DuPont de Nemours and Company introduced a perfluorosulfonic acid based membrane (trade name naifon®). The main advantage of nafion over previously used polystyrene-based membrane was it's high resistance to oxidative degradation due to the fluorinated backbone. However, it took another decade to design the electrode so that it reduces the amount of platinum catalyst used in the PEMFC, which makes it a sustainable energy conversion engine. The present thesis demonstrates the research carried out for the development of PEMFC.

1.1.4 PEMFC components

The structure of a PEMFC and it's components are shown in Figure 1.1.

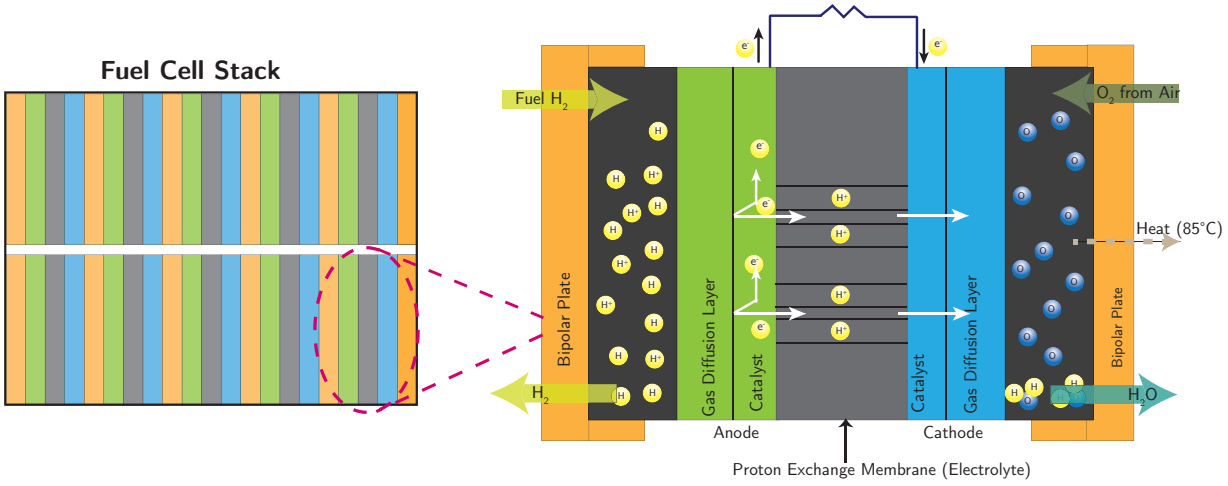

FIGURE 1.1: Schematic of PEMFC.

1.1.4.1 Electrodes

Electrodes are one of the crucial elements of fuel cell. The electrochemical reactions, responsible for generating cell working species (proton and electron), take place at the electrodes. It also maintains the potential gradient needed for charge movement through both the membrane and external load. The fuel (usually H_2) is oxidized at anode and the oxidant (usually O_2) is reduced at cathode as shown in Figure 1.1. The electrodes used in PEMFC are generally made of porous materials to take the advantage of large area to volume ratio. A catalyst layer mostly made up of platinum is coated on the inner surface of the electrodes. The catalyst enhances the rate of electrochemical reactions at electrodes by reducing the activation energies of the reactions. The high cost of catalyst makes the electrode most expensive component of PEMFC. The role of the electrodes in fuel cell are:

a) It separates H_2 and O_2 from the membrane.
b) It transports ionic species to complete the electrochemical reactions.
c) evacuates the spent fuel as well as oxidants.
d) provides the space for the electrochemical reactions to occur.

The operation at the electrodes are significantly affected by the impurities present in the fuel. Therefore, cleaning and reformation of fuel are highly needed. However, since electrodes play a vital role in the performance of fuel cell, research interests are drawn towards designing new catalyst and developing advanced manufacturing techniques for electrodes.

1.1.4.2 Electrolytes

The electrolyte is located at the center of the membrane and it separates anode and cathode as can be seen in Figure 1.1. To allow the two redox reactions to take place at two separate places (anode and cathode), the electrolyte has to separate the flow of fuels and oxidants. Besides, the electrolyte should be impermeable to electrons flowing through the external circuit. The most significant role the electrolyte plays is that it transports proton from anode to cathode where H_2 is used as a fuel. In this thesis, work is focused on the advancement of polymer electrolyte used in a PEMFC.

1.1.4.3 Gas diffusion layer (GDL)

The GDL is located in between the catalyst layer and bipolar plates (see Figure 1.1). It is generally used to provide and distribute fuel and oxidant to the electrode surfaces. It

is made up of porous materials such as carbon paper or cloth or woven paper in order to facilitate the transport of reactant species from flow channel to the catalyst layer as well as for the products from catalyst layer to flow channel. The materials used in GDL are often modified with Teflon sheet or other hydrophobic materials to avoid water saturation. The transportation occurs mostly by diffusion although convection has some role for which there must be a pressure gradient between flow channel and gas diffusion layer. GDL also acts as a media for transporting electrons and heat from catalyst layer to bipolar plate. In order to possess low resistivity towards flow of electrons, GDL must be made very thin (100-400 μm). However, the extent of porosity is limited since it reduces the conductivity. The three significant characteristics of GDL are: porosity, thickness and conductivity. Therefore, a balance of these three properties must be reached in order to maximize the performance of a fuel cell.

1.1.4.4 Polarized plates

For enhancing the output electrical power of PEMFCs, single cells, consist of electrolyte sandwiched between two electrodes, are connected in series. This arrangement is known as fuel cell stacks. The bipolar plates separate adjacent fuel cells as shown in Figure 1.1. It also ensures net flow of electrons and heats from each fuel cell unit in the stack. The roles of bipolar plates are as follows:

a) Separate individual cell units in a stack and provides structural rigidity to each single cell.
b) Deliver the reactant gases to the individual cells.
c) Remove products from the cell.
d) Conduct electrons within internal circuit which is a part of complete electrochemical reactions.

The functions suggest that bipolar plates must have high electrical conductivity, good mechanical and chemical stability and low gas permeability. Besides, since it occupies most of the portion of a PEMFC, it should be thin and light to minimize the volume and weight. The materials used for manufacturing bipolar plates are either graphite composites or metallic. The graphite plates have high electrical conductivity and good chemical stability but low mechanical strength and high gas permeability. On the other hand, metallic plates have advantage of high electrical as well as thermal conductivity, good mechanical strength and low gas permeability. However, the high acidic and corrosive environment of PEMFC lead to dissolution and corrosion of metal plates which poison the reaction environment. To avoid this limitation, protective coating layers are usually applied on the metallic bipolar plates. In these days, a composite material made

of both graphite and metallic plates is used to get the best of both the plates. The concept combines the advantages of both the plates and provides a durable, lightweight and easy to manufacture bipolar plates.

1.1.4.5 Fuel cell stack

The power output of a single PEMFC is around 0.6 - 0.7 V which is too low for practical applications. Therefore, a number of fuel cells are connected in series, resulting fuel cell stack (as shown in Figure 1.1), so that voltage of all the cells are added. Two adjacent cells in a stack are connected by bipolar plates. Two types of designs for fuel cell stack are available: monopolar and bipolar. The monopolar design of a stack has an anode-anode and cathode-cathode cell arrangement where adjacent cells are electrically isolated and share a fuel or oxidant gas flow stream. The specific arrangements of electrodes in this type of stack make it a variable voltage source. Because, a number of cells, needed for a particular voltage requirement are connected. This type of design makes the fuel cell highly robust against failures as the global stack operation would be uninterrupted even if the cell units are disconnected. However, under high current loads or when large electrodes are used, current distribution becomes uneven in the monopolar stacks. On the other hand, in bipolar stack design, the cathode-anode or anode-cathode cell arrangement, connected through bipolar plates, has high power density and low internal resistance. However, power failure of one of the cell will affect the performance of the whole stack significantly.

1.1.5 Polymer electrolyte membrane

The PEM is the heart of PEMFC. It plays a vital role by selectively transporting protons from anode to cathode which in turn determines the efficiency of the fuel cell. The PEM plays three significant roles in the fuel cell: i) acts as an electrolytic medium for PT ii) works as a support for electrode catalyst and iii) acts as a barrier for separating reacting gases for example hydrogen and oxygen in anode and cathode respectively. For satisfying these roles, a state of the art membrane material for PEMFC should fulfill the following requirements: a) high ionic conductivity b) good mechanical properties in both dry and hydrated states c) low fuel permeability d) good thermal and electrochemical stability e) low cost and long-term durability. The most commonly used and most widely characterized PEM is the nafion membrane. [20–24] However, recent PEM technology uses PA doped polybenzimidazole as a membrane. This membrane based fuel cell can operate at higher temperature. (>100°C) [25–27]

1.1.5.1 Low temperature membrane

Various kinds of polymer membranes were proposed which can be used in low temperature fuel cell (LTFC) operated below 100°C. These membranes conduct proton in presence of liquid water. [28, 29] The most investigated and widely used polymer electrolyte membrane is nafion. However, LTFCs are intolerant to CO present as a impurity in fuel. Therefore, good quality purifier is needed. The heat produced as a by-product must be removed as it can degrade the fuel cell components. [30] Hence, a complicated cooling system is needed which is cost effective. Besides, higher amount of catalyst is required to enhance the electrode kinetics at such low operating temperature. However, this type of fuel cell technology is well known and already established. Start-up time of this type of fuel cell is very fast and operating voltage is very high that favour the use of LTFC.

Nafion membrane Nafion membrane was first invented by DuPont in 1960. In recent time, it is treated as benchmark for other developed polyelectrolyte membrane performance to be used in a LTFC. Nafion is a sulfonated tetrafluoroethylene copolymer synthesized by copolymerization of perfluorinated vinyl ether monomer with tetrafluoroethylene. The chemical structure of nafion is depicted in Figure 1.2.

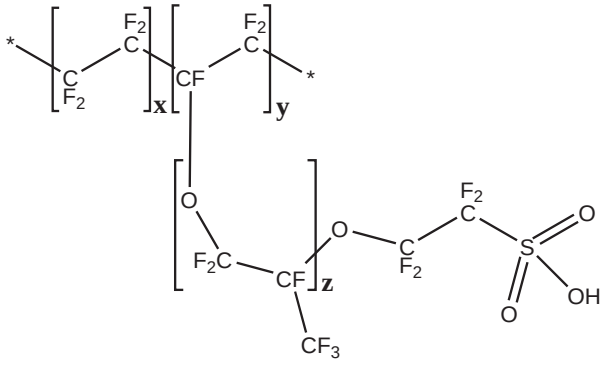

FIGURE 1.2: Chemical structure of nafion.

It has a hydrophobic backbone consists of poly(tetrafloroethylene (PTFE)) and pendant side chain terminates at hydrophilic group (sulfonate group). The hydrophobic backbone provides the polymer a strong structural integruity whereas the hydrophilic side chain plays active role in proton conduction when the membrane is hydrated. The extent of PT through nafion membrane is directly related to the hydration level. Water plays crucial role in structure formation, connecting the ionic channels, separating the hydrophobic and hydrophilic regions which in turn impact the PT. Therefore, operating temperature of nafion membrane based fuel cell is limited by boiling point of water. Above this temperature, water gets evaporated and as a result proton conductivity of the membrane

decreases which reduces the efficiency of the PEMFC. Apart from this drawback, nafion based membranes suffer from other shortcomings such as poor chemical and mechanical stability at elevated temperature, lower resistance to methanol crossover, complicated manufacturing process resulting higher cost of the membrane, electro-osmotic drag of water molecules flowing with protons from cathode to anode often causes flooding of catalyst layer at the electrode etc. Hence, external water management is necessary for nafion based PEMFC which is expensive. Therefore, to overcome these drawbacks, several attempts are made to modify the conventional polymers. For example a) using porous support materials b) doing physical or chemical treatment to modify the nanostructure of the membrane c) adding organic or inorganic compounds etc.

1.1.5.2 High temperature PEM

Currently, one of the challenge to establish the PEMFC as an alternative power source is the development of a membrane which can perform efficiently at higher temperature (above 100°C) and under external low humidification.

Neccesity for high temperature membrane High temperature operation of PEMFC has several advantages as follows:

(a) Improved electrode kinetics At high temperature, the electrode kinetics get enhanced and the catalytic activity increases.

(b) Tolerance to high impurities Carbon monoxide (CO) is generated in the fuel cell as a result of using reform liquid fuels. CO acts as a poison and competes with the H_2 for occupying the active sites on catalyst layer at anode surface at normal operating temperatures. Therefore, it is necessary to clean up fuel in order to get rid of CO content, which requires much cumbersome, larger and more cost effective system. On the other hand, the high temperature PEMFC (HT-PEMFC) can tolerate upto 30000 ppm CO and 20 ppm sulphur without degradation. Therefore, PrOx reactor, which is costly, huge and lower the system efficiency, is not required. Hence, high temperature operation of PEMFC uses simple, cheap and lightweight reformer to produce H_2 from a wide range of fuels such as methanol, ethanol, formaldehyde etc.

(c) Water management Water plays significant role in PEMFCs. The system efficiency and the overall system power depends on the water management in the fuel cell. For low temperature PEMFC (LT-PEMFC), presence of less amount of water decreases the proton conductivity of the system which in turn increases the cell resistance. On the other hand, excessive water causes 'flooding' which restricts the transport of oxygen

(O_2) through cathode. High temperature operation (>100°C) of fuel cell decreases the possibility of problems related with flooding. Besides, the conductivity of the PEM used in HT-PEMFCs does not depend on the amount of water.

(d) Heat management Effective utilization of waste heat produced is a challenge for LT-PEMFCs. Due to the small difference between ambient and the operating temperature of this type of fuel cell, a good heat removal system is required. The standard heat exchanger, pumps, fans in radiator consume part of the power produced, thus, reduces the efficiency of the overall system.

Approaches for designing high temperature membranes Several approaches have been attempted for increasing the operating temperature of the membrane maintaining high proton conductivity:

a) Retaining water in membrane at high temperature Efforts have been focused at retaining water in the membrane at high temperature for those which uses water as a proton carrier. For achieving the purpose, inorganic materials or hydrophilic groups are incorporated into the ionomer membrane in the aim of increasing the binding energy of water. [31] As a result, loss of water from the pore of the membrane will be prevented and ionic conductivity of the membrane will be maintained at temperature above the boiling point of water. The performance of hydrophilic additives have been revealed in case of heteropolyacids in nafion. [32] It has been demonstrated that the use of acid helps to maintain sufficient membrane hydration at $\approx$ 115°C. However, water drained from the fuel cell over time and leaching of acid occurs which reduces water retention. To overcome this problem solid materials such as sulfated zirconia, silica gel, which are immobilized in the membrane, can be used and were investigated. [31, 33]

b) Use of non aqueous solvents of lower volatility A possible approach to increase the operating temperature of the PEM is to replace water by lower volatility solvent. Savinell et al. [34] pioneered this approach by utilizing PA doped nafion which was demonstrated to have high conductivity at elevated temperature. Doyle et al. [35] similarly showed that nafion imbibed with ionic liquid, 1-butyl, 3-methyl imidazolium triflate, posses high conductivity above 100°C.

c) Development of new class of solid state proton conductor In this approach, solid state protonic conductors, which conduct in absence of water, are explored. For example, Zaidi et al. [36] embedded heteropolyacids to sulfonated polyether ether ketone (S-PEEK). Conductivity was observed to be similar to nafion. However the most promising membrane, PBI/PA acid complex was fabricated by Savinell et al. [37]. This membrane offers conductivity as high as 0.04 Scm^{-1} at 190°C and negligible amount of

electro-osmotic drag. In the present thesis, research work is carried out to understand the nanostructure and PT mechanism inside the PA doped PBI membrane which are responsible for such high proton conductivity.

d) Use of inorganic-organic composite membrane In recent time, a great deal of effort is invested for developing organic-inorganic composite membrane. [31, 38, 39] For example, Adjemian et al. [33, 40] used nanosized SiO_2 into nafion pores. The advantage of these composite membranes over the conventional membranes are their longer operational time at higher temperature. The investigation also showed that unlike unmodified PEMs, SiO_2 modified PEMs do not exhibit thermal degradation. Similarly, Yang et al. [31] incorporated zirconium phosphate into nafion membrane and obtained results which are similar to those with SiO_2.

PA-doped polybenzimidazole Among all the membranes used in HT-PEMFCs, PA doped polybenzimidazole was found to be most extensively studied. [27, 41–43] Poly [2, 2′-(p-Phenylene)-5, 5′-bibenzimidazole (PBI) and poly (2, 5 Benzimidazole) (ABPBI) solvated with PA are the two most efficient membrane materials in the polybenzimidazole family. [44–46] These polyelectrolyte materials are less expensive compared to nafion and no humidification is required for PEMFC applications. Wainright et al. [47] first introduced PBI as a membrane for PEMFC. PBI and ABPBI have several favourable properties to be used as a high temperature membrane material: i) high glass transition temperature (698-708K) [44] ii) conduct proton in absence of water and provide high proton conductivity after doped with PA [48] iii) PA doped PBI shows good mechanical strength [49, 50] iv) good chemical strength [51] and v) excellent textile fiber properties. [50] The high temperature stability of the doped acids and the affinity between PA and PBI/ABPBI have been a matter of concern, as enough acid doping level is necessary for introducing these membranes in PEMFCs. [52] Numerous experimental studies have been performed on the PA doped PBI and ABPBI membranes concerning their proton conductivity. [29, 53–55] For the PA doped PBI/ABPBI system, proton conductivity strongly increases in a nonlinear fashion with an increasing amount of PA, while the mechanical strength decreases significantly. [26, 42] It was observed that increasing the doping level of PA from 3.28 to 4.62 mol per polymer repeat unit, the proton conductivity increases from 0.020 to 0.060 S cm^{-1}. However, the tensile strength decreases from 121 to 33 MPa. [55] Hence, a doping level of 5-6 mol of PA per mol of polymer repeat unit is reported to be necessary to obtain good conductivity maintaining a reasonable mechanical strength of the membrane. [26] Recently, Xiao et al. [54] developed a sol-gel process in which doping was achieved through the hydrolysis of polyphosphoric acid to PA. The doped membrane contained 20-40 mol of PA per mol of PBI repeat unit, and it acquired good mechanical properties at higher temperatures. For a given doping level,

the conductivity increases with temperature. For example, it was reported that the PBI-PA membrane exhibits proton conductivity of 5 $\times$ 10^{-3} S cm^{-1} at 298 K, which increases to 4 $\times$ 10^{-2} S cm^{-1} at 190 ° C. [53] However, Asensio and coworkers [56] have reported that PA doped ABPBI exhibits better proton conductivity than PBI because of the presence of higher imidazolium group concentration per unit volume of ABPBI, resulting in increasing capability of dissolving acid and thus higher proton conductivity. The study by Zhang et al. [57] demonstrated that PBI membrane with a higher doping level (27.7 mol/RU) exhibits proton conductivity of 0.24 S cm^{-1} at 160 °C whereas ABPBI membrane with acid doping level of only 2.5 mol/RU shows proton conductivity of 0.14 S cm^{-1} at 180 °C. But the disadvantage of ABPBI is that the loss of mechanical strength is more compared to PBI in presence of higher PA content. On the other hand, pure PA has been found to be one of the high proton conduction media at higher temperature (150-200° C) [58] since the boiling point of PA is 213 ° C. The advantage of PA is that it can conduct proton in anhydrous form [59, 60] due to its proton-solvating ability and self-ionization behavior. [61] The higher PA uptake ability of PBI stands in favor of its usage as a proton exchange membrane material.

1.2 Investigation of PT at molecular level

PT through the membrane occurs by two mechanisms: i) Grotthuss mechanism [62] where proton hops along the H-bonding network formed inside the membrane and ii) vehicular mechanism [63] in which proton carrier (membrane components) itself diffuses carrying protons. Since, experimental techniques can not describe the origin of these PT mechanisms directly, theoretical modeling and simulations are needed to understand the PT mechanism in details. This will enable the researchers to design new membrane materials with improved proton conductivity.

Modeling the transfer of proton inside PEM requires the presence of following two features simultaneously which are difficult to obtain: i) since, the relaxation of polymer is a slow process, long time simulation is necessary in order to obtain experimentally observed properties of polymer membrane. Therefore, the model system should be simple enough so that long simulation run would be possible. ii) The model system and theoretical method must represent non classical, complex PT in solvated membrane which is proposed to be borne out by Grotthuss mechanism.

The efforts to provide a detail understanding about the morphology of the hydrated/acid solvated membrane rely on different level of resolutions of the model system. It ranges from all atomistic MD, where all the atoms of the solvent as well as polymer chain are treated explicitly, to united atom model where groups of atoms in the polymer chain are

represented by single interaction sites and finally coarse-grained (CG) model in which multiple atom groups with their substituents are described by a single bead. From the atomistic simulation, detailed structural informations including H-bond network formation are gained. Although, to more accurately model the morphology of PT network, we need to simulate the system at larger length scale. As a result, longer time simulation has to be done to fully equilibrate such large system, representative of the molecular weight used in experiment. However, this is impossible in a computationally feasible time scale. Therefore, one of the reasonable approach is to combine atomistic results from simulation or experiment with CG approaches to obtain accurate representation of membrane structure for predicting experimentally observed conductivity. On the other hand, dissipative particle dynamics (DPD) has been applied on solvated PEM to understand the morphology and phase behaviour of block copolymers.

The use of computational methods to design new PEM materials with improved proton conductivity should fulfill two requirements: i) it must be an accurate method to treat local as well as global arrangements of the membrane constituents ii) appropriately represent the PT mechanism within the correct morphology of the membrane. [64] Proton is transported through PEM following either vehicular or Grotthuss mechanism. Vehicular mechanism can be treated by standard classical MD. [65] But, for accounting Grotthuss mechanism, a method capable of describing bond breaking and making is required. Several methods are applied successfully to deal with Grotthuss mechanism of PT such as *ab initio* MD, empirical valence bond (EVB) theory, [66–68] hopping algorithm within standard MD, [69, 70] reactive MD [71] etc. However, these simulation techniques are highly computationally expensive. Therefore, these methods can not be used for larger systems.

1.2.1 PT in water solvated nafion membrane

Multi-scale modelling techniques have been applied to investigate H-bond network formation and PT mechanism in nafion membrane. Techniques include QM methodology, *ab initio* MD [72–75], EVB technique, [76] classical [22, 77–79] and mesoscale MD. [64, 80] Classical and mesoscale MD were used to understand the H-bonding network, which works as the PT path and morphology of the membrane in large scale. On the other hand, *ab initio* MD and EVB methodology were used to reveal the PT mechanism in the hydrated nafon membrane.

Quantum mechanical optimization was performed on the pendant side chain of nafion by Paddison et al. [81, 82] which revealed that PT occurs only when three or more water molecules are present around each pendant side chain. Choe et al. [63] and Glezakou

et al. [83] investigated the dynamics of PT upon dissociation using *ab initio* MD. The aim was to understand the complex interplay between Grotthuss shuttling and vehicular transport of proton as a function of amount of water. They found that proton hopping strongly depends on the continuity of the water H-bonding network. Therefore, PT gets disrupted at lower water content. The effect of side chain mobility and pore structure inside the membrane have been examined using simple model systems. [84, 85] Although *ab initio* MD method is an efficient method for studying proton dynamics around the individual side chain, it is computationally intractable to model individual pores of nanometer dimension using this method. Therefore, MS-EVB method was used to model PT in confined regions of the membrane. [68, 86, 87] Peterson et al. [66] demonstrated the applicability of self-consistent iterative MS-EVB, known as SCI-MS-EVB in extending time and length scale far beyond *ab initio* MD. Using SCI-MS-EVB method they simulated multiple polymer chains of nafion consists of ten monomer units and also the side chain units in each chain. Proton diffusion coefficients obtained from these simulations well agree with the experimental results. Anti-correlation of the vehicular and hopping motion of the excess proton in nafion was also established from this study. This anticorrelation was not observed while PT occurs in bulk water. Therefore, the study indicates that sulfonate groups significantly influence the PT in hydrated nafion by serving as proton traps. Apart from the basic nature of hopping and vehicular motion of PT, detailed local proton motion related properties within the hydrophilic region of the membrane were investigated. The directionality of the proton hopping as a function of distance from the closest sulfonate group was examined which revealed that protons close to the sulfonate group hop back towards the sulfonate. However, at further distance, probability of hop backward and hop away from the side chain was similar.

Urata et al. [88] performed classical MD to model hydrated proton where backbones were treated with united atom force field and side chains were treated with all-atom force-field. They found that at low hydration level (λ), aggregation of sulfonate units and binding of water to sulfonate unit occurs. At higher hydration state, frequent exchange between free and bound water molecules takes place. The side chains were found to orient themselves perpendicular to the hydrophilic-hydrophobic interface. The simulations by Cui et al. [89] established the fact that clustering of water molecules strongly depends on the hydration level. At low λ, small isolated water clusters are formed which become connected at higher λ. They concluded that poor conductivity at low λ was found due to lack of connectivity between water clusters and poor hydration of hydronium ion. In addition, mesoscale simulations [90, 91] were used to characterize the morphology of the hydrated nafion and estimate the vehicular diffusion coefficients. Most of these model studies and PT mechanism are reviewed by Devanathan [28] and Elliot. [92]

1.2.2 PT in PA doped polybenzimidazole membrane

Experimetal results suggest that conductivity in PA doped PBI membrane depends on the PA doping level, temperature and relative humidity. [93–96]

Not many computational studies on structural properties and proton conductance mechanism have been performed on PA doped polybenzimidazole (PBI and ABPBI) membranes. [43, 97–100] This is primarily because of its complexity and higher length and time scale of the systems. Li et al. [97, 98] studied the structural and electronic properties of monomers of PBI and ABPBI as well as PA in order to explore the nature of H-bonding interaction and the energy barriers for different PT pathways within PA-doped polybenzimidazole. Authors reported the proton affinities of benzimidazole, PA, water and their corresponding ions and categorized them based on their ability to associate a proton. They also found that at lower doping level of PA, there is a formation of strong H-bond between PA and polymer chain. The activation energy barrier for various PT pathways suggest that the excess proton moves to benzimidazole after the initial optimization. The H-bond between PA and benzimidazole is the major interaction in PA solvated polybenzimidazole at lower PA doping level. They also performed classical MD simulation on neat, hydrated and PA solvated PBI and ABPBI and investigated radial distribution function (RDF) and number of different types of H-bonds to characterize the complex H-bonding network formation for both the polymers. They confirmed the less hydrophilic character of PBI, therefore it has lower affinity towards PA compared to ABPBI. The effect of PA doping level and temperature in H-bonding for both the PBI and ABPBI systems were also reported in their paper. Zhu et al. discussed the H-bonding network within neat PBI and PA solvated PBI by investigating RDFs between different proton donor and acceptor sites. [100] They studied the microscopic structure and H-bonding characteristics of the pristine and PA doped *m*-PBI and *p*-PBI using MD simulations based on a united-atom force field model. It was found that among the pristine PBIs, *p*-PBI is more ordered and stretched than the *m*-PBI. The study also revealed that in PA doped PBIs, H-bonding network is formed by donating PA proton to imine nitrogen, PA proton to PA oxygen, and amine hydrogen to PA oxygen.

There are very few first principle MD studies on PA doped high temperature membrane materials till date. [101, 102] Vilčiauskas et al. [101] studied microscopic mechanism accountable for high proton conductivity in liquid PA using *ab intio* MD. The study revealed that interplay between long polarizable H-bonded chain and frustrated H-bonding network is responsible for high proton conductivity in liquid PA. They also simulated PA doped imidazole system [101] and compared it with liquid PA systems to understand the PT mechanism in more realistic system. Authors addressed local structure, dynamics, energetics in their work and established a relation of these properties to long range PT.

1.3 Objective of the present thesis

In order to enhance the efficiency of the HT-PEMFC, there is a need of novel membrane material with high proton conductivity. The above review of current research activities on various PEM materials at different length and time scales suggest an opportunity to investigate the proton transfer events at molecular as well as atomic level exploring new membrane materials. Therefore, the broad objective of the present thesis is to explore and design potential anhydrous membrane materials with improved proton conductivity than existent materials for HT-PEMFCs. For achieving the purpose, fundamental understanding of the membrane properties, proton transfer, solvent mobility in the existent materials are essential. Among the existent membrane materials for HT-PEMFC, PA doped polybenzimidazole membranes are the promising candidates as suggested in the above literatures. Therefore, the current work is focused on these materials. For obtaining an overall understanding about PT in a membrane, which determines the efficiency of a membrane, following three aspects are necessary to address.

1.3.1 PT path

Since proton hops along the H-bonding network, detailed understanding of the H-bond network formation in the system is necessary. Therefore, all atomistic MD where hydrogens are treated explicitly, is used in this thesis. It is important to check the stability of these H-bonds as the transient bonds lead to efficient proton transfer. Besides, classical MD provides access to the nanometer length scale to capture the formation of cluster in the system or whether the components are fully phase separated. The distribution of various sized clusters of membrane constituents reveals a global picture of the structuring of PT path. The effect of solvent in H-bonding network formation, clustering helps us to optimize the amount of solvent for improved PT. The chain conformations of PBI and ABPBI are studied in chapter 5 of this thesis which determines PA absorbing capacities in turn proton conductivity. From the comparative arrangement of solvent along the backbone of the chain and nature of H-bond formation, we can qualitatively predict proton conductivity following PT path.

1.3.2 PT mechanism

PT is consists of proton hopping along the H-bonded network and diffusion of proton carriers. The contribution of these proton transfer mechanisms vary from system to system which in turn decide the proton transfer rate. Therefore, quantitative estimation of both the mechanisms are essential to predict an efficient membrane. However,

structural diffusion occurs at picoseconds time scale whereas vehicular diffusion occurs at nanosecond timescale. Therefore, multiscale simulation techniques are needed to accurately model both the PT mechanisms. Chapter 6 of this thesis presents estimation of Grotthuss mechanism of PT using *ab initio* MD whereas chapter 4 present vehicular motion of PA and BI as a function of PA doping level using classical MD.

1.3.3 Properties related to PT

The participation of PA doped N-containing aromatic heterocyclic compounds in proton conductivity depends to a large extent on the ability of these compounds to accept or donate protons. In this context, estimating proton affinity of various PEMs are necessary to develop new membrane materials. Usually, these aromatic heterocyclic compounds have both the proton donor and acceptor groups. Hence, they can form dynamic H-bonds through which protons are readily transported. Proton affinity of a basic compound depends on the electron density on the acceptor site. If it is too high, the compound will readily take the proton but will not give it back. Therefore, long range PT gets affected. The constituents of a good proton conduction medium should take as well as give away proton readily. The ability of a substrate to give away the proton to other molecules depend on the activation energy barrier for that particular proton transfer. The substrate must overcome that energy barrier. Therefore, a good proton conducting substrate should have a considerable amount of proton affinity (not too high) as well as low activation energy barrier for proton transfer. These properties can be tuned by adding different electron withdrawing or donating substituents on the molecules. In order to estimate the strength of H-bonding interaction between PA and heterocyclic compounds, interaction energy can be evaluated. In chapter 7 of the present thesis, proton affinity, interaction energy and PT energy barriers are listed for a large number of N-containing heterocyclic compounds in presence of PA. Comparing these properties against a benchmark material, we chose promising molecules which can be used to construct membrane with enhanced proton conductivity.

1.4 Overview of this work

In this thesis, first we have investigated the structural and dynamical properties of existent PEM materials (PA doped BI) to understand PT events and presented in chapter 3 and 4. Then we extended our study from monomer to polymer and chapter 5 presents the comparative conformational and structural properties of PBI and ABPBI in presence of PA using all atom classical MD. After obtaining understanding about PT path, we have estimated PT mechanisms quantitatively using *ab initio* MD in chapter 6. In

this chapter, apart from imidazole, we have examined the possibility of using triazole as a membrane material. Being inspired from this study, we have explored other possible N-containing aromatic heterocycles by calculating gas phase properties which govern PT such as proton affinity, interaction energy and PT activation energy barrier using QM methodologies.

In chapter 2, methodological ground works related to this thesis are discussed

In chapter 3, structural properties of PA doped BI and the effect of PA doping level on the nanostructure of PA-BI mixture are discussed

In chapter 4, evidence of dynamical heterogeneity and it's correlation with structural heterogeneity in BI-PA mixture is presented

In chapter 5, comparative structural and conformational properties of PBI and ABPBI chain in melt as well as in PA are discussed

Chapter 6 presents the possibility of using triazole in place of imidazole or along with imidazole using *ab initio* MD

In Chapter 7, gas-phase quantum chemical calculations of proton affinities, interaction energy and proton transport activation energy barriers are listed for a large number of N-containing aromatic heterocycles in presence of PA

Chapter 8 discusses conclusions from the above studies

Chapter 2

Computational method

Molecular modeling numerically solves equation of motion that represents fundamental laws. This is done in various levels of theories. In this chapter, some of the theoretical methods are described which are used throughout the work in the thesis. Structural properties and proton transport (PT) mechanisms are strongly correlated to each other. We have studied dynamics of the atoms and molecules through both classical MD simulation as well as *ab initio* MD. Classical force-field based MD can deal with systems consist of several thousands of atoms in nanosecond time scale. This method has been used to study the structural properties of the polyelectrolyte membrane (PEM) as a function of solvent amount, temperature etc. It also reveals the role of solvent in conformational arrangement of polymer chain. But classical MD fails to deal with the bond breaking and forming phenomenon. Therefore, it prevented us to quantify Grotthuss like PT mechanism. In this respect, first-principle MD is the most reliable one to understand PT mechanism within H-bonding network. On the other hand, although quantum calculations can treat the Grotthuss mechanism, these are computationally very expensive. It takes much longer computational time even to sample a system for few picoseconds. Therefore, density functional theory (DFT) has been introduced to reduce the computational cost. Thus, the concept of electronic density has been introduced in place of wave function in standard quantum calculations. In recent years, there is an increasing interest of using DFT since it is computationally less expensive, allows calculating larger molecules with good accuracy. In this thesis, gas phase DFT based electronic structure calculation is used to compute proton affinity, interaction energy and proton transfer activation energy barrier which help us to predict and design potential membrane materials.

2.1 Quantum mechanics (QM)

In QM, molecules are treated in most fundamental level of theory. It determines electronic structure of a molecule by solving Shrödinger equation 2.1 [103]

$$H\psi = E\psi \tag{2.1}$$

where the Hamiltonian (H) is sum of kinetic and potential energy

$$H = K.E. + P.E \tag{2.2}$$

However, Schrödinger equation can not be solved exactly. Different levels of approximations are frequently required. These approximate solutions are also computationally expensive and are used to only model small molecules.

2.1.1 Density Functional Theory (DFT)

DFT is an alternative method to solve Shrödinger equation in which electron density plays the main role instead of wave function. In traditional quantum chemistry, total wave function depends on 3N electronic coordinates. Hence, computational cost increases with the size of the molecule. On the other hand, in DFT approach, the total electron density always depends only on 3 coordinates, independent of number of electronic coordinates. Therefore applying DFT method, we can solve comparatively larger systems.

2.1.1.1 Theoretical basis

Many body systems and Born-Oppenheimer approximation The Hamiltonian of a many body system can be written as follows:

$$H_{total} = -\sum_{I} \frac{\hbar}{2M_I}\Delta^2_{R_I} - \sum_{i} \frac{\hbar}{2m_e}\Delta^2_{r_i} + \frac{1}{2}\sum_{\substack{I,J \\ I\neq J}} \frac{Z_I Z_J e^2}{|R_I - R_J|} + \frac{1}{2}\sum_{\substack{i,j \\ i\neq j}} \frac{e^2}{|r_i - r_j|} - \sum_{I,i} \frac{Z_I e^2}{|R_I - r_i|} \tag{2.3}$$

where I, J are nuclear and i, j are electronic indexes. M_I and m_e are the masses of nuclei and electrons; R_I and r_i are the positions of nuclei and electrons respectively. The first term of equation 2.3 is the kinetic energy of nuclei; second term is kinetic energy of electrons; third term is the potential energy due to the nucleus-nucleus coulombic repulsion; fourth term is the potential energy due to electron-electron repulsion and fifth

is the nuclei-electron attraction energy term. Hence, the time-independent Schrödinger equation is

$$H_{tot}\psi(R_I, r_i) = E\psi(R_I, r_i) \tag{2.4}$$

$\psi(R_I, r_i)$ is the total wave function of the system. If one can solve this Schrödinger equation, everything of the system would be known. However, in reality it is impossible to solve. Therefore, several approximations were proposed. One of the first and useful assumption is Born-Oppenheimer (BO) approximation proposed by Born and Oppenheimer in 1927. [104] The approximation states that we can separate out the movement of nuclei and electrons since the movement of nuclei are much slower than that of electrons. This is because the mass of nuclei are much heavier than electrons. Therefore, the complete wave function is written as a product of nuclear and electronic wave functions

$$\psi_{tot} = \psi_{nuclear} \times \psi_{electronic} \tag{2.5}$$

BO approximation divides Equation 2.5 into two individual Schrödinger equations for electronic motion (equation 2.6) and nuclear motion (equation 2.8)

$$H_{electronic}\ \psi_{electronic} = E_{electronic}\ \psi_{electronic} \tag{2.6}$$

where

$$H_{electronic} = -\sum_i \frac{\hbar}{2m_e}\Delta^2_{r_i} + \frac{1}{2}\sum_{\substack{i,j \\ i\neq j}} \frac{e^2}{|r_i - r_j|} - \sum_{I,i} \frac{Z_I e^2}{|R_I - r_i|} \tag{2.7}$$

and

$$H_{nuclear}\ \psi_{nuclear} = E_{nuclear}\ \psi_{nuclear} \tag{2.8}$$

where

$$H_{nuclear} = -\sum_I \frac{\hbar}{2M_I}\Delta^2_{R_I} + \frac{1}{2}\sum_{\substack{I,J \\ I\neq J}} \frac{Z_I Z_J e^2}{|R_I - R_J|} \tag{2.9}$$

Equation 2.6 is the equation of electronic motion where positions of the nuclei are fixed. The eigen value, $E_{electronic}$ parametrically depends on the nuclear positions. While, nuclei are treated classically, quantum many body problem boils down to solve only electronic problem. To solve electronic wave function, various approaches exist in the literature: Hartree-Fock (HF), post-HF and DFT methods.

HF and post-HF methods HF [105–107] is the simplest approximate *ab initio* theory for solving many-body electronic problem. It is based on mean field theory which

is also called as self-consistent field theory. The basic idea of the theory is to replace N-body interaction to one electron interaction where each electron interacts with the mean field created by all the other electrons. Therefore, the many body problem becomes approximated to the product of one electron wave functions.
In HF approach, many electron wave function is represented as a single Slater determinant [108], named after John Slater, composed of spin orbitals. Each spin orbital $\chi(\mathbf{x})$ is the product of space part, $\phi(\mathbf{r})$ and spin part, $\alpha(\mathbf{r})$ or $\beta(\mathbf{r})$. $\mathbf{r}$ denotes the coordinate of electrons and space-spin coordinates are denoted as $\mathbf{x} = \{\mathbf{r}, \alpha \text{ or } \beta\}$. The many-electron wave function for a molecule consists of n electrons can be written as:

$$\psi_{HF} = \frac{1}{\sqrt{(n)!}} \begin{vmatrix} \chi_1(\mathbf{x}_1) & \chi_1(\mathbf{x}_1) & \chi_1(\mathbf{x}_1) & \dots & \chi_1(\mathbf{x}_1) \\ \chi_1(\mathbf{x}_2) & \chi_1(\mathbf{x}_1) & \chi_1(\mathbf{x}_1) & \dots & \chi_1(\mathbf{x}_1) \\ \chi_1(\mathbf{x}_3) & \chi_1(\mathbf{x}_1) & \chi_1(\mathbf{x}_1) & \dots & \chi_1(\mathbf{x}_1) \\ \dots & \dots & \dots & \dots & \dots \\ \chi_1(\mathbf{x}_n) & \chi_1(\mathbf{x}_1) & \chi_1(\mathbf{x}_1) & \dots & \chi_1(\mathbf{x}_1) \end{vmatrix} \tag{2.10}$$

Therefore, HF wave function have the form of Slater determinant and energy will be calculated by the QM expression 2.11

$$E_{el} = \langle \psi | \, H_{el} \, | \psi \rangle \tag{2.11}$$

where the wave function, ψ is normalized. For symmetric energy expression, variation theory is employed. Variation theorem states that expectation value of energy for any wave function is always equal to or greater than the true energy. Any wave function can be written as the linear combination of eigenstates

$$\psi = \sum_i c_i \phi_i \tag{2.12}$$

Hence,

$$E[\psi] = \frac{\sum_i c_i^2 E_i}{\sum_i c_i^2} > E_0 \tag{2.13}$$

where, E_0 is the ground state energy. The problem now boils down to finding the coefficients (c_i), which minimize the energy of the approximate wave function.

$$\frac{\partial E[\psi]}{\partial c_i} = 0 \tag{2.14}$$

The energy obtained by the variatioal method is always greater than true ground state energy, E_0. The difference in the energy arises since in HF theory, two electron interaction only contains an average picture of the electrons, thereby neglecting the exact electronic correlation. This is the reason why HF theory is not considered to be trustworthy and gives approximate result. To remedy the drawback, post-HF methods were

developed. Among them two major classes are: configuration interaction (CI) and Möller-Plesset(MP) perturbation theory.

The CI approach uses a wave function which is a linear combination of various configuration states in place of Slater determinant in HF theory. Therefore, spatial correlation in the electronic motion can be considered by using more than one configurations states and putting electron in various orbitals.

$$\psi = C_0\psi_0 + C_1\psi_1 + C_2\psi_2 + ... \tag{2.15}$$

where ψ_0 is the HF wave function and other terms are the contribution from different configuration states. This wave function adds excited configuration states to the ground state configuration state. Both electrons being in the same space corresponds to the lowest energy state whereas higher energy states represent one electron close to nucleus and others are far away. In this way, CI approach takes into account the electron repulsion. Thus, CI successfully consider electron correlation.

However, CI is a rigorous method to add correlation to HF results. This method is computationally very expensive because large number of Slater determinants are required to be included. Another commonly used method which include electron correlation energy is MP method, which is based on perturbation theory rather than variational method. MP adds excitations to HF method as a non-iterative correction. The wave function can be represented as

$$\psi = \psi^0 + \lambda\psi^{(1)} + \lambda^2\psi^{(2)} + \lambda^3\psi^{(3)} + ... \tag{2.16}$$

and the corresponding energy is expressed as

$$E = E_0 + \lambda E^{(1)} + \lambda^2 E^{(2)} + \lambda^3 E^{(3)} + ... \tag{2.17}$$

The parameter λ is dimensionless. The first order MP energy is the HF energy. In MP2 method, second order correction is used. Second (MP2), third (MP3) and fourth (MP4) order MP methods are usually used for estimating properties of small molecules.

Couple cluster (CC) is another post-HF method which made some advances over CI approach. CC is a non-variational method, resolve the size extensivity problem and results obtained using this method is very accurate. However, CC method is computationally more costly compared to CI. In CC method, wave function is written as an exponential ansatz

$$\psi_{CC} = \exp\left(\hat{T}\right)\psi_{HF} \tag{2.18}$$

where T is the cluster operator, acting on a reference wave function usually HF wave function, produces linear combination of excited determinants. The cluster operator $\hat{T}$ is expressed as

$$\hat{T} = \hat{T}_1 + \hat{T}_2 + \hat{T}_3 + ...\dot{.}... \tag{2.19}$$

where $\hat{T}_1$ operates on all single excitations, $\hat{T}_2$ operates on all double excitations and so on. Due to the non-linear nature of the exponential ansatz, CC method recovers more correlation energy compared to CI for a given number of excitations.

Thomas-Fermi model The early work of Thomas [109] and Fermi [110] introduced the use of electron density in place of wave function. The density of a N particle system is expressed as

$$\rho(\mathbf{r}) = N \int \psi^*(\mathbf{r}, \mathbf{r}_2, ...\dot{.}..., \mathbf{r}_n)\psi(\mathbf{r}, \mathbf{r}_2, ...\dot{.}..., \mathbf{r}_n)d\mathbf{r}_2...\dot{.}...d\mathbf{r}_n \tag{2.20}$$

which reveals the probability of finding particles near position $\mathbf{r}$. In Thomas-Fermi (TF) approach, kinetic energy of electrons are derived based on uniform electron gas model and the electron-electron, electron-nucleus interactions are treated classically.

$$T[\psi] = C_F \int n^{\frac{5}{3}}(\mathbf{r})d\mathbf{r} \tag{2.21}$$

Assuming the electron cloud as classical picture of repulsive gas, internal potential energy can be expressed as

$$U[\psi] = \frac{e^2}{2} \int \int \frac{n(\mathbf{r}_1)n(\mathbf{r}_2)}{|\mathbf{r}_1 - \mathbf{r}_2|} d\mathbf{r}_1 d\mathbf{r}_2 \tag{2.22}$$

Therefore, in TF model, total energy of a many-electron system in an external field, V_{ext} can be expressed as a functional of electron density, $n(\mathbf{r})$.

$$E_{TF}[n(\mathbf{r})] = C_F \int n^{\frac{5}{3}}(\mathbf{r})d\mathbf{r} - \int n(\mathbf{r})v(\mathbf{r})d\mathbf{r} + \frac{e^2}{2} \int \int \frac{n(\mathbf{r}_1)n(\mathbf{r}_2)}{|\mathbf{r}_1 - \mathbf{r}_2|} d\mathbf{r}_1 d\mathbf{r}_2 \tag{2.23}$$

The approximations used in TF model are so crude that it suffers from several drawbacks. The severe one is that the homogeneous electron gas model does not include the discrete charge of individual electrons. Therefore, the model fails to describe bonding between atoms. However, the model gives good results for average properties of atoms. It acts as a starting approximation for sophisticated atomic models e.g. HF model. The significance of TF model lie in the fact that this simple model illustrates that energy can be expressed purely as a function of electron density.

Hohenbarg-Kohn theorem Hohenberg and Kohn [111] in 1964 proved that DFT is an exact theory for many-electron systems. It can be applied to any system of interacting

particles moving under the influence of an external potential, $V_{ext}(\mathbf{r})$. Hohenberg-Kohn (HK) theory is based on two significant theorem:

Theorem I A one to one mapping between electron density and external potential had been established. The theorem states that any system of interacting particles moving under the influence of an external potential (V_{ext}), is a unique functional of electron density, $n(\mathbf{r})$. Therefore, Hamiltonian can be fully determined which indicates that many-body wave function for ground as well as excited states can be evaluated.

$$H_{el} = K.E + P.E + V_{ext} \tag{2.24}$$

Thus, HK theorem states that if we can determine the correct ground state density, $n_0(\mathbf{r})$ then all the other properties of the many body system would be known.

$$E(n(\mathbf{r})) = \int n(\mathbf{r}) v_{ext}(\mathbf{r}) + F(n(\mathbf{r})) \tag{2.25}$$

$$E(n(\mathbf{r})) = \langle \psi | \, H \, | \psi \rangle \tag{2.26}$$

$$H = \hat{F} + \hat{V}_{ext} \qquad where \qquad F = \hat{K.E} + \hat{P.E} \tag{2.27}$$

Theorem II For any particular external potential, V_{ext}, ground state energy can be obtained using variation theorem i.e. the exact ground state energy of the system is the minimum value of energy functional, $E(n(\mathbf{r}))$ and the density that minimizes the energy functional is the exact ground state electron density, $n_0(\mathbf{r})$.

$$E(n_0(\mathbf{r})) \leq E(n(\mathbf{r})) \tag{2.28}$$

i.e.

$$\int n(\mathbf{r}) V_{ext}(\mathbf{r}) d\mathbf{r} + F[n(\mathbf{r})] \geq \int n_0(\mathbf{r}) V_{ext}(\mathbf{r}) d\mathbf{r} + F[n_0(\mathbf{r})] \tag{2.29}$$

Thus, the HK theorem tells us that the exact energy functional is sufficient to calculate exact electron density and exact ground state energy. However, it does not mention how to form the functional $F[n(\mathbf{r})]$ explicitly. We will be able to obtain good approximations to the exact ground state energy $E_0[n_0(\mathbf{r})]$ and density $n_0(\mathbf{r})$, only if we can construct a good approximation to the exact functional $F[n(\mathbf{r})]$. Therefore, HK theory was impractical to use for calculating any properties.

Kohn-Sham model Kohn-Sham (KS) theory [112] makes the DFT into practical use and some calculations are even possible in personal computer by implementing this theory. Kohn got Nobel prize in 1988 for his most popular and successful KS theory. Kohn and Sham realized that the failure of TF model was due to the improper description of kinetic energy. To circumvent the problem, they reintroduced the idea of one

electron orbital and determine the kinetic energy assuming that the electrons are non interacting. Thus, KS theory assumes that the exact ground state density of a system can be described as the ground state density of an auxiliary system in which electrons do not interact. The auxiliary hamiltonian is formulated such that it contains conventional kinetic energy operator $\hat{T} = -\frac{1}{2}\Delta_{r_i}^2$ but the potential is described as an effective potential, $\hat{V}_{eff}$. In KS approach, electron density, $n(\mathbf{r})$ is represented in terms of auxiliary single particle wave function, $\psi_i(\mathbf{r})$

$$n(\mathbf{r}) = \sum_{i=1}^{n} |\psi_i(\mathbf{r})|^2 \tag{2.30}$$

The energy functional in KS theory is

$$E_{KS}[n] = \hat{T}_0[n] + \int n(\mathbf{r})[V_{ext}(\mathbf{r}) + \frac{1}{2}\hat{V}_{Hartree}(\mathbf{r})d\mathbf{r}] + E_{xc}[n] \tag{2.31}$$

where $\hat{T}_0$ is the kinetic energy of the system of electronic density $n(\mathbf{r})$ and in absence of electron-electron interaction. $\hat{V}_{Hartree}$ represents Hartree potential which is the classical coulomb potential of electrons. E_{xc} is called the exchange-correlation energy. This term incorporates exchange as well as correlation energy and also the remainder of electronic kinetic energy and anything else which are needed to make E_{KS} to be the exact energy functional, $E_0(n(\mathbf{r}))$. For, E_{xc}, a good approximate functional is required to be constructed since the exact form of the functional is not known. In principle, more exact the E_{xc} used in KS equation, more accurate will be the resulting electronic density and energy including the many body effects.

2.1.1.2 Different Exchange-correlation functionals

Exact form of the exchange-correlation functional is not known till date. Therefore, one has no other option but to rely on the specific approximations of the functionals.

Local density approximation The simplest approximation was proposed by Kohn and Sham in 1965, is called Local density approximation (LDA). It is written as:

$$E_{xc}^{LDA} = \int \epsilon_{xc}(n(\mathbf{r}))n(\mathbf{r})dr = \int n(\mathbf{r})[\epsilon_x(n(\mathbf{r})) + \epsilon_c(n(\mathbf{r}))]d\mathbf{r} = E_x + E_c \tag{2.32}$$

$\epsilon_{xc}(n(\mathbf{r}))$ is the exchange-correlation energy per electron of the homogenious electron gas of density $n(\mathbf{r})$. The exchange energy, ϵ_x is known exactly and the correlation energy, ϵ_c is obtained by fitting to the independent quantum Monte Carlo studies by Ceperley and Alder. Several LDA functionals have been formulated such as Perdew-Zunger (PZ), Perdew-Wang (PW), Vosko-Wilk-Nusair (VWN) which differ only in how

the correlation part has been fitted to the many electron gas data. However, LDA is only valid for systems having slowly varying density. Although the approximation of homogenious eletron gas is a very crude approximation for most of the systems, it has proven to be successful in a large number of cases. This is due to the cancellation of errors as it overestimates ϵ_x while underestimates ϵ_c.

Generaized Gradient Approximation Although LDA has been successfully used to obtain accurate cohesive energy, lattice constant of metallic and non-metallic solids, it produces huge error ($\sim 20\%$) while calculating binding energy. Thus a lot of effort has been devoted to improve the exchange-correlation functional. In Generalized Gradient approximation (GGA), refinement of LDA was made, where apart from local density, the functional depends on the gradient of density.

$$E_{xc}^{GGA} = \int \epsilon_{xc}^{GGA}(n(\mathbf{r}), |\boldsymbol{\nabla} n(\mathbf{r})|)dr \tag{2.33}$$

An approriate choice of ϵ_{xc}^{GGA} takes into consideration the correct $\frac{1}{\mathbf{r}}$ assymptotic behaviour for the exchange energy density at long range and reduces the error of LDA by an order of magnitude. The most widely used GGAs are PBE, BLYP, RPBE, PBE-WC etc. BLYP functional was used in this thesis while performing *ab initio* MD.

Meta-GGA This is the third generation functional. In meta-GGA, in addition to density and gradient of density, second derivative of density, $\boldsymbol{\nabla}^2 n(\mathbf{r})$ or kinetic energy, $1/2 \sum_i |\boldsymbol{\nabla}\psi_i|^2$ is considered as an additional degree of freedom. In determining gas phase molecular properties, meta-GGA such as TPSS functional produces improved results over LDA or GGA. Minnesota functionals, developed by the group of prof. Donald Truhlar at the university of Minnesota, based on meta-GGA approximations. These functionals include M05, M05-2X, M06, M06-L, M08-HX, M08-SO etc. We used M06 functional in this thesis for quantum chemical calculations of small molecules. However, meta-GGA functional has not been widely exploited for solid state materials till date.

Hybrid functionals It is the fourth genertion functional which takes a portion of exact exchange from HF theory and rest of the exchange and correlation from other sources such as conventional DFT treatment of exchange and correlation. The most widely used hybrid functional is B3LYP which uses three parameters (a_1, a_2 and a_3), obtained by fitting to the experimental data. The parameters control the mixing of HF exchange and DFT exchange and correlation. The formulation of B3LYP is of the form

$$E_{xc} = E_x^{LDA} + a_1(E_x^{HF} - E_x^{LDA}) + a_2 \Delta E_x^{GGA} + a_3 \Delta E_c^{GGA} \tag{2.34}$$

B3LYP was used in this thesis for optimizing the initial structure of some molecules. If GGA used is PBE, then we call the hybrid functional as PBE0. Other hybrid functionals proposed are HSE, BH&HLYP (has 50% HF exchange). These hybrid functionals offer significant improvement in calculating gas phase properties of molecules and band gaps for solids over LDA and GGA.

2.1.2 Basis set

A basis set is a set of functions used to describe molecular orbitals and these are expanded as a linear combination of coefficients. In order to solve Schrodinger equation and to obtain the associated wave function, the wave function need to be extended into components of a basis set, ϕ_n where n is the number of basis functions.

$$\psi(\mathbf{r}) = \sum_{j=1}^{n} c_j \phi_j(\mathbf{r}) \tag{2.35}$$

In principle, to describe any wave function $\psi(\mathbf{r})$ exactly by basis set expansion, a complete set of basis functions (ψ_∞) are required. Therefore an infinite number of coefficients (c_∞) are needed to be determined to describe the wave function, $\psi(\mathbf{r})$. However, this is not practical to implement. Thus a finite basis set is used. J.C. Slater first developed the concept of basis set which is expressed in the form: $N * e^{-(\alpha * r)}$ where N is normalization constant, α is orbital exponent and r is radius. There are two general classes of basis sets: a) minimal basis set which describes only the basic aspects of orbitals and b) extended basis set in which much more detailed descriptions are implemented. Two major types of minimal basis sets include Slater types orbital (STO)and Gaussian type orbital (GTO). The STO and GTO equations are expressed as

$$STO = \frac{\xi^3}{\pi^{0.5}} e^{-\xi r} \qquad \text{and} \qquad GTO = \frac{2\chi}{\pi^{0.75}} e^{-\chi r^2} \tag{2.36}$$

The difference in STO and GTO is in the nature of the dependence on r. Since GTO uses square of r, the product of gaussian primitive would be another gaussian and thus we would have much easier workable equation. But the gaussian functions are less accurate to describe atomic orbitals compared to Slater functions. It has been found that if more gaussians are combined, results become more accurate. Therefore, linear combination of GTOs are used to approximate STO. The most common minimal basis set is STO-nG where n is the number of GTOs used to comprise single basis function which describe each orbital. In the minimal basis sets, all orbitals are approximated to be of the same shape which is not true. Therefore, several extended basis sets are used such as double zeta, triple zeta, quadrapole zeta, split valence, polarized basis, diffuse basis, plane wave

basis. Double zeta basis set treat each orbital separately and each orbital is described as the sum of two STOs.

$$\phi_{2s}(r) = \phi_{2s}^{STO}(r, \xi_1) + d\phi_{2s}^{STO}(r, \xi_2) \tag{2.37}$$

The value of ξ represents how diffuse each STO is and the constant d determines the contribution of each STO towards the final orbital. In equation 2.37, we can see each STO is of different size as ξ are different. the d accounts the percentage to add in for the second STO. The triple and quadrapole basis sets work in the same principle except three and four STOs are used respectively in place of two STOs.

It takes much computational time to calculate double zeta for each orbital. Thus, since inner shell electrons do not actively participate in bonding, scientists simplified the matter by considering single STO for inner-shell electrons and two or three STOs or GTOs for valence electrons. This type of basis set is known as split-valence basis set. For example 3-21G, 6-31G, 6-311G etc. In 6-31G, 6 is the number of GTOs used to describe inner-shell orbitals, 3 and 1 are the number of GTOs comprise the first and second STO of double zeta used to describe valence orbitals.

It has been found that when atoms are close to each other, their charge distribution causes polarization effect. Therefore, to improve the model basis set, polarization effect is considered. Polarization functions are added into split valence basis set, represented by orbital name. For example, 6-31G(d) indicates polarization is accounted in p orbital and 6-31G(d,p) denotes polarization is used on s as well as p orbitals.

Diffuse functions are commonly added to the split valence basis set for accurate representation of loosely bound electrons. For example, pople-type of basis sets are denoted by '+' sign. Single + accounts only p orbitals whereas double '+' sign take into consideration p as well as s orbitals. Correlation-consistent basis sets are larger basis set, denoted by aug e.g. aug-cc-PVTZ.

2.1.3 *Ab initio* molecular dynamics

Ab initio molecular dynamics (AIMD) simulates the motion of the atoms based on the forces, calculated quantum mechanically [113, 114], which are performed on the fly as the molecules move. Therefore, electronic variables act here as active degrees of freedom. This implies that for a given suitable solution of many electron system, it can be treated with AIMD. In this case, one has to choose the level of approximation for getting the best possible solution of Schrodinger equation. In spite of the advantages, a price has to be paid in AIMD: the length and time scale accessible in this case is much smaller

than classical MD. Among the various *ab initio* MD techniques, two significant types, Born-Oppenheimer MD (BOMD) and Car-Parinnello MD (CPMD) are discussed in this chapter.

2.1.3.1 Born-Oppenheimer molecular dynamics

In BOMD, static electronic structure problem is solved at each molecular dynamics time step, given the set of nuclear positions at that instant of time. [115] Therefore, the problem boils down to solve a time independent quantum problem. It is done by solving the time independent Schrodinger equation and concurrently propagating the nuclei by Newton's second law. Thus, equation of BOMD for electronic ground state is expressed as

$$M_i\ddot{\mathbf{R}}_i(t) = -\boldsymbol{\nabla}_i \min_{\psi_0} \langle\psi_0| H_e |\psi_0\rangle \tag{2.38}$$

$$E_0\psi_0 = H_e\psi_0 \tag{2.39}$$

The equations 2.38 and 2.39 ensure that the minimization of H_e is done at each BOMD step by using either HF approximation or KS DFT.

2.1.3.2 Car-Parrinello molecular dynamics

In 1985, Car and Parrinello developed a new AIMD technique by combining conventional MD with the DFT technique, called CPMD [116]. The method takes advantage of quantum chemical adiabatic time scale separation of slow nuclear and fast electronic motions. It is then transformed into adiabatic energy scale separation in dynamical theory framework of the system. This is done via mapping of a quantum-classical problem into a two component pure classical problem where two separate energy scales are employed at the price of loosing the explicit time dependence of the dynamics of quantum subsystem. The CPMD method postulated the following Lagrangian

$$L_{CP} = \frac{1}{2}\sum_i \mu \int |\dot{\psi}(\mathbf{r})|^2 + \frac{1}{2}\sum_I M_I \dot{\mathbf{R}}_I^{\,2} - E_{total}[\psi_i, \mathbf{R}_I] + \sum_{ij} \Lambda_{ij}\Big(\int \psi_i^*(\mathbf{r})\psi_j(\mathbf{r}) - \delta_{ij} d\mathbf{r}\Big) \tag{2.40}$$

where the Lagrangian, L_{CP} does not depend explicitly on time, is a functional of two degrees of freedom, $\psi_i(\mathbf{r})$ and $\mathbf{R}_I$ which depend on time. μ_i is an arbitary parameter which acts as an fictitious mass for electrons. The first and second term in equation 2.40, denotes kinetic energy of electrons and nuclei respectively. E_{total} is the potential energy of the overall system. In equation 2.40, Lagrangian multipliers, Λ_{ij} is used to impose the orthonormality condition on ψ_i.

The classical Lagrangian, L_{CP} in equation 2.40 generates trajectories for the nuclei and

electrons via the following coupled set of equations:

$$M_I \ddot{\mathbf{R}}_I{}^2 = -\frac{\partial E}{\partial \mathbf{R}} \tag{2.41}$$

$$\mu \ddot{\psi}_i(\mathbf{r}) = -\frac{\partial E}{\partial \psi_i^*(\mathbf{r})} + \sum_j \Lambda_{ij}\psi_j \tag{2.42}$$

In CPMD method, nuclei evolve with time at a physical temperature $\propto$ kinetic energy of nuclei and a fictitious temperature $\propto$ kinetic energy of electron is associated with the electronic motion. Therefore, ground state wave function optimized for initial nuclear configuration is assumed to be close to its ground state during the time evolution if the system is kept in a sufficiently low temperature. Thus, in this particular method unlike BOMD, the wave function need not to be optimized at each MD step.

2.1.3.3 Comparison of BOMD and CPMD

The comparison of CPMD and BOMD in terms of computational cost is a delicate issue. For example, it depends significantly on the choice which makes the conservation of energy, E_{cons} more accurate. Therefore, it varies from person to person at what extent the accuracy of E_{cons} should be considered, balancing with the computational time. The comparison between the two methods also make one able to consider the more suitable method depending on the system type and size. One of the advantage of CPMD over BOMD is that the minimization of energy functional which is equivalent to the diagonalization of the Hamiltonian, is not required at each MD step. In CPMD, only at the very first step it is required to get the initial wave function. However, electron dynamics are treated explicitly in CPMD, thus, it does not allow to take a larger time step to integrate the coupled equations of motion for electrons and nuclei. On the other hand in BOMD, maximum time step used is given by the nuclear motion as there is no explicit dependence on electronic motion. Therefore, it would be expected that BOMD take less computational time. But, in reality, time gained due to larger time step is lost in orthogonalization in case of BOMD. In BOMD, computation cost can be reduced by increasing time step and decreasing the wave function convergence quality but as a result one will obtain less accurate E_{cons}. The details of BOMD and CPMD have been discussed in several reviews and books. [113, 115, 117, 118] In the present thesis, CPMD method is used to understand the PT mechanism in liquid system.

2.2 Classical molecular dynamics

In this thesis, classical MD simulation technique has been applied to study simple as well as polymer melt systems. All atom MD simulation has been performed since we are interested on inter-atomic interactions which determine the macroscopic observable properties of the system. In classical MD, nuclear motion of each atom in the system is treated by Newton's equation of motion.

$$m_i \frac{\partial^2 \boldsymbol{r_i}}{\partial t^2} = \boldsymbol{F_i}, \quad i = 1 \ldots N \tag{2.43}$$

where, m_i and $\mathbf{r}_i$ is the mass and position of i^{th} particles while the systems composed of N number of particles. F_i, force acting on the i^{th} particle is the negative of the derivative of potential, $V(\mathbf{r}_1, \mathbf{r}_2, \mathbf{r}_3, \ldots \mathbf{r}_n)$.

$$\boldsymbol{F_i} = -\frac{\partial V(\boldsymbol{r}_1, \boldsymbol{r}_2, \boldsymbol{r}_3 \ldots \boldsymbol{r}_n)}{\partial \boldsymbol{r}_i} \tag{2.44}$$

The equations 2.43 and 2.44 are solved at each time step to obtain the new force which in turn determines the positions and velocities of each particle of the system as a function of time. At regular time interval, the file containing the positions and velocities of all the particles represents dynamic trajectory of the system.
However, the potential used in classical MD does not account the electronic motions which makes it computationally less expensive compared to *ab initio* MD. Electrons are assumed to adjust their motion and remain in the ground state instantly with the dynamics of the nuclei (BO approximation as earlier discussed in this chapter).

2.2.1 Force field

The force field is used in classical MD to estimate the internal potential energy as a function of atomic positions. The electronic motions are not considered in the force field except in a mean-field manner. Force field, consists of set of potential energy functions and parameters, represents inter-atomic potential. The parameters are derived from either experimental work or *ab initio* calculations. A force field is expressed as the summation of bonded and nonbonded contribution. The bonded part has three components: bonds, angles and dihedrals and nonbonded term contains Leenard-Jones

(LJ) and coulomb potentials.

$$V = V_{bonded} + V_{nonbonded}$$
$$V_{bonded} = \sum_{bonds} \frac{1}{2} K_b (b - b_0)^2 + \sum_{angles} \frac{1}{2} K_\theta (\theta - \theta_0)^2 + \sum_{dihedrals} K_\phi (1 + cos(n\phi - \lambda))$$
$$V_{nonbonded} = \sum_{LJ} 4\epsilon_{ij} \left[\left(\frac{\sigma_{ij}}{r_{ij}} \right)^{12} - \left(\frac{\sigma_{ij}}{r_{ij}} \right)^{6} \right] + \sum_{coulomb} \frac{q_i q_j}{4\pi\epsilon_0 r_{ij}} \tag{2.45}$$

We can observe in equation 2.45, harmonic functions are used for bond and angle potentials and for dihedrals, a cosine periodic function is used. The values, b, θ and ϕ at a certain time denote the deformation of length, angle and dihedral respectively compared to their corresponding equilibrium values of b_0, θ_0 and ϕ_0. For dihedral, functional form is defined with phase, λ and multiplicity, n. K_b, K_θ and K_ϕ are bond, angle and dihedral force constants respectively. These force constants are the measure of the energies required to stretch or contract a bond, distort a angle from their equilibrium value. The nonbonded term consists of van der Waals forces of the form of LJ 12-6 potential and coulomb electrostatic potential. The LJ potential between particle i and j contains an attractive tail ($-1/r^6$), a negative well depth (ϵ_{ij}), and a repulsive steep wall at a distance, r, while, $r < \sigma$. At σ_{ij}, the potential between i and j becomes zero and it is denoted as van der Waals radius. q_i and q_j in coulomb potential are the partial charges on atom i and j. ϵ_0 and ϵ_r are the dielectric constant in vacuum and relative dielectric constant of the medium respectively. All these described parameters, expressed in equation 2.45, are calculated to develop an accurate force field which will give us an accurate enough potential energy and in turn force. The force fields, usually used are OPLS [119, 120], CHARMM [121, 122], GROMOS [123], AMBER [124] etc, which are parameterized against various complex chemical compounds.

2.2.2 Periodic boundary condition

We perform MD simulations to determine macroscopic properties of bulk systems. However, our simulations can run only over small number of particles, not slowing down the computation. Therefore, if we consider a box surrounding the system of particles, most of the particles would remain near the surfaces of the box and produce surface effects. To lessen the influence of surface effects on bulk properties of the system, the system size considered in the computation must be extremely large. In this context, periodic boundary condition (PBC) is applied in MD simulations to avoid the surface effect caused by the finite size of the system. PBC replicates the simulation box throughout the space and make the system infinite one. During the simulation, when a particle in the central

box moves, the periodic image of the particle in each of the other boxes would move in exactly same way. Therefore, when a particle will leave the central box, its image will enter the box from the opposite site as if there are no boundary at the edges of the central box, thus, the simulation box has no surface. [125] In this way, surface effect is eliminated using the trick called PBC. During the simulation, it is not required to store the coordinates of all the images which would be infinite in number, only the particles in the central box will be considered. When a particle will leave the box passing through the boundary, the identical particle entering from the opposite site will be taken care of. PBC is usually used along with minimum image convention for calculating short range forces. Because, due to applying PBC, each particle in the simulation box interacts with the other particles as well as their images, making the number of interacting pairs extremely large. The basic idea behind minimum image convention is that it only considers interactions between each molecule and the nearest image of the neighbor molecule. Thus, computational efficiency increases for calculating the short range forces. For consistency with the minimum image convention, cut-off distance must be less than or equal to the half of the box length. [126] Sometimes, PBC is observed to affect the system considered especially, for small system sizes or properties associated with large long range contribution. However, the effect on equilibrium properties are significantly less. The most commonly used simulation box shape is cubic. However, there are also boxes of other shapes such as truncated otahedron, rhombic dodecahedron which can be used.

2.2.3 Equation of motion integrator

After calculating the force, Newton's equation of motion is integrated and the particles are propagated in the system. Various integration algorithms are available among which leap-frog method is widely used. [127] It generates the positions and velocities with time from the force at current time using the following equations:

$$\begin{aligned} v(t+\frac{1}{2}\delta t) &= v(t-\frac{1}{2}\delta t) + \frac{F(t)}{m}\delta t \\ \mathbf{r}(t+\delta t) &= \mathbf{r}(t) + v(t+\frac{1}{2}\delta t)\delta t \end{aligned} \tag{2.46}$$

In this algorithm, velocities are calculated at $t+\frac{1}{2}\delta t$ time and used to calculate the position $\mathbf{r}$, at time $t+\delta t$. Thus, velocities leap over the positions and then positions leap over the velocities. The advantage of this method is that velocities are explicitly calculated. However, the drawback is that they are not calculated at the same time as positions.

Therefore, the velocities are approximated according to the following equation:

$$v(t) = \frac{1}{2}\left[v\left(t - \frac{1}{2}\delta t\right) + v\left(t + \frac{1}{2}\delta t\right)\right] \tag{2.47}$$

In the integrator, δt is the time step, given as input in MD. It is chosen based upon the frequency of bond vibration in the system. δt is usually taken as 1 fs. However, in certain cases, we constrain the vibration of bonds if they do not play any significant role in the system dynamics, to enhance the computational performance. In these cases time step of 2 fs are used. This constraining bond technique is implemented in GROMACS simulation package used in this thesis, using different algorithms such as LINCS [128, 129], SHAKE [130] etc.

2.2.4 Energy minimization

Geometry optimization in terms of the potential energy minimization is one of the requirement before performing MD simulations. This is due to the fact that initial geometry of the system may stay in an extremely high energy configuration for example system in which some atoms or molecules remain in partially overlapped state. Therefore, during the MD run, strong repulsive forces, act in the system without optimization, cause large increase in atomic velocities, thus, system gets exploded and simulation gets crashed. The energy minimization is performed by potential energy evaluation and conformation adjustment. Conformation adjustment is done iteratively depending on the algorithms used and system size. There are several energy minimization algorithms available among which steepest descent, conjugate gradient are implemented in GROMACS.

2.2.4.1 Steepest descent method

The steepest descent method is one of the iterative method which uses first order derivative information. The method makes use of the gradient of potential energy surface (PES) which relates to the forces in the MD description of the given system. It guides us to find a path towards the nearest energy minimum. This method works by reducing the potential energy by changing the molecular conformation in response to the force applied to them. In steepest descent method, a succession of conformations are generated iteratively according to the following equation:

$$x(k) = x(k-1) + \lambda(k)F(k) \tag{2.48}$$

where k is the number of iteration, $x(k)$ denotes the conformation, $\lambda(k)$ is the step size and $F(k)$ is the force for k^{th} iteration. For the first iteration, step size is chosen

arbitrarily or by some heuristic. After each iteration, step size is adjusted depending on whether the potential energy of the system is decreased or increased in that step. If energy increases, the step size is assumed to be too large so that it jump over the local minima along that direction. Therefore, the step size is reduced by some factor. On the other hand, when energy is reduced, the step size is increased by some factor. In this way the continuous adjustment of step sizes keeps the PES roughly appropriate near the area of interest. However, steepest descent is a very robust method in locating nearest local minima and not an efficient method for PES with multiple local minima. Although, it is a good method for avoiding steric conflicts and relaxing bond and angles.

2.2.4.2 Conjugate gradient method

Steepest descent method takes large number of steps to reach the minimum. Therefore, a new method was developed to construct new direction, conjugate to the old gradient and all previous direction traversed, called conjugate gradient method. In this method, the new direction of the atomic movement are computed using the energy gradient of the current atomic positions and the direction moved in the last step. Each successive step keep on refining the direction towards minima. Therefore, the reverse of the progress made in steepest descent method is avoided here. However, conjugate gradient method is computationally more expensive and it's storage requirement is also large. But the total expenses and longer time per iteration is compensated by the efficient convergence to the energy minimum obtained in this method. For larger systems, conjugate gradient method is usually chosen.

2.2.5 Statistical ensemble

Statistical distribution is the distribution of various microscopic states lead to a set of macroscopic constraints. The macroscopic constraints include: constant volume (V), temperature (T), pressure (P), energy (E) and number of molecules (N) in a system. Three frequently used ensembles are i) canonical ensemble (NVT), in which N, V and T are held constant, ii) microcanonical ensemble (NVE), in which N, V and E are constant and iii) isothermal-isobaric ensemble (NPT), where N, P and T are held constant. The information of the statistical ensemble is used in a MD simulation as an input parameter. There are various techniques available to perform constant temperature or constant pressure MD.

2.2.5.1 Thermostat

In MD simulation, for pursuing a constant temperature ensemble, various types of thermostats are used. For example, weak coupling thermostat such as Berendsen [131], extended ensemble scheme of Nosé-Hoover [132, 133], velocity rescaling scheme [134] and stochastic coupling method e.g. Anderson thermostat are implemented in GROMACS. Berendsen and velocity rescaling thermostat, used in this thesis, are described below.

Berendsen thermostat The temperature of a system is governed by the velocities of the particles in the system. Therefore, a way to change the temperature of a system is velocity scaling. If the velocities are scaled by a factor λ, associated temperature change, ΔT is calculated using the following equation:

$$\begin{aligned} \Delta T = \frac{1}{2}\sum_{i=1} 2\frac{m_i(\lambda v_i)^2}{N_{df}k_B} - \frac{1}{2}\sum_{i=1} 2\frac{m_i v_i^2}{N_{df}k_B} \\ \Delta T = (\lambda^2 - 1)T(t) \\ \lambda = \sqrt{T_0/T(t)} \end{aligned} \tag{2.49}$$

where $T(t)$ is the temperature at time t calculated from kinetic energy and T_0 is the desired temperature. Therefore, in this velocity scaling approach, to maintain a desired temperature (T_0), velocity is multiplied by a factor (λ) at each time step.

Berendsen thermostat [131] is the weaker formulation of this approach. To maintain the temperature, system is coupled to an external heat bath of desired temperature (T_0). The velocities are scaled at every step so that the rate of change of temperature is proportional to the temperature difference

$$\frac{dT(t)}{dt} = \frac{1}{\tau}(T_0 - T(t)) \tag{2.50}$$

where, τ, the coupling parameter, measures at what extent the system and bath are coupled together. The change in temperature in the successive time step occurs according to equation 2.51.

$$\Delta T = \frac{\delta t}{\tau}(T_0 - T(t)) \tag{2.51}$$

Therefore, the scaling factor for velocities is represented as

$$\lambda^2 = 1 + \frac{\delta t}{\tau}\left\{\frac{T_0}{T(t - \frac{\delta t}{2})} - 1\right\} \tag{2.52}$$

The $T(t - \frac{\delta t}{2})$ term comes due to the use of leap-frog algorithm as an integrator. The value of τ is chosen in practice to adjust the coupling strength. Therefore, depending on the system to be simulated, user can adjust the coupling strength between system and bath, which is a major advantage of Berendsen thermostat. However the value of τ must be chosen with great care. This is due to the fact that if $\tau \to \infty$, Berendsen thermostat becomes inactive and the simulation samples a microcanonical ensemble. On the other hand, too small value of λ leads to extreme low temperature fluctuation which is unrealistic. Usually, $\tau = 0.1$ ps is used in MD simulation. Berendsen method work efficiently while heating or relaxing the system towards equilibrium at target temperature. However, the ensemble generated using Berendsen thermostat is not a canonical ensemble since the energy fluctuations are not captured correctly.

velocity rescaling Velocity rescaling is an extension of Berendsen thermostat in which an additional stochastic term is used to ensure correct kinetic energy distribution. [134]

$$dK = (K_0 - K)\frac{dt}{\tau} + 2\sqrt{\frac{KK_0}{N_f}}\frac{dW}{\sqrt{\tau}} \tag{2.53}$$

where, K is the kinetic energy, N_f is the degrees of freedom and dW a wiener process. The advantage of velocity rescaling method is that the ensemble produced using velocity rescaling thermostat is canonical ensemble.

2.2.5.2 Barostat

Since most of the experimental measurements are done at constant pressure, it is desired to perform MD simulation holding the pressure constant to be able to accurately predict the system properties. Since pressure is related to the virial term which depends on the positions of the particles and the derivative of the potential energy function, pressure often fluctuates more than temperature (T) in an NVT or energy (E) in an NVE MD simulation. These fluctuations are noticed in the instantaneous pressure values of the system during the simulations while average pressure must approach to desired pressure. Generally, during constant pressure simulations, temperature and number of atoms are also held constant while volume of the system is changed in order to achieve the desired pressure. Therefore, lesser the compressibility of the system, larger will be the fluctuation in pressure.

Berendsen barostat Berendsen barostat [131] maintains constant pressure via coupling the system to a constant pressure reservoir. The change in pressure of the system

is estimated as

$$\frac{dP}{dt} = \frac{1}{\tau_P}(P_0 - P(t)) \tag{2.54}$$

where, τ_P is the coupling constant, P_0 is the desired pressure and $P(t)$ is pressure at time t. For accommodating this pressure change, volume of the system is scaled by a factor, λ, at each time step. Thus, corresponding coordinate of each particle is scaled by factor, $\lambda^{1/3}$.

$$R(t + \delta t) = \lambda^{1/3} R(t) \qquad where \qquad \lambda = \left[1 - \frac{\delta t}{\tau_P}(P - P_0)\right]^{\frac{1}{3}} \tag{2.55}$$

Berendsen barostat includes P_0 and τ_P as input. Besides, one can define which directions are to be coupled with the pressure bath during the simulation depending on the system of interest.

Chapter 3

The effect of PA doping level on the structural properties of PA doped BI system[1]

3.1 Introduction

Phosphoric acid (PA) doped polybenzimidazole (PBI) is a promising polyelectrolyte membrane for high temperature (100°C and above) fuel cells. Proton conduction is governed by the amount of PA content in the polymer membrane. Numerous experimental studies have been performed on the PA doped PBI membrane concerning its proton conductivity. [53–55] For the PBI/PA system, proton conductivity strongly increases in a nonlinear fashion with an increasing amount of PA, while the mechanical strength decreases significantly. [26, 42, 55] It was observed that increasing the doping level of PA from 3.28 to 4.62 mol per polymer repeat unit, proton conductivity increases from 0.020 to 0.060 S cm^{-1}. However, the tensile strength decreases from 121 to 33 MPa. [55] Hence, a doping level of 5-6 mol of PA per mol of polymer repeat unit is reported to obtain good conductivity maintaining a reasonable mechanical strength of the membrane. [26] Recently, Xiao et al. [54] developed a sol-gel process in which doping was achieved through the hydrolysis of polyphosphoric acid to PA. The doped membrane contained 20-40 mol of PA per mol of PBI repeat unit, and it acquired good mechanical properties at higher temperatures. For a given doping level, the conductivity increases with temperature. For example, it was reported that the PBI/PA membrane exhibits

[1]This chapter is adapted from the publication Swagata Pahari, Chandan Choudhury, Prithvi Raj Pandey, Minal More, Arun Venkatnathan, S. Roy, Molecular Dynamics Simulation of Phosphoric Acid Doped Monomer of Polybenzimidazole: A Potential Component of Polymer Electrolyte Membrane of fuel cell, J. Phys. Chem. B, 116 (2012) 7357

proton conductivity of 5×10^{-3} S cm^{-1} at 298 K, which increases to 4×10^{-2} S cm^{-1} at 190°C. [53]

In this chapter of the thesis, we report the structural and dynamical properties of 2-phenyl-1H,1′*H*-5,5′-bibenzo[*d*]imidazole (BI) (Figure 3.1), the monomeric unit of PBI mixed with PA using classical all atomistic molecular dynamics (MD) simulation. Three different systems, which consists of different amounts of PA to cover the whole experimental spectrum of doping level, have been studied here. In addition, pure PA and pure BI simulations have been performed to observe the effect of doping on both BI and PA. The BI to PA ratio was varied in the mixed systems as 1:4, 1:8, and 1:14. It is well accepted that the conductivity of PA doped PBI membrane increases with an increase in the amount of PA in the system at higher temperatures. Since there were no optimized force field available for the monomer, BI or the polymer PBI, we have calculated few parameters for the force field, e.g., charges and dihedral angles for BI, and adopted other parameters from literatures. Our objective is to understand the molecular level structural arrangements of BI and PA molecules, which is directly correlated to the conduction of protons. Such understanding at the molecular level is highly desirable in the fuel cell community. Though the polymeric form of BI, i.e., PBI, has not been considered in the present chapter, this work on the BI-PA mixtures serves the purpose of understanding the underlying structural arrangement of BI in presence of PA and vice versa.

3.2 Computational details

We have performed MD simulation using all atom force-field on pure BI, pure PA, and BI mixed with varying amounts of PA systems. The chemical structures of BI and PA are shown in Figures 3.1(a) and 3.1(b) respectively.

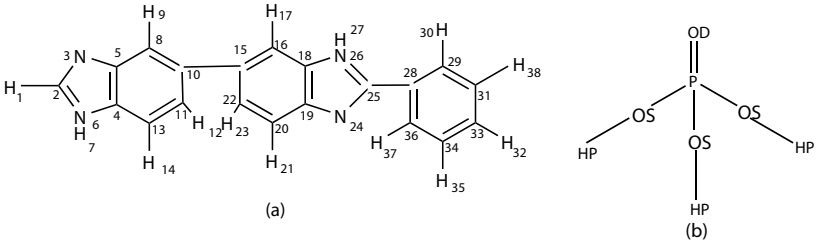

FIGURE 3.1: Chemical structure of (a) monomer unit (BI) of PBI and (b) PA.

All the simulations were performed with the GROMACS 4.0.7 package. [135, 136] A simulation cell containing 125 molecules of BI was constructed for pure BI. For pure PA, 1000 molecules were simulated. In mixed systems, a fixed amount of monomer,

i.e., 64 molecules of BI, were mixed with PA in three different ratios: 1:4, 1:8, and 1:14 according to the number of molecules, i.e., per monomer molecule.

3.2.1 Force field

The total potential energy used in the simulation is the sum over all intra-molecular and inter-molecular interactions. The intramolecular interaction energy consists of harmonic bond, angle potential, proper and improper dihedral potential. The nonbonded interactions energy consists of Lennard-Jones potential and electrostatic interaction. All these potential energy forms were used as implemented in GROMACS. The bond and angle potential parameters for BI were taken from the OPLS-AA force field. [119, 137] The calculation of dihedral potentials for BI were done as follows: we optimized the BI molecule using the Hartree-Fock method with 6-311g basis set by using the Gaussian09 program. [138] A dihedral scan was performed for 20 steps with an increment of 18° in each step. At each step, the geometry of the molecule was optimized, and the energy value was calculated as a function of dihedral angle and fitted by the dihedral potential function of the form

$$V = \frac{k_{\tau_p}}{2}\left[1 - cos\ p(\phi - \phi_0)\right] \tag{3.1}$$

where k_{τ_p} is the dihedral force constant, ϕ is the corresponding dihedral angle, ϕ_0 is the equilibrium dihedral angle, and p is the periodicity. The calculated parameters (force constant, dihedral angle, and periodicity) were fed in the force-field topology. In Figures 3.2(a) and 3.2(b), the dihedral energies from *ab initio* quantum chemical calculation and fitting of the classical dihedral potential energy function have been shown for C_8-C_{10}-C_{15}-C_{22} and C_{29}-C_{28}-C_{25}-C_{24} (numbering of the atoms are according to Figure 3.1(a)) dihedrals, respectively. The values of Lennard-Jones parameters (σ and ϵ) were taken

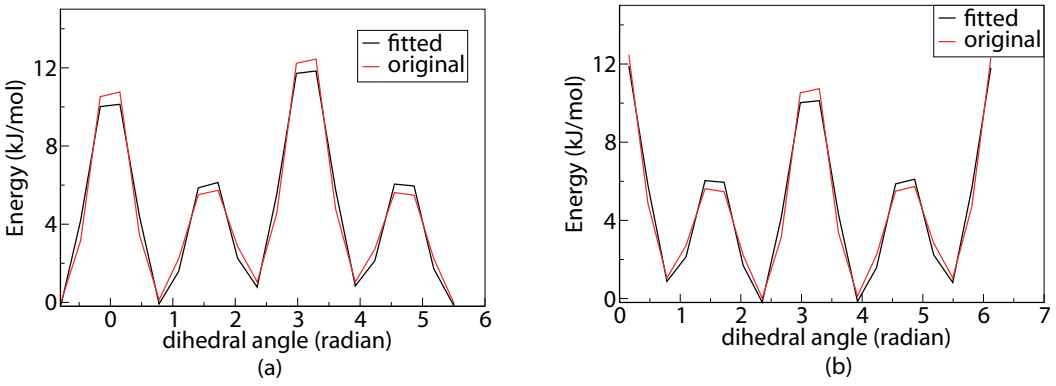

FIGURE 3.2: Dihedral potential fitting of (a) C_8-C_{10}-C_{15}-C_{22} and (b) C_{29}-C_{28}-C_{25}-C_{24}.

from the OPLS-AA force field. The partial charges of the individual atoms are calculated

by quantum chemical calculation using Gaussian09 code [138] and listed in Table 3.1. For this purpose, after geometry optimization, we used the CHELPG [139] method to calculate the partial charges for all the individual atoms of BI.

TABLE 3.1: Charges of the atoms of BI.

Atom number	**Atom name**	**Charge**	**Atom number**	**Atom name**	**Charge**
1	H	0.22	20	C	-0.04
2	C	0.31	21	H	0.19
3	N	-0.50	22	C	-0.18
4	C	0.40	23	H	0.18
5	C	-0.09	24	N	-0.53
6	N	-0.57	25	C	0.44
7	H	0.38	26	N	-1.05
8	C	-0.04	27	H	0.38
9	H	0.19	28	C	0.04
10	C	-0.05	29	C	-0.11
11	C	-0.18	30	H	0.17
12	H	0.18	31	C	-0.19
13	C	-0.02	32	H	0.17
14	H	0.17	33	C	-0.13
15	C	-0.04	34	C	-0.18
16	C	-0.04	35	H	0.17
17	H	0.18	36	C	-0.10
18	C	0.39	37	H	0.21
19	H	0.16	38	H	0.16

All bonded force field parameters including the parameters adopted from OPLS-AA for BI are listed in Table 3.2, 3.3 and 3.4.

TABLE 3.2: Bonded force field parameters for BI (bond parameters).

Bond description	$\mathbf{b_0}$ **(nm)**	$\mathbf{K_b}$ **(kJ/mol/nm^2)**
$C_{benzene}$-$C_{benzene}$	0.140	392459.2
$C_{benzene}$-$N_{attached\ with\ hydrogen}$	0.138	357313.6
$C_{benzene}$-$N_{without\ hydrogen}$	0.139	346435.2
$C_{benzene}$-$H_{benzene}$	0.108	307105.6
$N_{attched\ with\ hydrogen}$-H	0.101	363171.2
$C_{benzimidazole}$-$H_{terminal}$	0.108	307105.6
$C_{benzimidazole}$-$N_{attached\ with\ hydrogen}$	0.134	399153.6
$C_{benzimidazole}$-$N_{without\ hydrogen}$	0.133	408358.4

For all the simulations, NPT ensemble and periodic boundary conditions were used. Temperature was kept constant using a Berendsen thermostat. [131] A Berendsen barostat was used to keep the pressure constant at 1 bar. Reaction field electrostatics [140, 141] was used with a cutoff length of 1 nm. For pure PA, 20 ns production runs were performed at 400, 450, and 500 K. We prepared the system of pure BI at 500 K and

TABLE 3.3: Bonded force field parameters for BI (angle parameters).

Angle description	θ_0 (°)	K_θ (kJ/mol/rad^2)
$C_{benzene}$-$C_{benzene}$-$C_{benzene}$	120.00	527.184
$C_{benzene}$-$C_{benzene}$-$C_{benzimidazole}$	120.00	527.184
$C_{benzene}$-$C_{benzene}$-$N_{attached\ with\ hydrogen}$	108.70	585.760
$C_{benzene}$-$C_{benzene}$-$N_{without\ hydrogen}$	108.70	585.760
$C_{benzene}$-$N_{attached\ with\ hydrogen}$-$C_{benzimidazole}$	109.80	585.760
$C_{benzene}$-$N_{without\ hydrogen}$-$C_{benzimidazole}$	109.80	585.760
$N_{attached\ with\ hydrogen}$-$C_{benzimidazole}$-$N_{without\ hydrogen}$	120.00	585.760
$C_{benzene}$-$C_{benzene}$-$H_{benzene}$	120.00	292.880
$C_{benzene}$-$N_{attached\ with\ hydrogen}$-$H_{attached\ with\ nitrogen}$	118.00	292.880
$C_{benzimidazole}$-$N_{attached\ with\ hydrogen}$-$H_{attached\ with\ nitrogen}$	120.00	527.184
$N_{atached\ with\ hydrogen}$-$C_{benzimidazole}$-$H_{terminal}$	120.00	292.880
$N_{without\ hydrogen}$-$C_{benzimidazole}$-$H_{terminal}$	120.00	292.880

TABLE 3.4: Bonded force field parameters for BI (dihedral parameters).

Dihedral	τ_0 **(degree)**	p **periodicity**	K_{τ_p} **(kJ/mol/rad^2)**
C_4-C_5-C_{22}-C_{23}	50.706	4	0.884984
C_{12}-C_{11}-C_7-C_{33}	57.632	5	1.333620

cooled down in steps of 20 K up to 400 K. At all these intermediate and final temperatures, a 50 ns production run was performed. In the case of mixed systems, simulated annealing for better sampling of the phase space on the energy optimized structure was performed as follows: the initial structures of the mixed systems were taken at 400 K. The systems were gradually heated from 400 to 700 K, by 100 K in each step, and a NPT simulation for 100 ps was performed at each step. Similarly, the system was cooled in three steps from 700 to 400 K. This cycle of heating and cooling was repeated six times. From this cycle, we picked up three mixed systems at three different temperatures (400 K, 450 K, and 500 K), and then, NPT simulations for 50 ns were performed at these temperatures. Although we performed the simulations at three different temperatures, we have presented in this chapter the structural insight of all the systems only at 500 K, as the effect of temperature on the structural arrangement observed is not significant.

3.3 Force field validation

The validation of force field was performed by calculation of density and diffusion coefficient of the pure systems. The calculated density of pure PA at 298 K and 1 atm pressure is found to be 1.855 g/cm^3 and is slightly lower than the experimental value of 1.868 g/cm^3. [142] For pure BI, the calculated density is 1.245 g/cm^3 at 300 K, whereas the reported experimental density is 1.33 g/cm^3 for polymeric BI (PBI), at 308 K and 1 atm. [143] The calculated densities at different temperatures for BI and PA are plotted

in Figures 3.3(a) and 3.4(a), respectively. In the case of pure BI, below 440 K, the rate

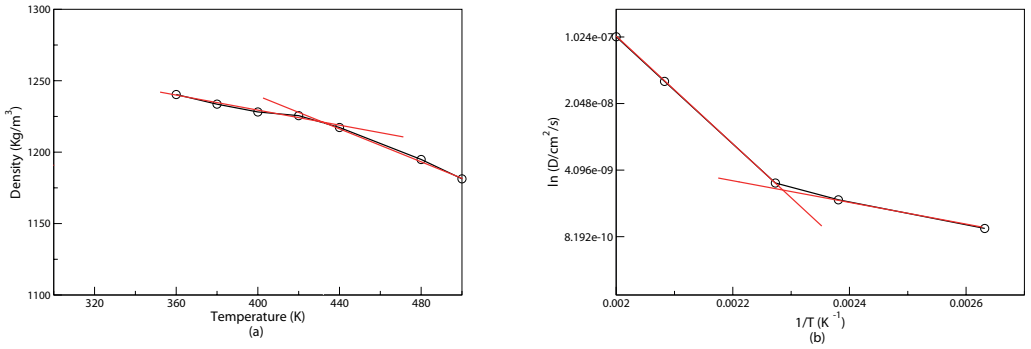

FIGURE 3.3: (a) Density as a function of temperature (b) natural log of diffusion as a function of inverse temperature for BI

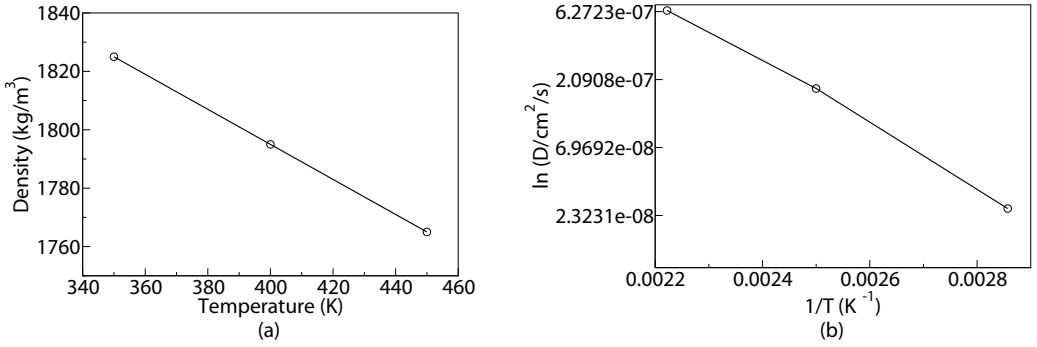

FIGURE 3.4: (a) Density as a function of temperature (b) natural log of diffusion as a function of inverse temperature for PA

of increase in density with a decrease in temperature is less (Figure 3.3(a)). Hence, this particular temperature, i.e., 440 K is near to the glass transition temperature for BI. However, for PBI, the glass transition temperature is reported to be 693 K. [44] From Figures 3.3(a) and 3.4(a), we have also calculated the thermal expansion coefficient for BI and pure PA, respectively, using the following relationship:

$$\alpha = -\frac{1}{\rho}\frac{\partial \rho}{\partial t} \tag{3.2}$$

where α is the thermal expansion coefficient, ρ is the initial density, and $(\frac{\partial \rho}{\partial t})$ is the density change with respect to temperature. The slopes of the Figures 3.3(a) and 3.4(a) plots give us $(\frac{\partial \rho}{\partial t})$ for BI and PA, respectively. For BI, slope was taken above the glass transition temperature (440 K). Dividing the slope by the initial density ρ, we obtained the thermal expansion coefficient. The thermal expansion coefficient at 500

K temperature for BI was calculated to be 50 $\times$ 10^{-5} K^{-1} and for PA is 34 $\times$ 10^{-5} K^{-1}. The calculated diffusion coefficients (D) for pure BI and pure PA at different temperatures are plotted in Figures 3.3(b) and 3.4(b). From the Arrhenius plot (ln D as function of 1/T), we observed in the case of pure BI, deviation from linearity appears below 440 K (see Figure 3.3(b)). Therefore, the density and diffusion values show that around 440 K is the glass transition temperature for BI. However, for pure PA, density gradually increases with a decrease in temperature (Figure 3.4(a)) and unlike pure BI, the plot of ln D vs 1/T for pure PA (Figure 3.4(b)) is linear, which shows that diffusion of PA increases with an increase in temperature. From the Arrhenius plot, we calculated the activation energy for pure BI and pure PA using the following equation:

$$lnD = lnA - \frac{E_a}{RT} \tag{3.3}$$

The activation energy of pure BI was calculated to be 58 kJ/mol and for pure PA to be 44 kJ/mol. Since no experimental data for BI is available in the literature, validation of the calculated properties is done with the polymeric form of BI (PBI). The calculated density of BI is 6.4 % lower than the density of PBI, which is within the limit of deviation of density for a monomer to polymer transition.

3.4 Results and Discussions

The primary motivation of the present work is to understand the structural and dynamical properties of BI in the presence of PA. Different PA content can change the structural arrangement of the BI matrix, which is directly correlated to the H-bond network formation in the system.

3.4.1 Structural properties

The snapshots for all mixed systems are shown in Figure 3.5. A visual inspection of the snapshots show that there is no clear phase separation of BI and PA. This confirms that most of the BI molecules are in contact with PA. We have also performed a NPT simulation for a 1:4 system containing a larger amount of BI and PA (512 BI and 2048 PA) to check the size effect on the phase morphology. In this case, also, we do not observe any distinct phase separation (Figure 3.6). This indicates that the phase morphology of the systems studied is independent of the system size. To investigate the structural arrangements of the BI in the mixed systems compared to the pure BI system, the radial distribution functions (RDF) have been calculated between various atoms of BI. The intermolecular RDFs were plotted between the amine nitrogen (NH, i.e., N_6 and

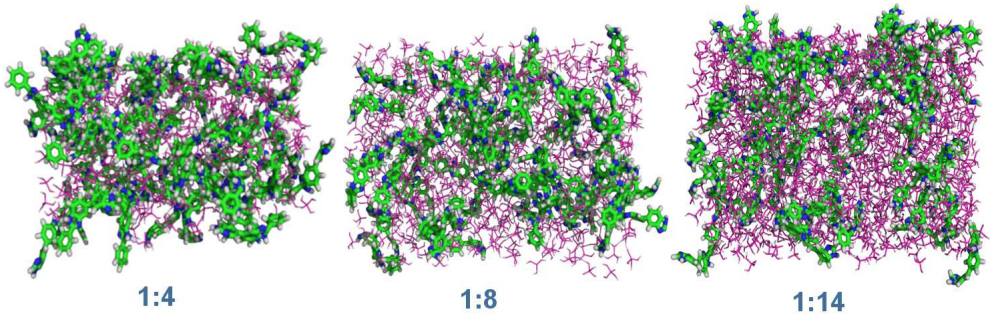

FIGURE 3.5: Snapshots of BI-PA mixed systems (1:4, 1:8 and 1:14).

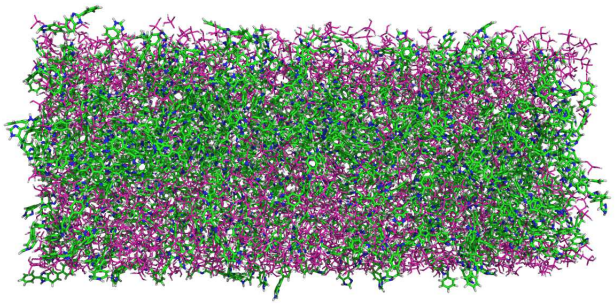

FIGURE 3.6: Snapshot of the 1:4 doubled sized system.

N_{26} according to Figure 3.1(a)) and the hydrogen attached to nitrogen (HN, i.e., H_7 and H_{27} as in Figure 3.1(a)), and between the imine nitrogen (N, i.e., N_3 and N_{24} according to Figure 3.1(a)) and HN for pure and all mixed systems. An examination of the NH-HN RDFs show no clear peaks for any of the systems (Figure 3.7). However, it indicates some distinctions in the arrangement of the BI molecules on going from pure BI to the mixed systems containing a different percentage of PA.

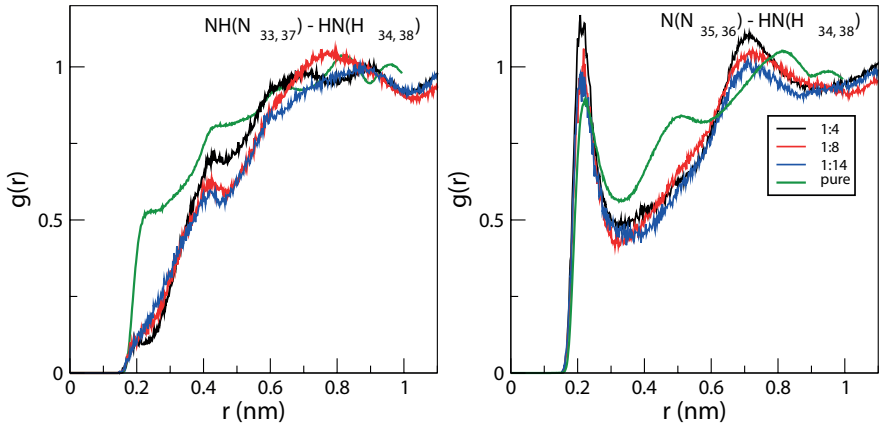

FIGURE 3.7: RDF between various atoms of BI molecules.

The first peaks in the N-HN RDF (Figure 3.7) show the minima at 0.3 nm, which is well inside the H-bonding distance criteria. This is the indication of the presence of intermolecular H-bonding interactions between BI molecules. The peak height is higher in the mixed systems compared to the pure BI system. This signifies higher ordering of BI molecules in the mixed systems compared to the pure BI system. The RDF peak height is the lowest for pure BI and the highest for the 1:4 system. Further, the peak height decreases as we go to higher PA ratio. The 1:4 system shows better ordering for BI molecules than the others. The presence of PA induces the BI molecules to come closer to PA and with an increment in the percentage of PA in the mixed systems, a larger number of PA gets structured around BI. Therefore, the number of BI molecules arranging around each other decreases. The H-bonding among N and HN is an important aspect for such an arrangement.

The structural arrangements of the PA molecules around BI are investigated by checking the RDFs between N, HN, and NH atoms of BI and various atoms of PA for all the mixed systems and depicted in Figure 3.8. Since PA acts as a solvent in the PEM, an

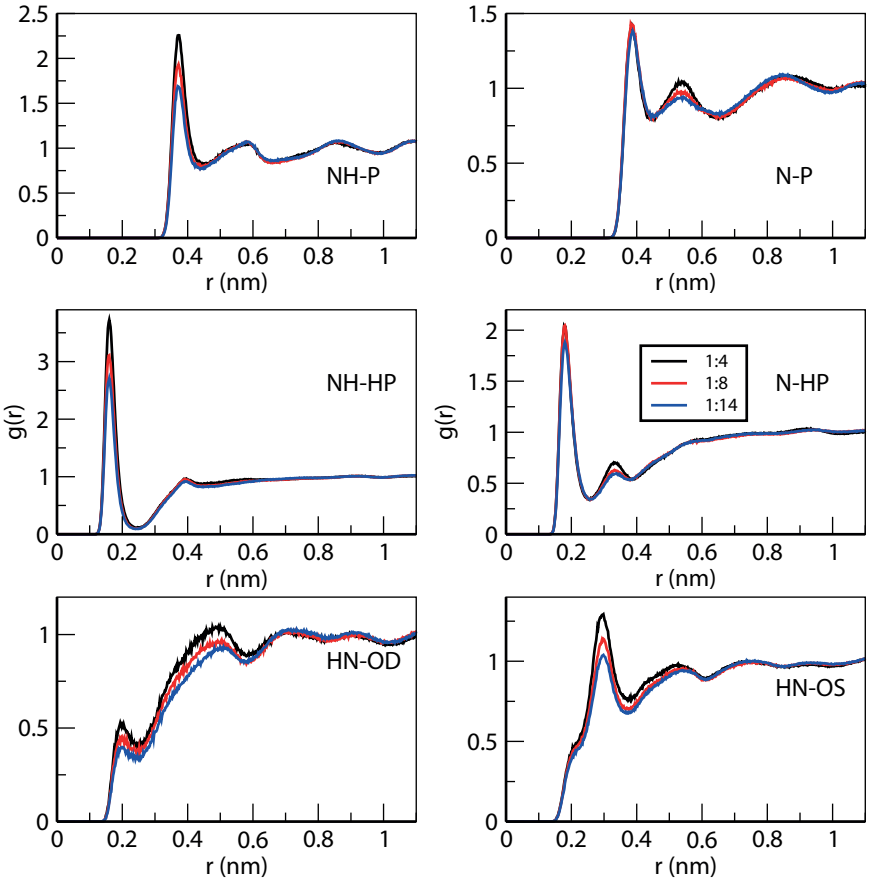

FIGURE 3.8: RDF between various atoms of BI and PA molecules.

investigation of the structural arrangements of PA around BI will provide insights on favorable interaction sites and hence the formation of hydrogen bond networks between

the two components. The RDFs of NH with phosphorus of PA (P) and between N and P signify clustering of PA molecules around imidazole moiety of the BI. There is a drop in the peak height of the NH-P RDFs with an increase in the amount of PA, which shows that ordering of PA molecules around the NH sites of BI is higher at a lower doping level of PA. However, there is not much shift in the peak heights in N-P RDFs with varying amount of PA. Thus, the ordering of PA molecules around the N site of BI is not affected much with an increase in the amount of PA. The RDFs between NH and HP (hydrogen on PA) and also between N and HP are shown in Figure 3.8. These RDFs show the extent of H-bonding interactions between BI and PA. Fairly sharp RDF peaks can be observed with the first minima at the H-bonding distance for all the BI to PA ratios of the mixed systems. This suggests that the PA molecules have an ordered arrangement in order to undergo H-bonding with BI. The NH-HP RDF peaks, and hence the H-bonding interaction decreases with the increase in the amount of PA, but the extent of H-bonding between N and HP is not affected much with a change in the BI to PA ratio. The possibility of the existence of H-bonding is further investigated by calculating RDFs between HN and single bonded oxygen of PA (OS) and double bonded oxygen of PA (OD). RDF peaks between HN and OD are broad and decrease with an increase in the BI to PA ratio. On the contrary, almost no peak at the H-bonding distance is observed for the HN and OS RDF plots. This is rather surprising because both the nitrogen atoms of BI (i.e., NH and N) actively take part in H-bonding interaction, but the extent is much less for double bonded oxygen (OD) and almost nothing for single bonded oxygen (OS) of PA. This is possibly because the highly ordered arrangement of HP atoms around NH hinders the HN and OS to set the proper alignment to undergo H-bonding.

Intermolecular RDFs are also calculated between OD and OS with HP of PA in the mixed systems and compared with the pure PA system (Figure 3.9).

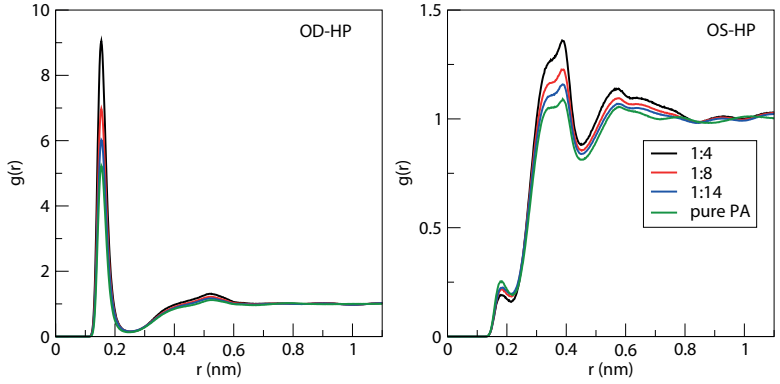

FIGURE 3.9: RDF between various atoms of PA molecules.

The peak heights of the RDF plots between OD and HP decrease steadily with an

increase in the amount of PA in the mixed systems. Peak height is lowest for the pure PA system. It shows that PA forms an H-bonding network (minima of the first peaks are at 0.24 nm) in the mixed system and that this network is better ordered compared to the pure PA system. Further, there are not much change in the first peak heights of the RDF plots between OS and HP, showing that there is not much change in the H-bonding among these atoms with a change in concentration of PA.

3.4.2 Clustering of BI molecules in PA doped BI mixtures

Analysis of the RDF plots showed that a larger number of BI molecules become ordered around each other with an increase in the amount of PA for the mixed systems. To verify this, the clustering of BI molecules has been investigated. To identify the clustering among the BI molecules, the distance between the center of masses (COM) among all the BI molecules were first computed. All the BI molecules for which the distance between the COMs came within 0.95 nm were considered to be a single cluster. This particular distance, 0.95 nm, is the distance of the second solvation shell of a BI molecule (taken from the RDF between BI molecules in pure system), i.e., until this distance, there is probability of a BI molecule to be near the other BI molecules and form a cluster. The cluster sizes, with respect to number of BI molecules, were calculated in each frame of the trajectory separately for all the mixed systems at only 500 K. Finally, the number of occurrences of the cluster sizes, sampled over last 10 ns trajectory, is plotted in Figure 3.10.

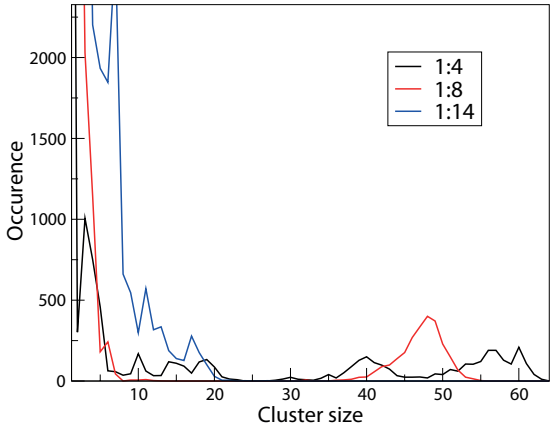

FIGURE 3.10: Cluster analysis of BI molecules in mixed systems.

A higher number of occurrence at a particular cluster size indicates higher probability of formation of cluster of that size in the 10 ns time window. The cluster size of one has the highest occurrence for all the mixed systems, which is obvious because each frame may have few isolated molecules. Figure 3.10 shows that, from smaller to higher PA ratio, the number of occurrence of smaller sized clusters increases. Larger sized clusters

(cluster size more than 20) are almost absent in case of the 1:14 system, but for 1:8 and 1:4 systems, it occurs several times. The probable reason may be in the case of the system with a higher amount of PA, BI is surrounded by a larger number of PA molecules, and because of the favorable H-bonding interaction between PA and BI, BI molecules cannot phase separate completely to become clustered. A snapshot of such situation is provided in Figure 3.11, which shows that PA molecules are interpenetrated in the clusters of BI molecules. However, in the cases of 1:4 and 1:8 BI-PA systems,

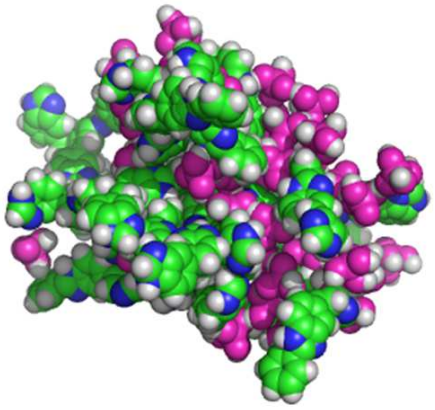

FIGURE 3.11: Cluster analysis of BI molecules in mixed systems.

there are BI clusters, which are large in size but with much less occurrence. As BI clusters are small in size, a continuous proton transport pathway is generated through the intermolecular H-bonding network between PA molecules and also between PA and BI molecules. Since proton transfer hopping between two molecules follows the following order, H_3PO_4 ... $H_2PO_4^-$ > N-H^+ ... $H_2PO_4^-$ > N-H^+ ... N-H, as reported by Ma et al., [93] the contribution of PA dynamics toward long-range proton transport is more than BI; [95] hence, we can expect that, with decreasing the size of the BI cluster as well as increasing the PA-PA association, the proton transfer rate should increase.

3.4.3 Arrangement of Clustered BI Molecules: Stacking

The clustering of BI molecules is observed to decrease with an increase in the amount of PA in the mixed systems. The hopping mechanism of the proton in a PEMFC is strongly dependent upon the arrangement of PBI molecules and also upon the arrangement of PA molecules around it. So the understanding of the arrangement of BI molecules at the structural level would better equip us to deal with the structural arrangements and proton conduction mechanism in the polymeric system. Hence, the issues of how the BI molecules are arranged in the clustered structure and how the arrangement changes with the change in the amount of PA in the mixed systems are important to address. To calculate the arrangement, a vector between H_1 and H_{32} (see Figure 3.1(a)) of all

the BI molecules of the system was defined. Then, the angle between these vectors for the BI molecules falling within a distance of 0.95 nm was computed in each frame of the trajectory. The distance criteria were given with respect to the COM of the BI molecules as in the case of cluster calculations. Finally, a distribution was plotted from all these angles normalized over a number of BI molecules falling within 0.95 nm and number of frames (Figure 3.12). This angle distribution was calculated over last 10 ns of the trajectory. A broad distribution can be observed for all the systems ranging from 0°

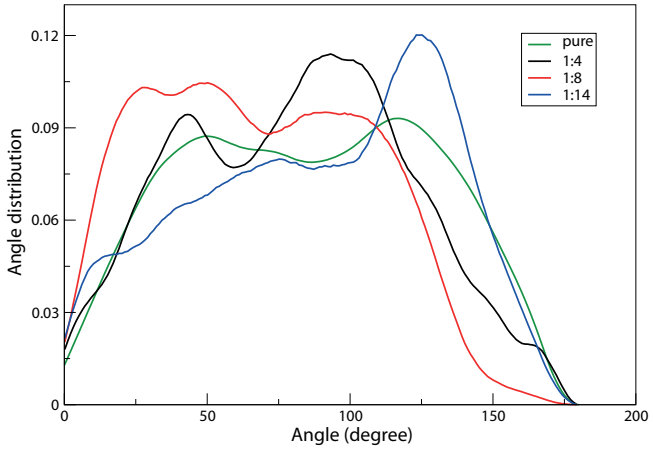

FIGURE 3.12: Angle distribution for BI molecule in pure BI and all the mixed systems.

to 180° with small humps. Two broad peaks can be observed for the pure, 1:4, and 1:8 systems. Also the peaks are more prominent for the 1:4 and 1:8 systems as compared to the pure BI system. This indicates the presence of two different conformations in two mixed systems. Also, the probability of these conformations becomes more significant in the 1:4 and 1:8 systems compared to the pure system. Thus, it can be inferred that the presence of PA caused biasness toward these conformations for BI molecules. However, for the 1:14 system, only one distinct hump can be observed near 150°. Thus, at the highest doping level of PA, at which conductivity has been observed to be maximum, the BI molecules prefer to remain in a nearly parallel conformation with respect to each other. To better visualize the conformational biasness, snapshots extracted from real time trajectory containing two BI molecules in nearly parallel and nearly perpendicular arrangements are depicted in Figure 3.13.

This distinction in the arrangement of BI molecule from 1:4 and 1:8 ratios to 1:14 ratio possibly helps in the proton conduction mechanisms of the PEMFC. This, however, is a matter of further investigation.

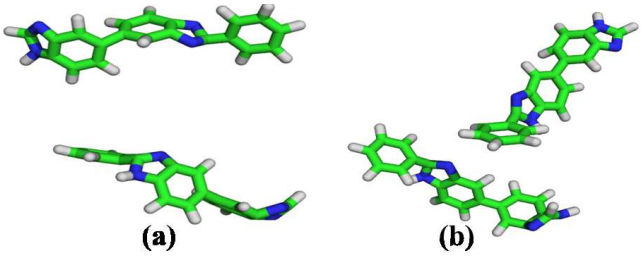

FIGURE 3.13: Snapshot of (a) parallel and (b) perpendicular orientation of BI molecules.

3.4.4 Ring Flipping

Further, to see the effect of stacking and H-bonding on the intramolecular rotation of BI molecules, the dihedral angle connecting two benzimidazole moieties, i.e., C_8-C_{10}-C_{15}-C_{16} (atom numbers as in Figure 3.1(a)) is calculated, and a dihedral distribution plot is given in the Figure 3.14.

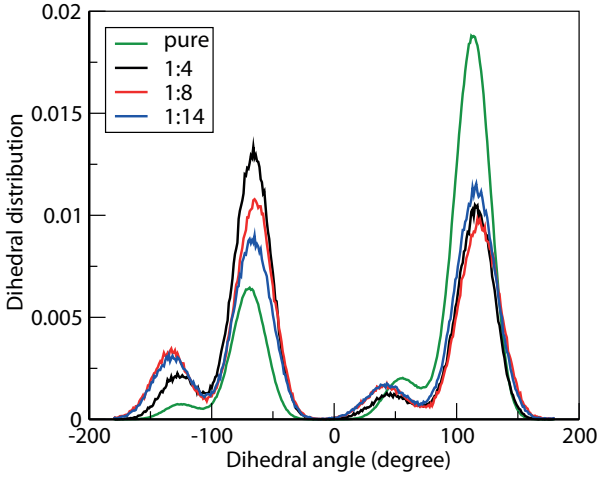

FIGURE 3.14: Distribution for C_8-C_{10}-C_{15}-C_{16} dihedral angle of BI molecule.

The flipping of the same dihedral of BI molecules were counted in each frame of the trajectory with respect to the angle between vectors connecting N_6, H_7 and N_{26}, H_{27}. Flip was considered when the difference of the angle between the vectors was greater than 110° or less than -70° in consecutive frames taking into consideration the peak position in the dihedral distribution plot (Figure 3.14). The occurrence of flip count is shown in Figure 3.15. These occurrences for systems with different ratios of BI to PA were obtained from the last 10 ns trajectory of the production run and averaged over a number of BI molecules present in the system. The flipping is clearly observed to be very frequent in the case of the pure system, but the mixed systems do not have a large affinity for flipping. The smaller flipping tendency in case of the mixed systems can again be attributed to the H-bonding with PA. Though H-bonding among the BI

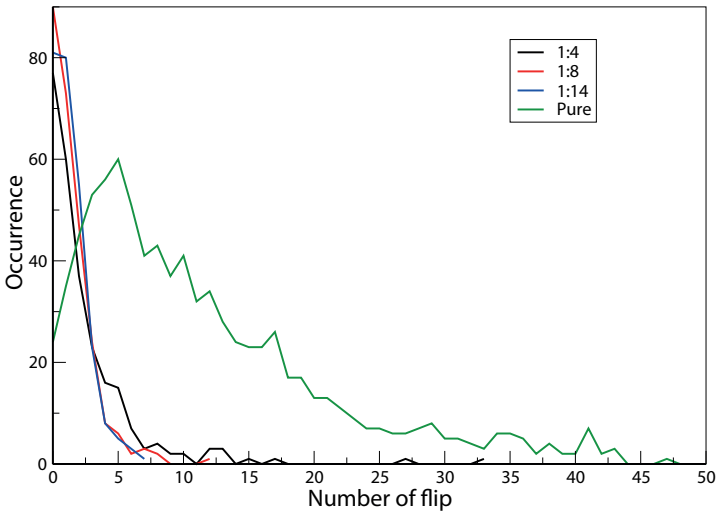

FIGURE 3.15: Occurrence of flipping per molecule over the 10 ns trajectory.

molecules exists in the pure BI system, such H-bonding is not as strong and networked as with the PA in the mixed systems. Also, the absence of peaks at 0° or 180° in the stacking angle (Figure 3.12) can also be understood from flipping. The lesser tendency of the BI molecules for flipping in any of the mixed systems indicates the biasness toward a particular orientation of the BI molecules due to the presence of PA.

3.5 Conclusions

The structural properties of BI-PA mixtures at different doping levels of PA have been investigated using classical MD simulations. The mixture does not phase separate in any of the mixed systems. PA molecules were observed to form highly ordered H-bonded structures among themselves and also with the BI at all the BI to PA ratios. This ordering of PA around BI molecules increases with the increasing amount of PA. Cluster formation among the BI molecules was analyzed, and the cluster sizes of BI were observed to decrease with the increase in the PA doping level. This enables the H-bonding between PA and BI to be more feasible. The BI molecules were also observed to undergo stacking interactions and arrange in parallel and perpendicular orientations among themselves. However, there is significant probability of the BI molecules to orient themselves at any angle among themselves. All these understanding will be useful to address the proton conduction in a PEMFC at its structural level. The present study gives us ample scope to be extended to PBI and hence better understanding of proton conduction at the structural level. The present study can be treated as a benchmark for characterizing structural properties exploring new membrane materials.

Chapter 4

Evidence of dynamic heterogeneity in binary mixture of BI and PA[1]

4.1 Introduction

It is essential to investigate the structural and dynamical properties of the membrane to understand the proton transfer process through it. In the previous chapter, we had studied the structural arrangements of BI and PA and the influence of the amount of PA on it. The binary system of BI-PA was found to be strongly hydrogen bonded(H-bonded) which is necessary for proton transfer. As the performance of the fuel cell is dependent on the extent of proton conduction through the membrane, so it is important to understand the correlation between the H-bonds and dynamics of each component of the binary system, which will contribute to the know-how in designing new membranes. Therefore, in this chapter, we have investigated the nature of vehicular motion of BI as well as PA and the influence of PA doping level on it. This chapter presents a strong correlation between structural arrangements of BI and PA and their dynamics.

In membrane, proton is transported following the path of H-bond network and by diffusion of the protonated species. In this BI-PA mixture any molecule can be surrounded by same, different, or both types of molecules. In aforementioned situations, the mobility of the molecules in their individual phases may differ. So, there is possibility of existence of correlation between structural properties (mainly H-bonded network) and dynamical

[1]This chapter is adapted from the publication Swagata Pahari and S. Roy, Evidence and Characterization of Dynamic Heterogeneity in Binary Mixtures of Phosphoric Acid and Benzimidazole, J. Chem. Phys., 2013, 139, pp 154701-154706

heterogeneity (DH), which arises when the mobility of molecules become different. DH is expected in each component in nonhomogeneous mixtures. Therefore, presence of DH may either reduce or increase the conductivity of the membrane because of slower or faster motion of protonated components, respectively, than the average. This fine-tuning for enhancing the mobility of ions to increase conductivity due to DH will depend upon the concentration of conducting components.

Experimental proof and theoretical concepts of DH in case of polymers and glass-forming liquids are reviewed by Sillescu. [144] Ediger showed that some regions of liquid in glassy state have faster dynamics than other regions separated by few nanometers. [145] Long aliphatic chain ionic liquids show DH which has been correlated to the structural arrangement [146] of aliphatic chains in domains. DH is observed in colloidal particles, [147] ionic liquids, [146] and binary mixture of Lennard- Jones particles. [148] However, to the best of our knowledge DH is not been reported for H-bonded binary system where different types of H-bonding contribute significantly to DH.

The characterization, quantification, and the physical understanding of DH have progressed in recent years. Four-point correlation function is well accepted as standard tool to analyze DH [149] and the direct measurement of this function was done for colloidal and granular materials experimentally. [150] The hopping motion of particle, ion through the system can potentially become clear from the DH study. [151, 152]

Computer simulation is useful to understand DH particularly for identifying cooperative rearrangement among different regions in the liquid. [153–155] Recent MD simulations showed DH in super-cooled model of binary mixture. [156] The correlation between the heterogeneity in structure and dynamics can be achieved by molecular level computer simulation. [157] Weak correlation between local dynamics and local structure was observed from simulations of a polymer melt. [158] Matharoo et al.23 revealed the existence of strong correlation between the mobility and its surrounding particles. However, Berthier and Jack [159] suggested dynamical effect rather than structural arrangement causes DH.

This chapter of the thesis presents first direct observation of DH in a H-bonded network forming system from all atomistic MD simulations of various BI-PA mixtures of varying PA concentration. The starting source of this work is the irregular self-diffusion coefficients of BI and PA molecules with gradual increase in PA concentration. In these mixed systems, the coexistence of fast and slow moving molecules are possible because of H-bonding. The heterogeneity in dynamics may originate from inhomogeneous distribution of complex structural arrangements, which are frequently rearranged by H-bond breaking and making. Therefore, we have analyzed the MD trajectories to find whether

DH is present, if so, in what extent and how it correlates the H-bonding arrangements and its stability.

4.2 Computational methods

We have performed classical MD simulation on BI-PA mixed systems using all atomistic force field. The details of the systems and simulation conditions are given in Ref. [160] All the simulations are performed using Gromacs 4.0.7 [136] molecular dynamics code. For the BI-PA mixed systems we have considered 64 molecules of BI and PA are mixed in different numbers to get ratios, 1:0.12, 1:0.25, 1:0.5, 1:1, 1:2, 1:4, 1:8, and 1:14. Lennard-Jones (LJ) parameters, σ and ϵ, bonds and angles potential parameters of the BI molecules are taken from Optimized Potentials for Liquid Simulations (OPLS) force field. [119] The dihedral potential parameters and partial charges for each atom of BI were calculated from quantum chemical calculations as given in chapter 3. For PA, all the force field parameters are taken from the paper of Spieser et al. [161] MD was done with constant temperature (500 K) and pressure (1 bar) using Berendsen thermostat and barostat. For all the simulations periodic boundary condition and reaction field electrostatics with a cut-off of 1 nm was used. Simulated annealing on the energy optimized structures was performed for 10 ns for better sampling of phase space. Stepwise details of the simulated annealing procedure are as described in chapter 3. After simulated annealing, 100 ns of NPT simulation run was done for all the BI-PA systems. For better statistics we have performed three independent runs of 100 ns each for all the systems with varying PA content.

4.3 Results and discussion

From the MD trajectory of the BI-PA mixtures, we have calculated Mean Square Displacement (MSD) and the self-diffusion coefficients (by using Stokes-Einstein's relation) of BI and PA (see Table 4.1) for all the BI-PA mixed systems containing different amounts of PA performing three sets of simulations. We have plotted the average MSD derived from three sets of simulations for both the BI and PA for each PA ratio in Figures 4.1(a) and 4.1(b), respectively. The calculated diffusion coefficient of BI as well as PA from these MSD plots decreases as we increase the amount of PA till 1:4 BI-PA ratio. However, beyond this ratio the diffusion constant starts to increase sharply with PA concentration. The self-diffusion coefficients (average value deriving from three sets of simulations) of BI as well as PA as a function of PA concentration are plotted in Figures 4.2(a) and 4.2(b), respectively. This anomalous diffusion hinted the presence

TABLE 4.1: Diffusion coefficients ($\times$ 10^{-7} cm^2/s) of BI and PA in various mixed systems of different PA ratio at 500 K.

BI				
System	Set 1	Set 2	Set 3	Average
1:0.12	0.93 ± 0.03	1.06 ± 0.01	0.89 ± 0.03	0.96 ± 0.02
1:0.25	0.80 ± 0.01	0.74 ± 0.04	0.85 ± 0.01	0.79 ± 0.01
1:0.5	0.46 ± 0.11	0.38 ± 0.07	0.51 ± 0.04	0.45 ± 0.06
1:1	0.33 ± 0.05	0.35 ± 0.01	0.30 ± 0.03	0.33 ± 0.03
1:2	0.27 ± 0.01	0.30 ± 0.00	0.28 ± 0.01	0.28 ± 0.01
1:4	0.25 ± 0.00	0.23 ± 0.02	0.27 ± 0.01	0.25 ± 0.01
1:8	0.75 ± 0.01	0.78 ± 0.05	0.70 ± 0.05	0.74 ± 0.02
1:14	1.01 ± 0.14	1.07 ± 0.08	1.12 ± 0.11	1.09 ± 0.07
PA				
System	Set 1	Set 2	Set 3	Average
1:0.12	0.73 ± 0.01	0.80 ± 0.02	0.63 ± 0.02	0.72 ± 0.01
1:0.25	0.60 ± 0.03	0.61 ± 0.05	0.57 ± 0.04	0.58 ± 0.05
1:0.5	0.53 ± 0.01	0.57 ± 0.02	0.49 ± 0.03	0.51 ± 0.02
1:1	0.49 ± 0.02	0.47 ± 0.01	0.42 ± 0.01	0.46 ± 0.01
1:2	0.47 ± 0.01	0.45 ± 0.02	0.39 ± 0.04	0.44 ± 0.02
1:4	0.46 ± 0.01	0.42 ± 0.01	0.36 ± 0.03	0.41 ± 0.01
1:8	1.13 ± 0.04	1.29 ± 0.03	1.18 ± 0.02	1.20 ± 0.03
1:14	3.20 ± 0.07	2.88 ± 0.05	2.91 ± 0.02	2.97 ± 0.04

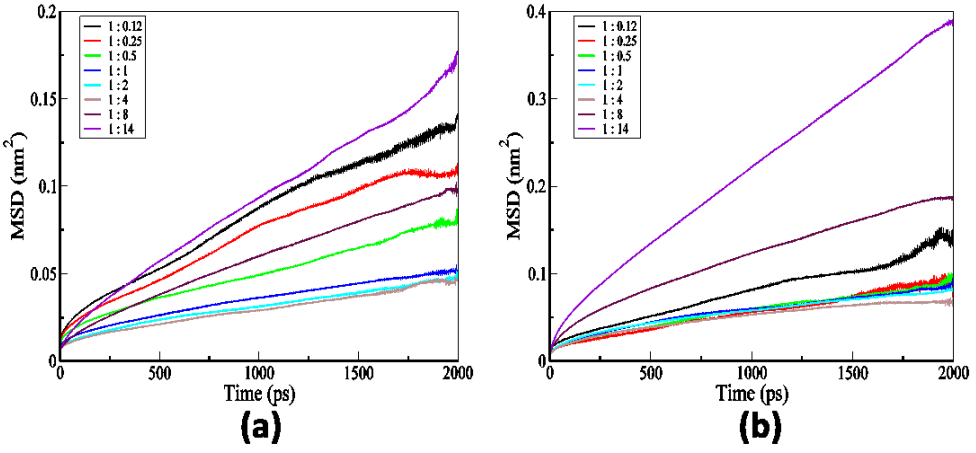

FIGURE 4.1: MSD plot of (a) BI and (b) PA as a function of PA ratio.

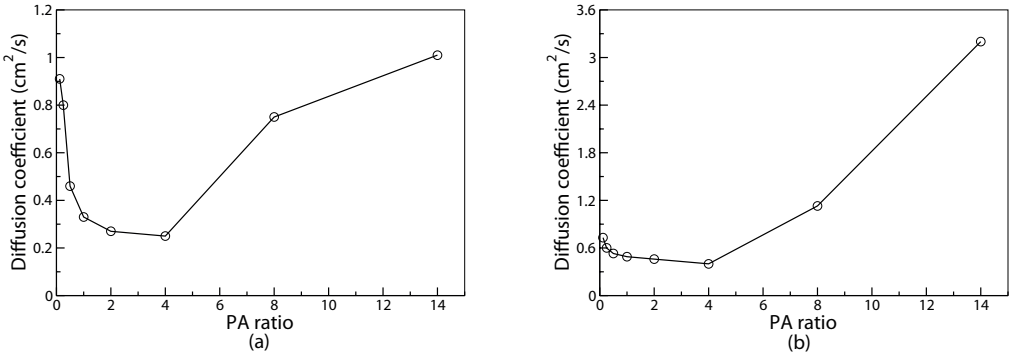

FIGURE 4.2: Diffusion coefficient $\times$ 10^{-7} of (a) BI and (b) PA in BI-PA systems as a function of PA ratio.

of DH in the mixture. We have further investigated this by evaluating the correlation between different types of H-bonding and DH in the systems.

Presence of DH can be tested by calculating self-part of the van Hove correlation (VHC) function $G_s(\mathbf{r}, t)$ as given in the following equation:

$$G_s(\mathbf{r}, t) = \frac{1}{N} \sum_{i=1}^{N} < \delta|\mathbf{r}_i(t) - \mathbf{r}_i(0)| - \mathbf{r} > \tag{4.1}$$

This gives the displacement of the molecule in a time interval t. $G_s(\mathbf{r}, t)$ characterizes particle motion in terms of their relative mobility. If all the molecules follow uniform motion, the distances molecules travel in definite time intervals lead to Gaussian distribution. We have calculated self-part of the VHC function $[4\pi \mathrm{r}^2 G_s(\mathbf{r}, t)]$ as a function of $\mathbf{r}$ at time interval of 1 ns for all mixtures. Deviation from the Gaussian form is observed for all the mixtures confirming the heterogeneity in the dynamics of PA molecules. The deviation from the Gaussian behavior is characterized by the non-Gaussian parameter $\alpha_2(t)$, [146, 153] which is defined as

$$\alpha_2(t) = 3 < r^4(t) > /5 < r^2(t) >^2 -1 \tag{4.2}$$

The value of $\alpha_2(t)$ becomes zero when the dynamics of the system is homogeneous, the value increases with the increase in DH in the system and it becomes maximum when the system touches maximum heterogeneity in dynamics. We have calculated $\alpha_2(t)$ as a function of time and located the time (t^*) corresponding to the maximum value of α, i.e., maximum heterogeneity in the system. The VHC function, $[4\pi r^2 G_s(\mathbf{r}, t)]$ calculated at t^* as a function of $\mathbf{r}$ for different PA ratio is shown in Figures 4.3(a) and 4.3(b) respectively.

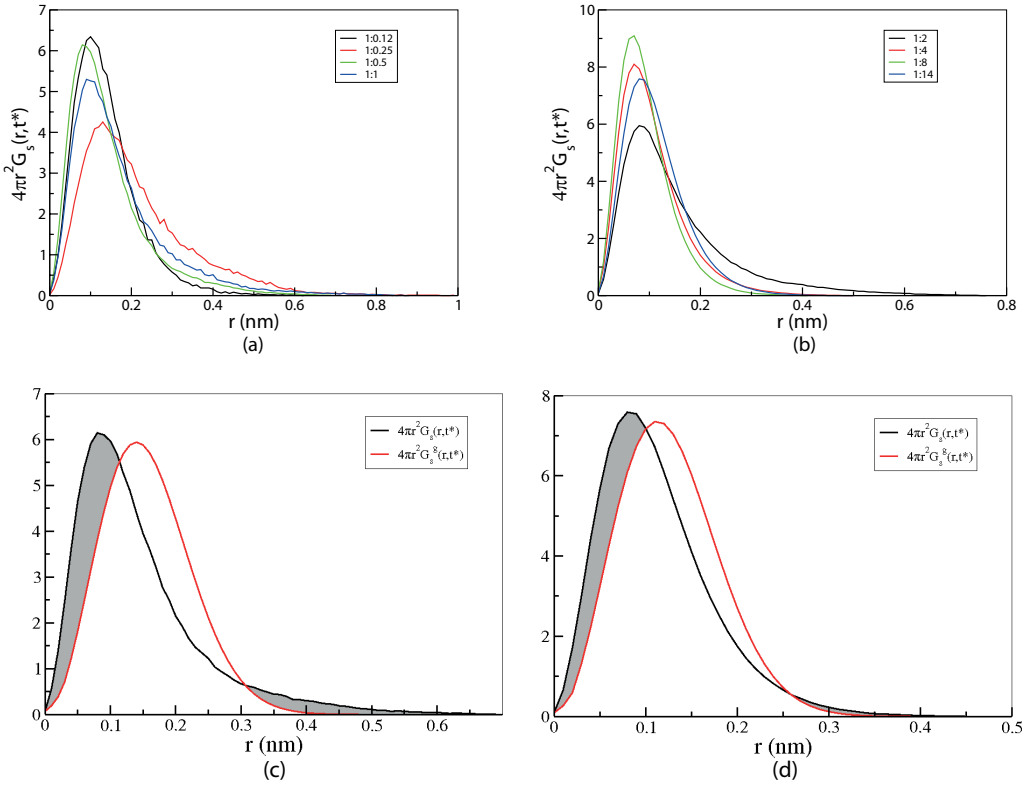

FIGURE 4.3: Self-part of van Hove correlation function $[4\pi r^2 G_s(\mathbf{r},t)]$ of PA in presence of different PA ratio calculated at t ((a) and (b)) and comparison of $[4\pi r^2 G_s(\mathbf{r},t)]$ and its Gaussian form for (c) 1:0.5 and (d) 1:14 BI-PA system.

For quantitative analysis of DH we compared self-part of VHC function, $[G_s(\mathbf{r},t))]$ with the ideal Gaussian distribution, $[\ G_s^g(\mathbf{r},t)]$ [146] for each of the BI-PA system

$$G_s^g(\mathbf{r},t) = \left[\frac{3}{2\pi < r^2(t) >}\right]^{3/2} exp\left[-\frac{3r^2}{2 < r^2(t) >}\right] \tag{4.3}$$

where $< r^2(t) >$ in the above equation is the MSD.

The comparison between $G_s(\mathbf{r},t)$ and $G_s^g(\mathbf{r},t)$ of PA for 1:0.5 and 1:14 (BI-PA) system are shown in Figures 4.3(c) and 4.3(d), respectively. Deviation from Gaussian is observed in both the plots in short as well as long range. The molecules at short and long distance are moving slower and faster, respectively, than what is predicted for homogeneous system. For quantitative estimation of the percentage of molecules whose motion differ from the ideal Gaussian motion, we have calculated the regions where $G_s(\mathbf{r},t)$ deviates from $G_s^g(\mathbf{r},t)$ as shown by Carbone et al. [162] These regions are identified (as depicted in Figures 4.3(c) and 4.3(d)) between zero and first crossing point, which defines slow molecules, and between second crossing point and infinity, which corresponds to fast

molecules. The percentages of slow and fast PA molecules are calculated (reported in Table 4.2) by taking the integral of the corresponding areas indicated by shadows.

TABLE 4.2: Percentage of fast and slow PA molecules in different PA concentration.

System (BI:PA)	percentage (%) of fast PA molecules	percentage (%) of slow PA molecules
1:0.12	15.0	2.4
1:0.25	15.7	5.3
1:0.5	18.9	5.5
1:1	19.7	5.7
1:2	20.6	7.1
1:4	16.4	2.8
1:8	15.8	1.8
1:14	14.7	1.4

For low PA concentrations both the slow and fast moving PA molecules are increasing but till 1:2 (BI:PA) system and beyond 1:2 ratio percentage of both fast and slow PA molecules decreases with the increase in PA concentration.

In Figure 4.4, we have depicted a snapshot of 1:2 BI-PA system. It is clear from the Figure that there is no clear phase separation between PA and BI.

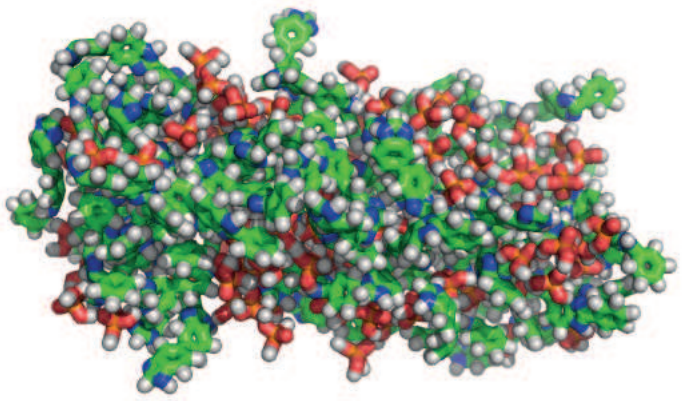

FIGURE 4.4: Snapshot of a BI-PA (1:2) system.

In case of all other mixtures with different ratios BI to PA, we have observed similar phase separation. So, different neighbors are present surrounding the molecules of the mixtures. Therefore understanding the structure of the micorphases, which are interacting via H-bonding can help in correlating it to the DH. Hence, we have explored the structural

arrangement by investigating H-bonding of PA near BI and studied whether this type of arrangement hinders or assists the dynamics of PA. We have started our exploration by calculating the number of PAs which has different H-bonding situations, i.e., (i) PAs making H-bond with only one Nitrogen (N) of BI (s-bond), (ii) PAs making two H-bonds with two N atoms of two BI (d-bond), and (iii) PAs making three H-bonds with three N atoms of three BI (t-bond). We have used H-bond criterion of distance (between N and H less than or equal to 0.25 nm) and additionally angle (between O, H of PA and N greater than 150°). The snapshots of these arrangements of BIs and PA taken from real time trajectory are shown in Figure 4.5.

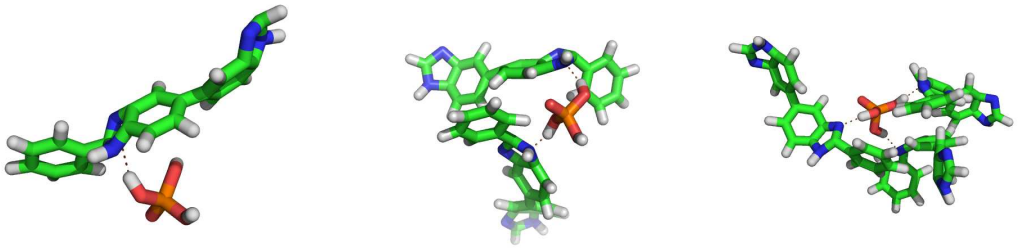

FIGURE 4.5: Snapshot of formation of (a) s-bond, (b) d-bond, and (c) t-bond, respectively, extracted from real trajectory.

We have plotted the number of PAs acquiring these three types of arrangements as a function of PA ratios separately in Figure 4.6. PAs forming only s-bond increases with increase in the PA ratio (Figure 6(a)) and the number is higher than other two types of PAs (forming d and t-bonds shown in Figures 4.6(b) and 4.6(c), respectively).

There is also increase in PAs, making d- and t-bonds with PA concentration but till 1:4 system and beyond this the number decreases. PAs with d- and t-bonds are acting as bridge between different BIs (see Figure 4.5). The PAs with only s-bond have bond with one BI and free to form two other H-bonds with other PAs. Therefore, with increases in PA concentration, number of PAs forming H-bonds with PA increases than number of PAs forming H-bonds with BI. For lower PA ratios (1:0.12 - 1:4) there are also increase in the number of bridging PA though these are less in number than the PAs forming s-bond. Due to bridging H-bond formation, molecules become slower relative to the average dynamics of PAs, whereas formation of PA-PA bond makes the molecules faster than average PA dynamics as the PA-PA dynamics is faster than BI-PA dynamics. To understand how this type of bridging bond affect the solvation shell of PA with varying PA concentration, we have calculated the coordination number of each type of PA molecule (making s-bond/d-bond/t-bond) separately for each BI-PA mixed system. We have defined coordination number of a molecule as the numbers of molecules which are coming within the first solvation shell of that molecule. The calculations are done over

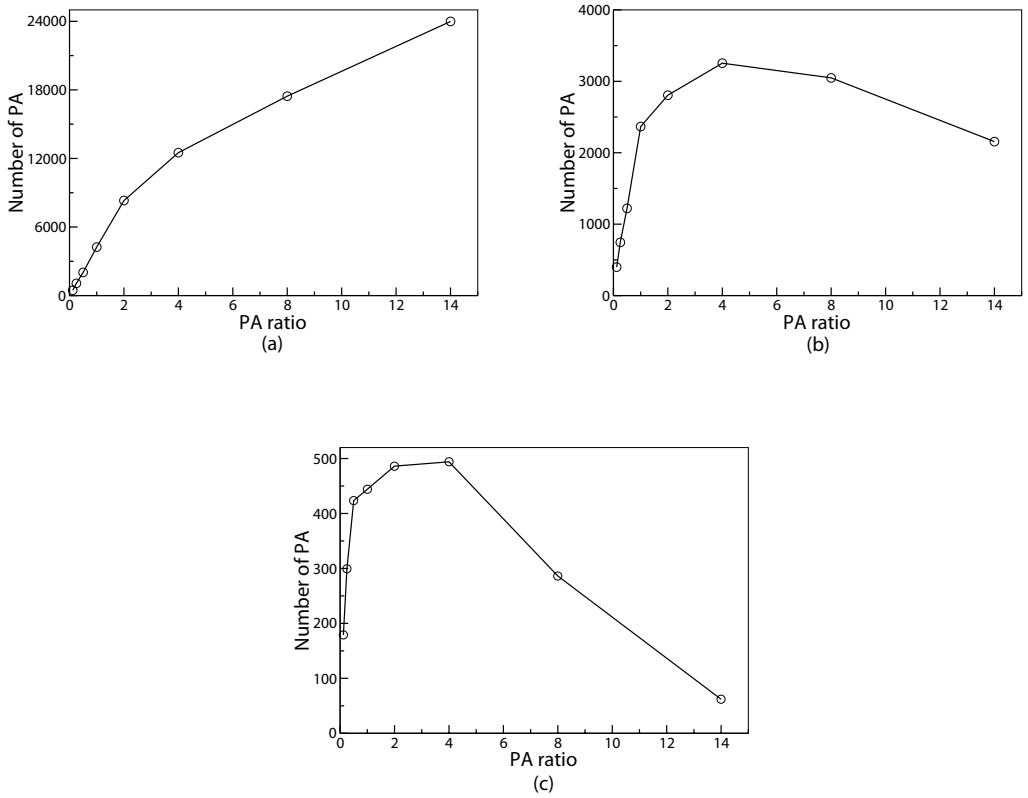

FIGURE 4.6: The number of PAs forming (a) s-bond, (b) d-bond, and (c) t-bond with BI, respectively, as a function of PA ratio.

last 10 ns trajectory of the simulation. In each time frame, we normalized the coordination number by number of such PA molecules (making H-bonds of type s-bond/d-bond/ t-bond) present at that particular frame. Then average coordination numbers from 10 ns trajectories for each type of PA molecules at different PA concentrations are given in Table 4.3.

TABLE 4.3: Coordination number of PA (which are H-bonded with BI) with PA.

System (BI:PA)	**No. of PA (s-bond)**	**No. of PA (d-bond)**	**No. of PA (t-bond)**
1:0.12	0.91 ± 0.26	0.96 ± 0.24	0.98 ± 0.21
1:0.25	0.98 ± 0.31	1.02 ± 0.39	1.07 ± 0.37
1:0.5	1.16 ± 0.20	1.23 ± 0.23	1.30 ± 0.21
1:1	1.20 ± 0.07	1.24 ± 0.11	1.82 ± 0.08
1:2	1.91 ± 0.19	2.05 ± 0.23	2.37 ± 0.27
1:4	2.92 ± 0.28	2.66 ± 0.33	2.53 ± 0.30
1:8	3.55 ± 0.37	3.11 ± 0.31	2.65 ± 0.39
1:14	4.25 ± 0.15	4.13 ± 0.11	3.97 ± 0.19

The coordination numbers of PA molecule (H-bonded with BI) increase with the amount of PA. Therefore, number of PA-PA bond increases with PA content irrespective of the

number of BI present in the close proximity. We have also calculated the coordination number of those PA molecules which are outside the solvation shell of BI at different PA concentrations and reported in Table 4.4. The coordination numbers of these molecules are also increased with increase in PA content and at the highest PA concentration (i.e., BI-PA of 1:14), the size of PA solvation shell resembles pure PA system.

TABLE 4.4: Coordination number of PA outside the solvation shell of BI.

System (BI:PA)	**Number of PA molecules**
1:0.12	1.4 ± 0.12
1:0.25	2.3 ± 0.28
1:0.5	2.7 ± 0.22
1:1	3.0 ± 0.09
1:2	5.8 ± 0.13
1:4	8.1 ± 0.21
1:8	9.4 ± 0.35
1:14	10.1 ± 0.19
Pure	10.2 ± 0.17

The size of the PA solvation shells (which are not having BI molecules in their solvation shell) also get affected due to the presence of BI molecules in the system. So, the number of PA-PA bond increases with increase of PA content. Therefore, percentage of fast molecules also increases with increase in the PA ratio. Beyond 1:2 system, PA molecules are higher in number compared to BI molecules, produces more PA-PA H-bond. The dynamics of these PAs contribute to the average dynamics of the system. The PAs forming H-bonds with BI attain slower dynamics compared to the average dynamics of PA. As we go from 1:2 to 1:14 system, with increase in the number of PAs (see Tables 4.3 and 4.4 for solvation shell sizes), PA-PA H-bond increases and d-bond and t-bond (bridging bonds) decreases. Although number of s-bond between BI and PA increases with PA concentration but increase in PA-PA bond is much higher in number (as the size of the solvation shell of PA also increases). Therefore, percentage of slower PA molecule decreases as we go from 1:2 to 1:14 system. There are negligible percentages of faster PA molecules in the systems of higher PA ratio (1:4, 1:8, and 1:14) and it decreases with increase in PA concentration because the average dynamics of PA in the system is dominated by the high number of PA H-bonded to PA. Therefore, DH in the BI-PA system is due to the formation of different types of H-bonded structures, which causes different mobility.

The stability of these H-bonds was estimated by calculating the lifetime of each type of bonds (s-, d-, t-bonds) formed by PA with BI separately and depicted in Figure 4.7. The lifetime of a bond is generally defined as how long that bond exists before breaking. To calculate the lifetime, we took into account each type of H-bond separately and checked the existence of that H-bond in the consecutive time frames and recorded the time. The

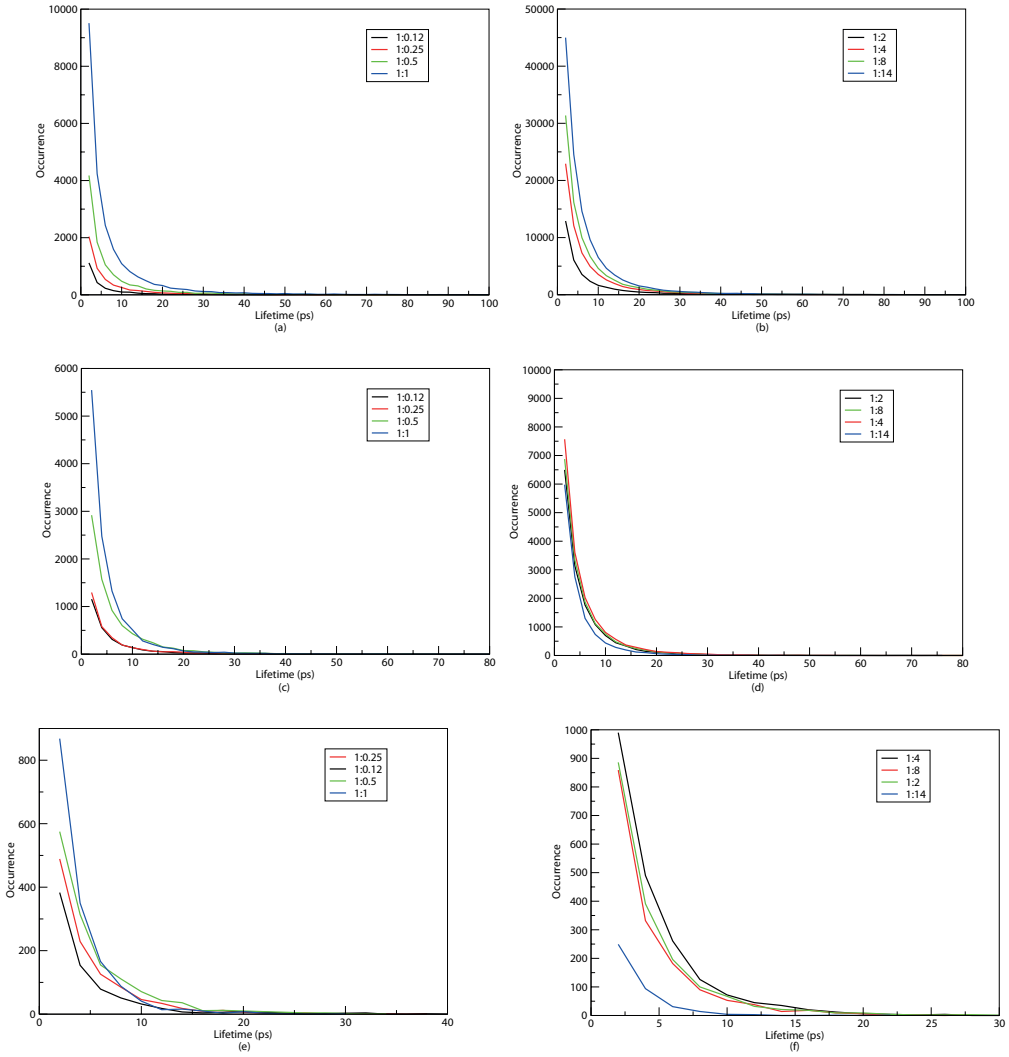

FIGURE 4.7: The occurrence of lifetime of s-bond (a) and (b), d-bond (c) and (d), and t-bond (e) and (f), respectively, with varying PA concentration.

distribution of lifetime for each type of H-bond calculated over last 10 ns trajectory is shown in Figure 4.7. From these exponential decaying plots, it is clear that the order of lifetime is s-bonds > d-bonds > t-bonds. The lifetime of s-bond and its occurrence gradually increases with PA. For d- and t-bonds, the occurrence of lifetime increases with increase in PA till 1:4, beyond that occurrence decreases as expected from H-bond occurrences (Figure 4.7). Lifetime of d- and t-bonds do not change significantly with PA ratios. The lifetime of three types of H-bonds suggest that PA prefers to form stable H-bond with one BI rather than two or three BIs and this gets more prominent with higher PA concentrations. The PAs that form s-type of bonds with a BI may form H-bonds with PA molecules using its other two H atoms. In this type of structural arrangement of BI-PA system, proton prefers to hop more from PA to PA rather than BI to PA since the energy barrier for proton transport has the order: PA-PA < BI-PA < BI-BI as suggested by Li et al. [97] As the occurrence of s-bond increases with increase

in PA ratio, proton transport also increases (fast moving PA) as the preferable pathway (PA-PA) becomes more in number. The overall short lifetime of H-bonds makes the H-bonded network flexible and frequent changes of surroundings around PAs make these molecules dynamically heterogeneous.

4.4 Conclusions

Our molecular dynamics simulations on BI-PA binary systems demonstrate that the diffusivity of PA molecules are spatially heterogeneous in the structurally heterogeneous system. Our analysis explained how the different regions of varying mobility emerged in the system. Different microscopic pictures of the DH and its qualitative as well as quantitative variation with different PA concentrations are examined. The correlation between H-bonded structure and DH has been established from our analysis. We have also checked the solvation shell sizes for PAs with different H-bonding situations with BI and PA molecules which are not H-bonded with BI. Size of the solvation shell of PA which is not H-bonded with BI also gets altered because of the presence of BI in the system. However at higher concentration of PA the solvation shell size of PA is same as pure PA system. DH can be originated from other source also like confinement. In our calculations we got the total DH, which is sum of all contributions, i.e., hydrogen bonding, confinement and to certain extent temperature. However, we have only correlated our results to the different possible H-bonding situations. In this type of system we believe that the H-bonding contributes maximum to the DH, but it is matter of further investigations.

Chapter 5

Comparative structural and conformational properties of Polybenzimidazoles

5.1 Introduction

After understanding the structural and dynamical properties of PA doped BI system, served as a model system, in chapter 3 and chapter 4, we extended our study to the polymeric form of BI. In the present chapter, we investigated the structural and conformational properties of ABPBI and PBI, two most promising membrane materials of polybenzimidazole family, in presence of PA. This will enable us to reveal the microscopic structures responsible for experimentally observable properties. The effect of conformations of polymer and the arrangements of solvent along the backbone of the chain on proton conduction are investigated.

The key of proton transport in ABPBI and PBI depends on their impregnation into PA. [49, 101, 102, 163] These polyelectrolyte materials are less expensive compared to Nafion, no humidification is required for PEMFC application and working temperature is also high (upto 200 °C). PBI is the first and most investigated one [25, 54, 94, 164, 165] of these benzimidazole based polymers although ABPBI is also equally competent. Wainright et al. [47] first showed that PA doped PBI can be used as a replacement for Nafion membrane at higher temperature in PEMFC with various fuels. [166–168] Similarly, ABPBI with certain concentrations of PA also performs as an efficient membrane [56, 169–171] for PEMFC. ABPBI was first synthesized by Vogel in 1961. [172] Litt et. al. first casted PA impregnated ABPBI membrane from an EtOH/NaOH solution and they found that ABPBI absorb more PA than previously known PBI. [49] Unlike

PBI, ABPBI does not contain the phenylene ring in the backbone. This structural difference of ABPBI may give rise to better affinity towards PA compared to PBI. However, ABPBI is the simplest of all the benzimidazole types of polymers as it is prepared from a simple, comparatively inexpensive, commercially available monomer. [170, 171, 173] Besides that, doping of ABPBI with a given amount of PA leads to more acid uptake compared to PBI. [56, 173] Since the acid provides hydrogen ion mobility, conductivity increases as the percentage of acid increases. Another key feature of ABPBI is its high thermal stability. Concerning the mechanical properties of these membranes, Wainright et al. reported that mechanical strength of comparably doped PBI and ABPBI films are almost same. But synthesis of higher molecular weight ABPBI is achievable, which yields higher elongation and toughness. [56] Litt et al. [49] studied the mechanical properties of PBI and ABPBI as a function of their inherent viscosities. They found that within high viscosity range, ABPBI film is much tougher and more elongated than the PA doped PBI film. Despite of these advantages of ABPBI over PBI, it has not been considered widely because of some critical drawbacks. [173] One of them is its poor solubility in common solvents, which are generally used in membrane casting method in solution. Another important disadvantage of ABPBI is that the mechanical strength of the polymer decreases with the increase in PA content. In case of ABPBI, the loss of mechanical strength is more than PBI because it gets dissolved more readily in PA due to its higher basicity.

Savinell and coworkers [174] first observed the high conductivity of PA doped PBI. The PBI membrane with a higher doping level (27.7 mol/RU) exhibits proton conductivity of 0.24 S cm^{-1} at 160 °C. ABPBI membrane with acid doping level of only 2.5 mol/RU shows proton conductivity of 0.14 S cm^{-1} at 180 °C. [57] Asensio and coworkers [56] have reported that PA doped ABPBI exhibits better proton conductivity than PBI because of the presence of higher imidazolium group concentration per unit volume of ABPBI, resulting in increasing capability of dissolving acid and thus higher proton conductivity.

Not many computational studies on properties and proton conductance mechanism have been performed on polybenzimidazole (PBI and ABPBI) membranes. [43, 97–100] This is primarily because of its complexity and higher length and time scale of the system. Shuo et. al. [97, 98] studied the structural and electronic properties of monomers of PBI and ABPBI as well as PA in order to explore the nature of hydrogen bonding (H-bonding) interaction and the energy barriers for different proton transport pathways within PA-doped olybenzimidazole. Authors reported the proton affinities of benzimidazole, PA, water and their corresponding ions and categorized them based on their ability to associate a proton. They also found that at lower doping level of PA, there is a formation of strong H-bond between PA and polymer chain. The activation energy barrier for various proton transport pathways suggest that the excess proton moves to

benzimidazole after the initial optimization. The H-bond between PA and benzimidazole is the major interaction in PA solvated polybenzimidazole at lower PA doping level. They have also performed classical molecular dynamics (MD) simulation on neat, hydrated and PA solvated PBI and ABPBI and investigated radial distribution function (RDF) and number of different types of H-bonds to characterize the complex H-bonding network for both the polymers. They confirmed the less hydrophilic character of PBI, therefore it has lower affinity towards PA compared to ABPBI. The effect of PA doping level and temperature in H-bonding for both the PBI and ABPBI systems were also reported in their paper. Zhu et al. discussed the H-bonding network within neat PBI and PA solvated PBI by investigating RDF plots between different proton donor and acceptor sites. [100] They studied the microscopic structure and hydrogen bonding characteristics of the pristine and PA doped *m*-PBI and *p*-PBI using MD simulations based on a united-atom force field model. They found that among the pristine PBIs, *p*-PBI is more ordered and stretched than the *m*-PBI. In our earlier report, [160, 175] we had studied PA solvated monomer (BI) of PBI system. We had discussed structural arrangement of BI, probability of stacking and the effect of the amount of PA on this arrangement. We had also revealed different types of H-bonding probability between BI and PA which is responsible for structural heterogeneity and a correlation between structural and dynamical heterogeneity in the PA doped BI system had been established. [176]

Till date, a comparative single chain structural property of PBI and ABPBI in PA solvent is unexplored. The computation of single chain conformational behavior will serve as the first step to understand physical properties of the polymers in PA as solvent, which are of direct interest. The microstructure of a single chain of polymer tells us about the physical arrangement of the monomer units along the backbone which in turn results the macroscopic properties of polymer such as durability, mechanical strength, solvent up-take capacities. In this work, we have performed classical MD simulations of PBI and ABPBI single chains solvated in PA as well as melt systems of both the polymers. We have investigated the structural properties of single polymer chain in melts and the effect of solvent on the chain conformations. The objective of this work is to provide correlations and differences between structural and conformational complexities of PBI and ABPBI in PA (and in melt) and its effect in properties as fuel cell membrane. The end-to-end distance and radius of gyration of ABPBI and PBI single chain, which gives us direct indication about the conformational behavior of the polymer chain, are calculated and analyzed. We studied how the conformational changes are reflected in their solvent uptake capacities. The arrangements of the solvent along the backbone of ABPBI and PBI chain have been compared and how it affects the rigidity of the chain

is being explored. The difference in hydrogen bonding arrangement along the ABPBI and PBI chain and its correlation with the proton conductivity values has been studied.

5.2 Computational Details

We have performed classical MD simulations on PBI and ABPBI polymer melts as well as PA solvated PBI and ABPBI single chains separately using all atomistic force field. The chemical structures of the monomer of PBI and ABPBI are shown in Figure 5.1.

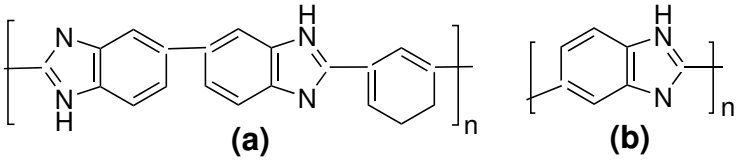

FIGURE 5.1: Chemical structure of (a) PBI and (b) ABPBI

We have constructed PBI chains consist of 8 monomer units and ABPBI chains consist of 24 monomer units to keep the initial chain length of both the polymers about the same. All the simulations were performed with GROMACS 4.0.7 package. [135, 136] The simulation cells of melt of PBI and ABPBI were constructed separately by adding 80 polymer chains each. Single chain of PBI (8 repeating units) and ABPBI (24 repeating units) were solvated with PA. These two solvated systems represent extremely dilute polymer solution. The total potential energy used to calculate forces among atoms were sum over all the bonded and non-bonded interactions. The bonded interaction energy consists of harmonic bond, angle potential, proper and improper dihedral potential. The non-bonded interactions energy consists of Lennard-Jones (LJ) potential and electrostatic interaction. All these potential energy forms are used as implemented in GROMACS 4.0.7 package. [135, 136] The parameters for bond and angle potentials for PBI and ABPBI were adapted from OPLS-AA force field. [119, 137] The parameters for dihedral potential for PBI and ABPBI were calculated from quantum chemical calculations. We optimized PBI and ABPBI made of three monomers using B3LYP functional with 6-311g (d, p) basis set by using the Gaussian 09 program. [138] With these optimized structures, dihedral scan optimization was performed with an increment of 18° (each dihedral angle separately) in each step. At each step the geometry of the molecule was optimized and the energy value was calculated as a function of dihedral angle, and fitted by the dihedral potential function of the form:

$$V_{rb} = \sum_{n=0}^{5} C_n (cos(\psi))^n \tag{5.1}$$

where, C_ns are (n= 0, 5) dihedral parameters, ψ is dihedral angle and V_{rb} is the corresponding dihedral potential energy. The calculated parameters, C_ns were incorporated in the force-field. In Figure 5.2(a) and 5.2(b), dihedral energies from *ab initio* quantum chemical calculation and fitting of the classical dihedral potential energy function have been shown for C_b-C_b-C_b-C_b and C_b-C_b-C_{im}-N_{im} dihedrals (C_b denotes carbone atom of benzene and C_{im} and N_{im} denote carbone and nitrogen atoms of imidazole) in case of PBI. C_b-C_b-C_{im}-N_{im} dihedrals for ABPBI are shown in Figure 5.2(c).

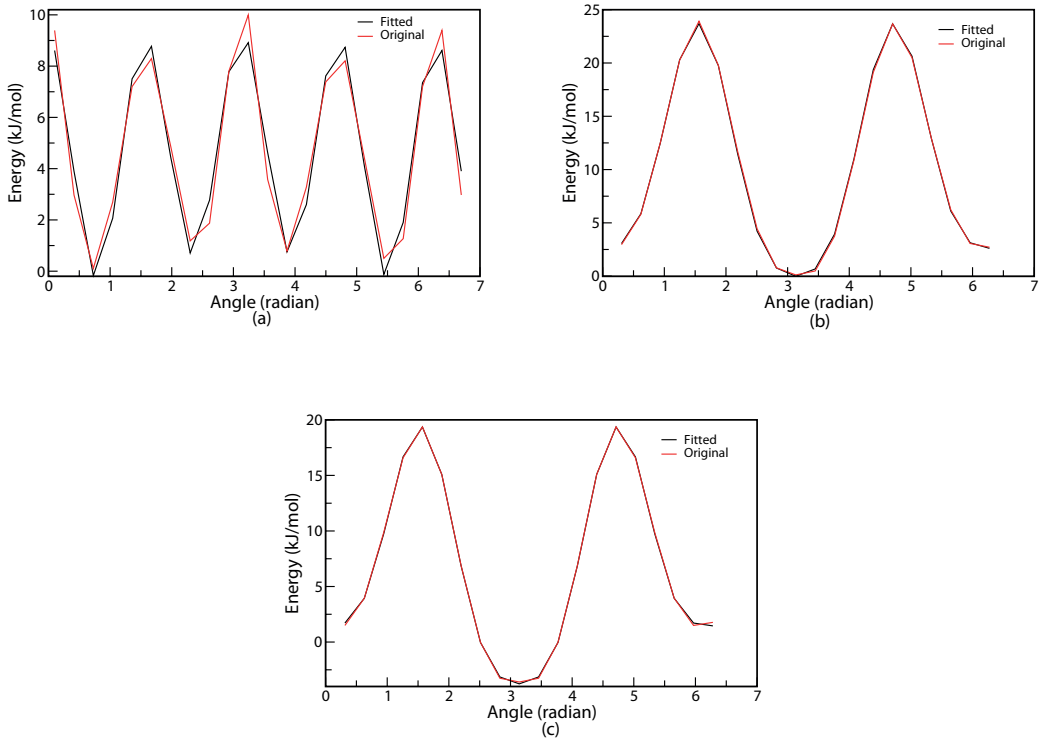

FIGURE 5.2: Fitting of dihedral potential energy of a) C_b-C_b-C_b-C_b b) C_b-C_b-C_{im}-N_{im} dihedral for PBI and c) C_b-C_b-C_{im}-N_{im} for ABPBI

Dihedral parameter values (C_ns) were shown in Table 5.1.

TABLE 5.1: Dihedral parameter values for PBI and ABPBI

Dihedral	C_0 kJ/mol	C_1 kJ/mol	C_2 kJ/mol	C_3 kJ/mol	C_4 kJ/mol	C_5 kJ/mol
C-C-C-N (PBI)	23.6855	1.5774	-40.0972	-1.2674	17.7090	0.9971
C-C-C-C (PBI)	9.1038	-0.1848	-35.7188	-1.8278	35.7281	1.8779
C-C-C-N (ABPBI)	19.3584	2.6036	-38.1289	-0.6441	17.6170	0.6493

The values of LJ parameters (σ and ϵ) for all the atoms were taken from OPLS-AA force field. [119, 137] The partial charges of the individual atoms for both PBI and ABPBI were calculated by quantum chemical calculation using CHELPG [139] method as implemented in Gaussian 09 code. [138] All bonded force field parameters including

parameters adopted from OPLS-AA for both the chains are listed in Table Table 5.2 and 5.3.

TABLE 5.2: Bonded force field parameters for PBI and ABPBI (bond parameters).

Bond description	$\mathbf{b_0}$ **(nm)**	$\mathbf{K_b}$ **(kJ/mol/nm^2)**
$C_{benzene}$-$C_{benzene}$	0.140	392459.2
$C_{benzene}$-$N_{attached\ with\ hydrogen}$	0.138	357313.6
$C_{benzene}$-$N_{without\ hydrogen}$	0.139	346435.2
$C_{benzene}$-$H_{benzene}$	0.108	307105.6
$N_{attched\ with\ hydrogen}$-H	0.101	363171.2
$C_{benzimidazole}$-$H_{terminal}$	0.108	307105.6
$C_{benzimidazole}$-$N_{attached\ with\ hydrogen}$	0.134	399153.6
$C_{benzimidazole}$-$N_{without\ hydrogen}$	0.133	408358.4

TABLE 5.3: Bonded force field parameters for PBI and ABPBI (angle parameters).

Angle description	$\boldsymbol{\theta_0}$ **(°)**	$\mathbf{K_\theta}$ **(kJ/mol/rad^2)**
$C_{benzene}$-$C_{benzene}$-$C_{benzene}$	120.00	527.184
$C_{benzene}$-$C_{benzene}$-$C_{benzimidazole}$	120.00	527.184
$C_{benzene}$-$C_{benzene}$-$N_{attached\ with\ hydrogen}$	108.70	585.760
$C_{benzene}$-$C_{benzene}$-$N_{without\ hydrogen}$	108.70	585.760
$C_{benzene}$-$N_{attached\ with\ hydrogen}$-$C_{benzimidazole}$	109.80	585.760
$C_{benzene}$-$N_{without\ hydrogen}$-$C_{benzimidazole}$	109.80	585.760
$N_{attached\ with\ hydrogen}$-$C_{benzimidazole}$-$N_{without\ hydrogen}$	120.00	585.760
$C_{benzene}$-$C_{benzene}$-$H_{benzene}$	120.00	292.880
$C_{benzene}$-$N_{attached\ with\ hydrogen}$-$H_{attached\ with\ nitrogen}$	118.00	292.880
$C_{benzimidazole}$-$N_{attached\ with\ hydrogen}$-$H_{attached\ with\ nitrogen}$	120.00	527.184
$N_{atached\ with\ hydrogen}$-$C_{benzimidazole}$-$H_{terminal}$	120.00	292.880
$N_{without\ hydrogen}$-$C_{benzimidazole}$-$H_{terminal}$	120.00	292.880

For PA, all the force field parameters were taken from the paper of Spieser et al. [161]

All the simulations were carried out in NPT ensemble with periodic boundary conditions in all directions. Temperature was maintained using Berendsen thermostat [131] with a coupling constant of 0.1 ps and Berendsen barostat for isotropic pressure control with coupling constant of 1ps was used to keep the pressure constant at 1 bar. Reaction field electrostatics [140, 141] was used with a cut-off length of 1.2 nm for pure melt systems. In case of PBI and ABPBI in PA as solvent, particle mesh Ewald (PME) method was used for electrostatic interaction. For PBI and ABPBI melt systems, 1 μs production runs were performed at a wide range of temperature starting from 500K up to 1000K. Simulated annealing (SA) for better sampling of the phase space on the energy-optimized structure was performed on the single chains of PBI and ABPBI. These well-equilibrated single chains were replicated to prepare a bulk system containing 80 chains in each simulation cell. These bulk systems were gradually heated from 500 K to 1000 K, by 50 K in each step, and NPT simulation of 500 ps was performed at each step. Similarly,

the systems were cooled in six steps from 1000 K to 500 K. This SA cycle of heating and cooling was repeated at least six times until the potential energy converges with respect to the previous cycle. From the last SA steps, we grabbed frames at different temperatures and subjected to NPT simulations for 800 ns at these temperatures to obtain the glass transition temperature. The melt systems were simulated at 750 K (above glass transition temperature) while the single chain in PA were simulated at 450 K for 1 μs. For all the systems, trajectories were recorded every 2 ps and last 10 ns of the production run were analyzed.

5.3 Force Field Validation

The validation of force field for both the polymers were done by comparing the density and glass transition temperature with experiment. The calculated density of bulk PBI at 300 K and 1 atm pressure from simulation is 1.23 $\pm$ 0.02 g/cm^3 where experimental density of PBI varies from 1.2-1.34 g/cm^3 depending on whether it is an untreated PBI fiber or annealed or plasticized PBI fiber. [177, 178] Therefore, density of simulated PBI well agrees with the experimental density. For ABPBI, the calculated density from simulation is 1.32 $\pm$ 0.03 g/cm^3 at 300 K whereas the reported experimental density is 1.4 g/cm^3. [179] Hence, densities of both the polymers (PBI and ABPBI) are in well agreement with the experimental data. For computing the glass transition temperature, we have calculated densities at different temperatures ranging from 500 K to 1000 K and plotted for PBI and ABPBI as a function of temperature in Figure 5.3.

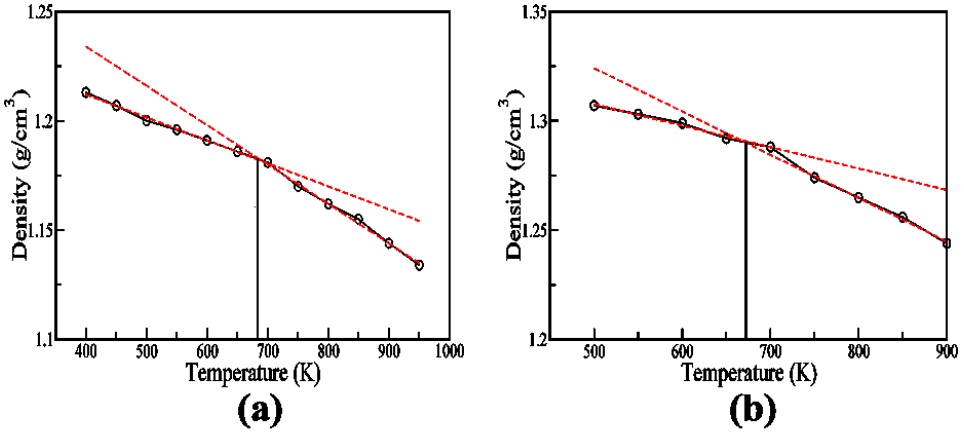

FIGURE 5.3: Density as a function of temperature for (a) PBI and (b) ABPBI

In case of PBI, there is a change of slope in density as a function of temperature plot below 680 K (5.3(a)) which indicates ~680 K is the glass transition temperature for PBI. The glass transition temperature for PBI is reported as 690 K - 700 K. [44] For ABPBI,

we obtained the glass transition temperature of 670 K (5.3(b)) while the experimental value is > 673 K. [164] Thus the comparable values of density and glass transition temperature validate the force field for ABPBI and PBI.

5.4 Results and discussion

5.4.1 Structural properties of polymer

The physical properties of polymer depends on the structural properties and conformation of a single polymer chain to a large extent. The physical arrangement of the monomers along the backbone of a polymer chain reveals the microstructure of the system. For example, we can have two polymers of same composition but different durability due to different structural arrangement of the polymer chains.

5.4.1.1 End-to-end distance and radius of gyration

The conformation and shape of a polymer chain is characterized by end-to-end distance (R_{ee}) and radius of gyration (R_g). From R_g, we can predict the shape and size of the polymer coil and from R_{ee}, we get the elongation of the polymer chain. Therefore, to understand the structure of polymer chains in melts as well as in PA solvent, we have calculated the R_{ee} and R_g of both ABPBI and PBI chain over last 10 ns of production run trajectory. Since the chain length of ABPBI and PBI are not same, we have normalized the R_{ee} and R_g data by taking into consideration the ratio of calculated R_{ee} or R_g and the R_{ee} or R_g of the chain in its fully stretched conformation (represented by R_{ee} / $R_{ee}^{stretched}$ or R_g / $R_g^{stretched}$). Further in this chapter, we have denoted these ratios as fractional R_{ee} and fractional R_g. We plotted the distribution of these ratios for both ABPBI and PBI melts as well as in PA solvated single chain systems in Figures 5.4(a) and 5.4(b) respectively. It is observed from Figures 5.4(a) and 5.4(b) that for the polymer melts (ABPBI and PBI), fractional R_{ee} as well as R_g fluctuates over a wide range of distances. The result indicates that different polymer chains find different conformational energy state, which makes the polymer melt systems mostly disordered. The fractional end-to-end distance distribution [Figure 5.4(a)] of PBI melt shows presence of some conformations (0.05 to 0.2) smaller than ABPBI melt. This indicated that the PBI chains are more flexible compared to ABPBI chain. However, in Figure 5.4(b) we find ∼0.36 is the most probable fractional R_g for PBI melt, and it varies between 0.22 to 0.45, which is higher than ABPBI melt where fractional R_g varies from 0.19 to 0.40 with a maximum at 0.28. The result denotes that ABPBI chains are more coiled

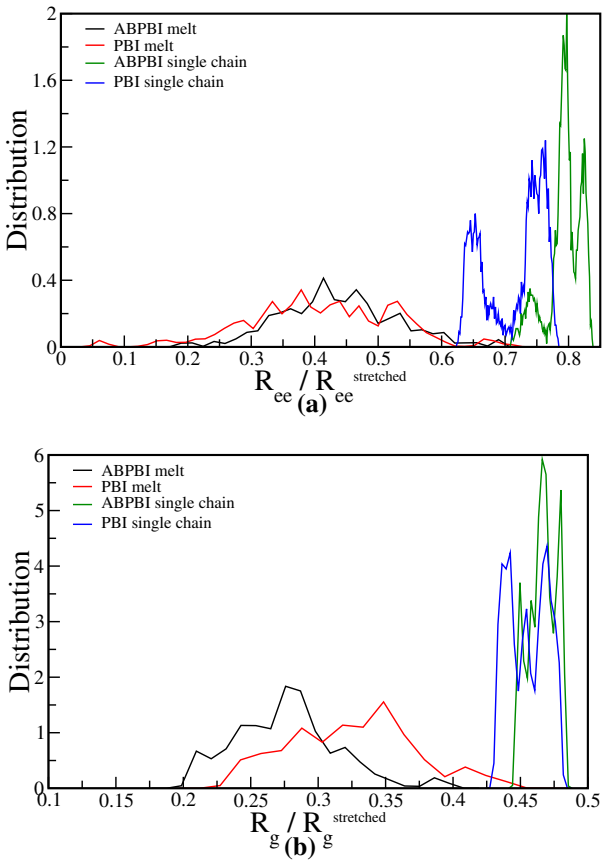

FIGURE 5.4: Distribution of (a) fractional end-to-end distance and (b) fractional radius of gyration for PBI and ABPBI in melt as well as in PA solvated systems.

than PBI chains in bulk. It is interesting to note that R_{ee} of PBI and ABPBI chains are almost same but R_g shows that ABPBI chains are more coiled.

Since PBI and ABPBI are membrane candidates for PEMFC in presence of PA, it is important to understand the conformation of single polymer chain in PA as solvent. The conformation of single polymer chain in solvent reflects the physical properties of the system e.g. miscibility, solvent uptake capacity of polymer. This is related to the efficiency of these polymers as a membrane material for high temperature fuel cell. To evaluate the quality (good or bad) of the solvent (PA) for ABPBI and PBI, we have investigated how the polymer conformation changes on moving from a melt system to PA solvated system. We observe in Figures 5.4(a) and 5.4(b) that both ABPBI and PBI chains become elongated in presence of PA compared to their corresponding melt systems, which indicates complete conformational change of these polymers in presence of PA. Since both the polymer chains become stretched in PA compared to the melt system, we can say that PA is a good solvent for both the polymers (ABPBI and PBI). It is evident from Figures 5.4(a) and 5.4(b) that ABPBI chain becomes more elongated compared to PBI chain in presence of PA which is in agreement with the experimental results. [49] The fractional R_{ee} of ABPBI chains varies from 0.71 to 0.84 where 0.79 is the

most probable fractional R_{ee} [Figure 5.4(a)]. Apart from 0.79, there is another significant peak at 0.82 in the fractional R_{ee} distribution plot which reflects that at some instant of times the chain becomes more elongated. There is also a relatively small peak at lower distance (0.74). In case of PBI, two distinct peaks are observed in Figure 5.4(a): one at lower distance (∼0.65) and other at higher distance (∼0.75), which reveals two distinct conformations of PA solvated PBI chains. Similarly, from the distribution of factional R_g in Figure 5.4(b), we can see R_g of ABPBI varies from 0.44 to 0.48 and for PBI from 0.42 to 0.48. Distribution of R_g also indicates that ABPBI and PBI chains prefer to stay in extended conformations. However, the conformations guiding the extended structure of these two polymers are different, which can be attributed to different curvature of the extended polymer chains. Therefore, ABPBI and PBI having same major constituent (benzimidazole), solvated with same solvent (PA) shows different conformations which can be indicator to their different physical properties like capability of dissolving acids, toughness or rigidity of the chain etc.

5.4.1.2 Characterization of curvature

The fractional R_{ee} and R_g distribution plot for the melt systems show that ABPBI chains are more coiled compared to PBI chains, while ABPBI chains in PA is more elongated compared to PBI in PA solution. To carry out further detailed analysis of the local structure of the polymer chains in melt and dilute solutions of PA, we have simplified the system by considering the center of mass (COM) of benzimidazole (BI) for ABPBI and COM of BI and COM of benzene for PBI. This is schematically represented in Figures 5.5(a) and 5.5(b) for ABPBI and PBI (taken from real time trajectory) respectively. Therefore, each monomer of ABPBI is represented by one COM particle and that of PBI is represented by three COM particles and both the polymer chains consist of 24 such COM particles.

Local arrangement

Bond distance distribution The structural properties of melt and PA solvated systems of ABPBI and PBI suggest that polymer chains have different conformations. Thus, for detail understanding of the nature and shape of these polymer chains in melt and in PA solvent, we have investigated the local arrangement of polymer chain segments for both the ABPBI and PBI. To understand whether the polymer chains are coiled or fully stretched, we have calculated the distance between every i^{th} COM particle and the $(i+1)^{th}$, $(i+2)th$, ..., and $(i+9)^{th}$ and their distributions are plotted in Figure 5.6, where i is the COM particle number. The COM particles along the polymer chain

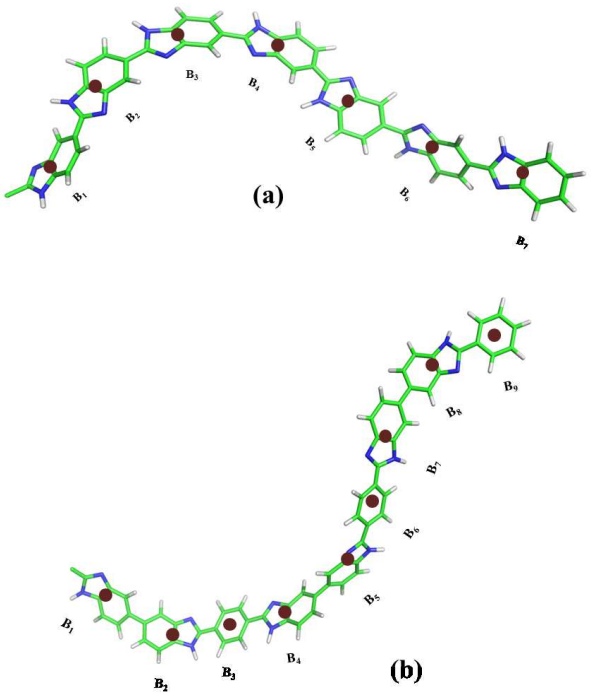

FIGURE 5.5: Snapshots of (a) ABPBI and (b) PBI along with centre of mass (COM) particles

are represented as B_1, B_2, B_3, ..., B_n respectively [see Figures 5.5(a) and 5.5(b)]. We refer these distributions as COM particles bond distance distribution in rest of our paper. For ABPBI and PBI melt systems, we plotted the COM particles bond distance distribution averaged over number of chains in Figures 5.6(a) and 5.6(b) respectively. We have here considered up to the 10th bead from both end of the chain for the clarity of visualization. If the polymer chain is completely extended, then the bond distance between B_i and B_{i+2} would be twice of B_i and B_{i+1}; B_i and B_{i+3} would be thrice that of B_i and B_{i+1} and so on. In the distance distribution plot [Figure 5.6(a)] for ABPBI melt system, we can see that though the bond distance of B_i - B_{i+2} (1.0 nm) is almost twice of B_i - B_{i+1} (0.5 nm) but B_i and B_{i+3} has slightly smaller bond distance than thrice of B_i - B_{i+1}. B_i - B_{i+4} also has smaller distance than four times B_i - B_{i+1}. These decreases in distances are much prominent for longer bonds (starting from B_i - B_{i+5} bonds). For longer bonds, bond lengths are fluctuating over a wide range of distances (from 0.9 nm to 4.6 nm), which indicates different polymer chain forms coil of different lengths which represent different structural conformations. In case of PBI (Figure 5.6(b)), B_i - B_{i+1}, B_i - B_{i+2}, B_i - B_{i+3} have peaks at 0.5, 1.0 and 1.5, respectively. It seems that these sets of COM beads are stretched. B_i - B_{i+4} has a maximum probable peak at $\sim$2.0 nm, while B_i - B_{i+5} has a high probable region from 2.3 to 2.5 nm. This indicates that these sets of beads are also almost stretched. The distribution of bonds is sharper for the PBI melt system compared to ABPBI, which indicates that

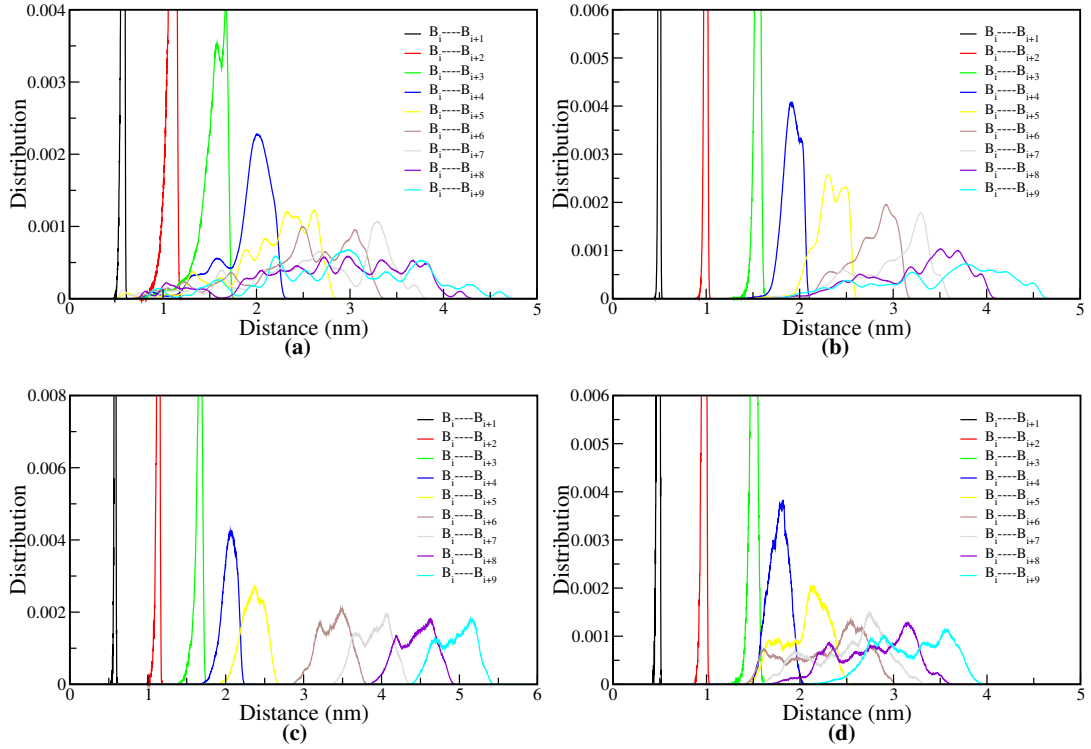

FIGURE 5.6: Bond distance distribution of COM particles for (a) ABPBI in melt (b) PBI in melt (c) PA solvated ABPBI and (d) PA solvated PBI chain

PBI chains are more stretched and less dynamic compared to ABPBI in melt system. This observation matches well with the fractional R_{ee} and R_g distribution (see Figures 5.4(a) and 5.4(b)), which shows ABPBI chains are more coiled. In case of PA solvated ABPBI and PBI single chain, we can observe discrete peaks at varying distances in the COM bond distance distribution (Figures 5.6(c) and 5.6(d)) plots. There are overlaps between peaks to some extent, which indicate curved nature of polymer chains. Now if we compare the distance distributions of PA solvated ABPBI and PBI chain (Figures 5.6(c) and 5.6(d)) with that of melt systems, we can notice that the extent of overlaps are more for the melt system. Therefore, it is clear that both ABPBI and PBI chain become stretched in presence of PA compared to the melt system. Figures 5.6(c) and 5.6(d) also shows that overlap in the bond distances is more for PA solvated PBI with respect to PA solvated ABPBI chain. In case of ABPBI chain, the bond distance of one COM particle overlaps only with the next neighboring COM particle whereas for PBI it can overlap with the bond distance of next five COM particles. Therefore, we can expect less curvature in case of PA solvated ABPBI chain compared to PBI chain which means PA solvated ABPBI chain is more elongated than that of PBI.

Angle distribution To evaluate the shape of the curvature forming along the chain, we have calculated the angles between COM particles which give us more direct estimation of curvature. We have computed the angle between B_i, B_{i+1}, B_{i+2}; B_{i+1}, B_{i+2}, B_{i+3}; B_{i+2}, B_{i+3}, B_{i+4} and so on (numbering are according to Figures 5.5(a) and 5.5(b)) and distribution is shown in Figure 5.7 for both ABPBI and PBI in melt as well as in PA solvated systems. The larger the angle, lesser will be the curvature and smaller value

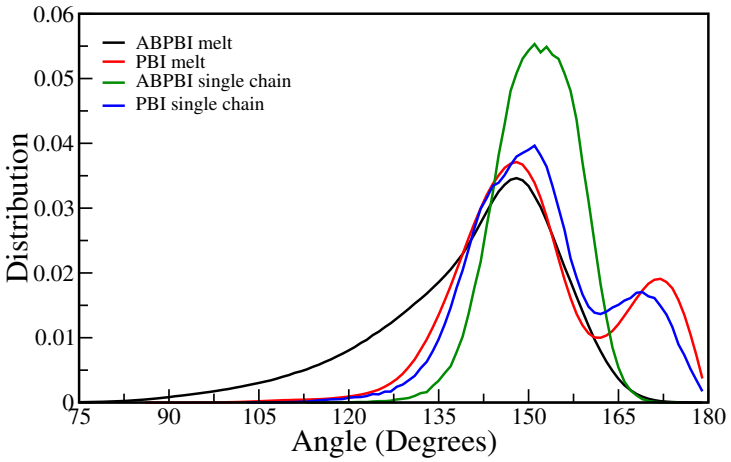

FIGURE 5.7: COM particles angle distribution for both PBI and ABPBI in melt as well as in PA solvated.

of angle represents sharp curvature, which in turn form coiled chain. We notice that in the melt systems, for both ABPBI and PBI chain, a sharp peak is observed at 150° but apart from that a peak at 170° is also observed in case of PBI. The two peaks in the angle distribution plot indicate two distinct conformations of PBI, which is in agreement with R_g (Figure 5.4(b)). We can see in Figure 5.7 that the angle between COM particles varies from 105 ° to 180° for PBI whereas for ABPBI, angle varies from 75° (much lower value) to 175°. The presence of smaller angles reflect the fact that ABPBI chain has sharp curvature compared to PBI chain in melt system. This result matches with the R_g (Figure 5.4(b)) and COM particle bond distance distribution results (Figures 5.6(a) and 5.6(b)). The comparative local microscopic arrangement of single polymer chain in melt with the solvated system shows (Figure 5.7) that the angle distribution peak for ABPBI single chain in PA solvated system is shifted to slightly higher angle value compared to melt system, which indicates that ABPBI chain becomes extended in presence of PA. Another interesting thing to observe is that in case of melt, the angle varies over a wide range (80° to 175°) whereas for PA solvated system angle varies only from 120° to 175°. This reveals the fact that ABPBI chain in presence of PA as solvent becomes less flexible compared to melt system. The rigidity of the PA solvated ABPBI chain, which acts as a membrane material in fuel cell, attributes to the mechanical strength of the membrane, which in turn determines the efficiency of the fuel cell. For PBI, in case of both melt and PA solvated system, two distinct peaks are observed in COM particle

angle distribution plot (Figure 5.7). Hence, there is no sign of conformational change as we go from melt to solvated system from this COM particle angle distribution plot. Thus PA has more effect on the conformation of ABPBI chain compared to PBI. This observation is also supported experimentally by Litt et al. [49]

Curvature along the chain To draw a clear picture of the shape of the curvature along the polymer chain, we have plotted time average angle distribution of COM particles as a function of angle number in Figure 5.8. The angles were computed along the chain: $\angle B_1B_2B_3$ were designated as 1, $\angle B_2B_3B_4$ as 2, $\angle B_3B_4B_5$ as 3, ..., and $\angle B_{22}B_{23}B_{24}$ as 22 (in Figure 5.8 X-axis). These angles were computed for every chain

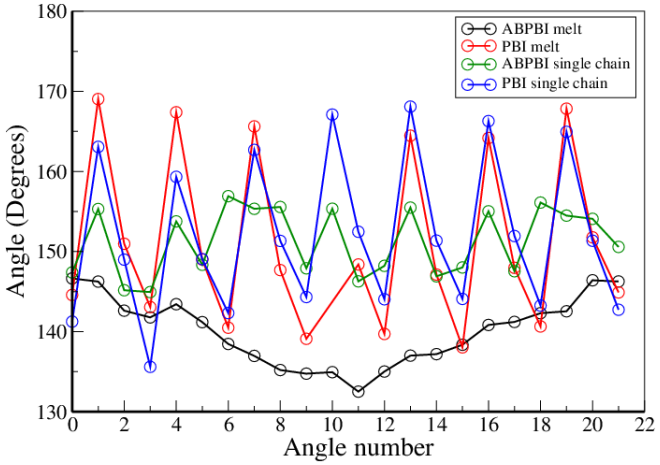

FIGURE 5.8: COM particles angle distribution as a function of angle number i.e. along the chain for both PBI and ABPBI.

in the melt systems. We have averaged over all such angles in the last 10 ns of the trajectory and represented in Figure 5.8. There are 24 COM particles in both ABPBI and PBI chains; hence there are 22 angles along the chain. In Figure 5.8, we notice a monotonic angle distribution curve for ABPBI chains in the melt system. The average angle gradually decreases towards the center of the polymer chain and again increases, although the deviation is small (from 130° to 145°). Therefore, ABPBI chains in melt have broad curvature in long range i.e., a single broad semi-circular loop type of structure is formed along the ABPBI chains. On the contrary, in case of PBI melt system the angle distribution is periodic. This shows us that several small curvatures are formed along the chain, the curvatures are wavy in nature and the direction of the curvature changes periodically. Since the angles vary only between 140° to 170°, the curvatures are not sharp. Therefore, the nature of the curvature is different in PBI and ABPBI chain in melt system. For PA solvated ABPBI (Figure 5.8), several curvatures, oriented periodically in alternate direction were observed. The angle varies from 145° to 157°, which indicates that the curvature is very broad. Due to this wavy nature, the ABPBI

chain in PA becomes elongated relative to the melt system. But the PBI chain in PA as well as in melt system shows the same nature of the curvature [see Figure 5.8]. The only difference is in the values of angles. The angles near the centre of the chain are significantly lower in case of melt system of PBI. Higher the angle, the sharpness of the curvature becomes less which in turn elongates the polymer chain. This provides us the evidence that PBI chain gets elongated in PA compared to melt system.

Dihedral angle distribution Dihedral angle represents angle between two planes and can give us the root cause of different curvatures in different systems. Therefore, dihedral angle between four given COM particles along the polymer chain gives an idea about the local curvature along the chain. If the dihedral angle between four COM particles is 0°, the distance between the end COMs is minimum and for 180°, the distance is maximum. Hence, we have calculated every possible dihedral angle along each single chain for ABPBI and PBI melt as well as for PA solvated single chain systems. We have plotted the distribution of these calculated dihedral angles and compared for each of the systems in Figure 5.9. In case of melt system, there is a significant difference between ABPBI and PBI in the dihedral distribution plot (Figure 5.9).

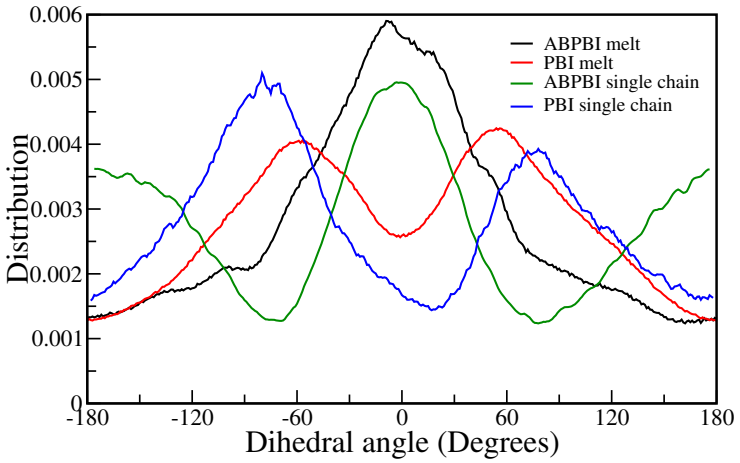

FIGURE 5.9: COM particles angle distribution for both PBI and ABPBI in melt as well as in PA solvated

For ABPBI melt, a peak is observed at 0° whereas a peak minimum is observed at this angle for PBI melt system. Two peaks of equal probability at +60° and -60° are observed for PBI melt, which is absent in ABPBI system. But at 180° and -180°, both the polymer melts show same dihedral distribution minima. Since peak at 0° represents the lowest distance, the distance between terminal COM particles among the four COM particles (within which the dihedral angle is calculated) become less for ABPBI (i.e., distance between second next neighbor COM particles). Peak at only 0° for ABPBI is also indicative of similarities in local curvature. But the difference in the overall end to end distance between ABPBI and PBI in melt systems is not much because of the

presence of peak at +60° and -60° for PBI systems. The two equally probable peaks for PBI chain at +60° and -60° indicates that the nature of the curvatures are same for PBI but the directions are different which reveals wavy curvature of the PBI chain. The result is in well agreement with the nature of the curvature analysis observed in Figure 5.8.

For PA solvated ABPBI, apart from peak at 0°, two peaks are observed at +180° and -180° (See Figure 5.9). The presence of peaks at 180° specify higher distances between the COM particles along the ABPBI chain in presence of PA. Therefore, ABPBI chain gets elongated in PA. In case of solvated PBI, the dihedral distribution plot is almost same as PBI melt. In both the cases two equally probable peaks are observed, the only difference is that in case of PA solvated single chain, dihedral angles shifted towards higher value. This result indicates larger distances between next neighbor COM particles. Therefore PA solvated PBI chain is relatively longer than polymer chains in melt.

Global arrangement From the analysis of local arrangement, we concluded that the curvature along PBI and ABPBI chains are different in the melt and PA solvent. Also, the shapes of the curvatures are different in PA solvated PBI and ABPBI. To get a clear picture of structure-property relationship, we have made a connection of these local variations in curvatures to the global structure of the polymer chains.

To evaluate the global arrangement of the chain segments along the polymer chain, we have calculated the angle between all the COM particle bond vectors with respect to the first COM particle bond vector. According to Figures 5.5(a) and 5.5(b), the angles were calculated between vectors $\overrightarrow{B_2B_1}$, $\overrightarrow{B_2B_3}$; $\overrightarrow{B_2B_1}$, $\overrightarrow{B_3B_4}$; $\overrightarrow{B_2B_1}$, $\overrightarrow{B_4B_5}$ and so on. We have computed the time average of these angles and plotted in Figure 5.10 for melts as well as solvated chains of ABPBI and PBI. The angle between first and second vectors is represented as 0, between first and third vectors as 1 and so on in Figure 5.10 (X-axis). In the melt, initially we observe angle decreases for ABPBI up to 4^{th} angle and for PBI up to 7^{th} angle and beyond that angle remain almost constant. Therefore both PBI and ABPBI chains in melt have broad curvatures over a large region and small sharp curvature locally.

Single chains of ABPBI and PBI in solvent are different from corresponding melt systems. From Figure 5.10, it is evident that ABPBI is not having global (long range) curvature but it is more wavy (local curvatures) than PBI in solvent. However, PBI shows some global curvature (similar to bulk) in PA. This clarifies why ABPBI chain is more extended compared to PBI in presence of PA, which is in well agreement with end-to-end-distance (Figure 5.4(a)), Rg (Figure 5.4(b)), bond distance distribution (Figure 5.6(c), 5.6(d)) data.

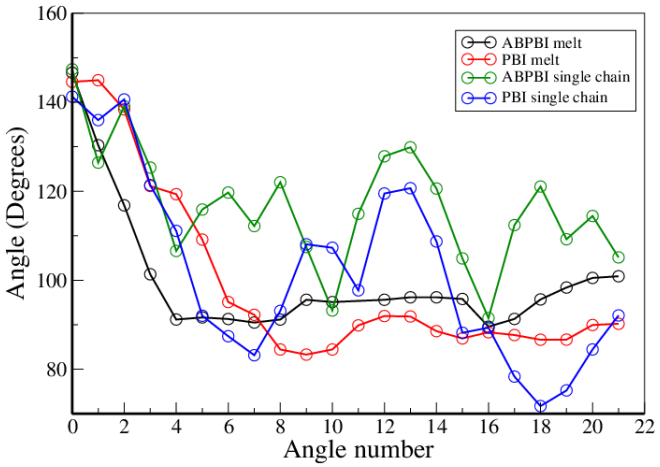

FIGURE 5.10: Distribution of angles between COM particles with respect to first bond vector for PBI and ABPBI in both melt and PA solvated systems.

5.4.1.3 Role of solvent

Arrangement of PA molecule along the chain The conformations of ABPBI and PBI chains in presence of PA are different though the polymers belong to same benzimidazole family. The only chemical difference between ABPBI and PBI is the presence of phenylene rings in the backbone of PBI. The reason behind the different conformations of ABPBI and PBI may also because of the interaction between the polymer backbone and solvent. Therefore, we have explored the interaction between PA molecules and polymer backbones. To understand the structural arrangement of the PA molecules around the polymer chain, we have considered the COM of each PA molecules and plotted RDF between these PA COMs and COM particles along the polymer chain as described in Figure 5.5. We have computed the RDF between the COM of benzene moiety for PBI, benzimidazole moiety for PBI and ABPBI chains and PA separately and plotted them in Figure 5.11. We observe that the RDF plots almost overlap with each other and the first solvation minima are also in the same position for the three RDFs. PA solvation shells surrounding benzimidazole for both ABPBI and PBI is same. But to our surprise it is also same around the benzene moiety where there is no basic site in phenylene ring with which PA can interact. Now to evaluate how many PA molecules are in the first solvation cell, we have calculated the coordination number for each RDF plots. The number of molecules in first solvation shell are also same in all the three cases. However, from the visual examination of the trajectory, we found that there are some PA molecules, which are shared by two or three consecutive COM particles of polymers. This means that the first solvation shell of consecutive COM particles overlap. In PBI, benzene ring is in between two benzimidazole rings and it shares the solvation shell of two benzimdazole moieties. This might be the reason why we have the number of PA molecules same in the first solvation shell of Benzene and benzimidazole.

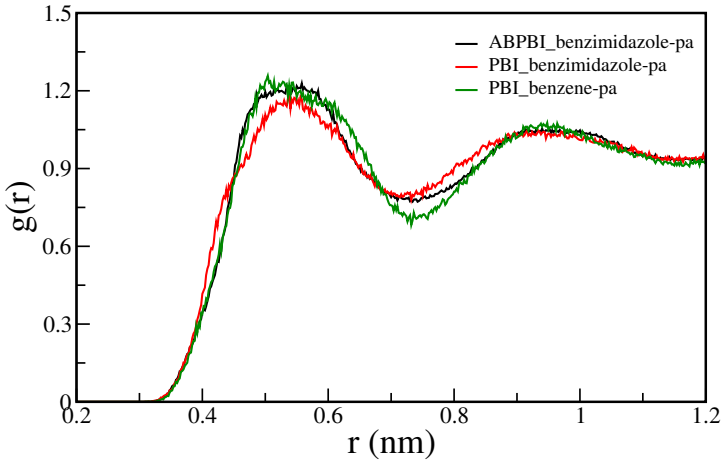

FIGURE 5.11: Radial distribution function (RDF) between COM of benzimidazole of PBI and PA; COM of benzimidazole of ABPBI and PA; COM of benzene of PBI and PAs.

From Figure 5.11, it is evident that the first solvation shell of benzimidazole/benzene is quite large (0.75 nm). At this large distance, the probability that the neighboring benzimidazole/benzene moieties are sharing PA molecules becomes high. This is obvious as there is no direct interaction between basic site of polymer and acidic site of PA, only cooperative arrangement of PA molecules at such larger distance. To explore the fact, we have counted the number of PA molecules within the first solvation shell as a function of distance from benzimidazole of ABPBI, benzimidazole of PBI and benzene of PBI, separately and plotted in Figure 5.12 (averaged over all the benzimidazole/benzene rings). Figure 5.12 depicts that at lower distances, the difference between the three

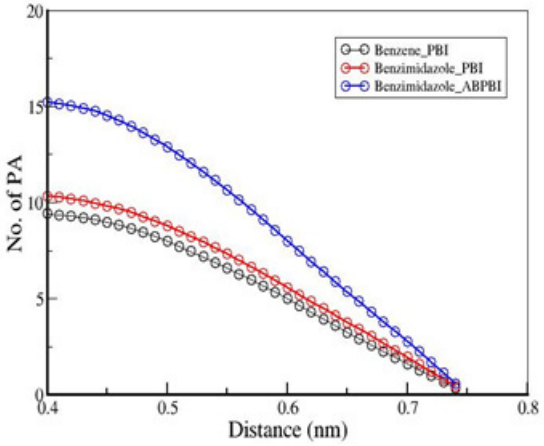

FIGURE 5.12: Number of PA molecules as a function of distance from COM particles of benzimidazole of PBI; benzimidazole of ABPBI; benzene of PBI.

plots are significant and as we go towards higher distances, number of PA molecules start decreasing. At lower distance, PA molecules come near to the benzimidazole ring because of the interaction between acidic and basic site of PA and polymer backbone, respectively.

Therefore, numbers of PA molecules present at lower distances are more because of the interaction with benzimidazole compared to benzene. At this lower distance there is a chance that two benzimidazole molecules can share PA molecules in case of ABPBI but it does not happen for PBI. For ABPBI, there is head-tail connection and for PBI head-head connection of benzimidazole moieties are present [see Figures 5.5(a) and 5.5(b)]. As a consequence imidazole moieties are far apart in case of PBI. Because of the larger separation of Imidazole moieties, they cannot interact with same PA molecules. This is the reason why we observe more PA molecules at 0.4 nm distance (Figure 5.12) for ABPBI (15) compared to PBI (10). But to our surprise, benzene in case of PBI is having 8 PA molecules at 0.4 nm distances although it does not have any interaction site. Since the length of benzene ring is smaller (less than 0.4 nm), the solvation shell at 0.4 nm from benzene COM overlaps with the two neighboring benzimidazole ring which makes the number of PA molecule as high as 8. The edge of the first solvation shell is at 0.75 nm (Figure 5.11) for all benzimidazole and benzene for both the polymers. The overlapping of large solvation shells play the key role here. However, at shorter distances we can observe that the density of PA around benzimidazole ring is more for ABPBI chain compared to PBI chain which is in well agreement with experimental data [56, 173] that shows for a given amount of PA, ABPBI absorbs more PA compared to PBI. Since proton conductivity through these membrane strongly depends on the amount of solvent (PA), therefore the result indicates PA doped ABPBI should exhibits better proton conductivity relative to PA doped PBI. Besides, larger PA density along the ABPBI chain makes it more elongated and less flexible compared to PBI.

We have explored the H-bond formation along the chain for detailed understanding of the structuring of PA molecules along the polymer chain. H-bonding between PA and monomers plays the key role in determining chain flexibility. We calculated the number of H-bonds formation between the backbone atoms of polymer chain and the PA molecules. There are two possibilities of H-bond formation: i) between nitrogen of polymer chain and hydrogen atoms of PA, ii) between amine hydrogen of polymer chain and oxygen atoms of PA. We have normalized the number of H-bonds by the number of imidazole moieties present in ABPBI and PBI and plotted them in Figure 5.13. Figure 5.13(a) represents the number of H-bonds per imidazole moieties as a function of time and its distribution is plotted in Figure 5.13(b). From Figure 5.13(a), it is evident that the number of H-bonds per benzimidazole ring is more for ABPBI than PBI. This is only possible if two consecutive benzimidazole rings share some PA molecules i.e. same PA molecule making two H-bonds with two adjacent imidazole moieties. Therefore, we calculated the possibilities of such H-bonds for both ABPBI and PBI. In PBI, there are no such H-bonds shared between neighboring benzimidazole moieties. On the contrary, in case of ABPBI there are some H-bonds shared between two neighboring benzimidazole

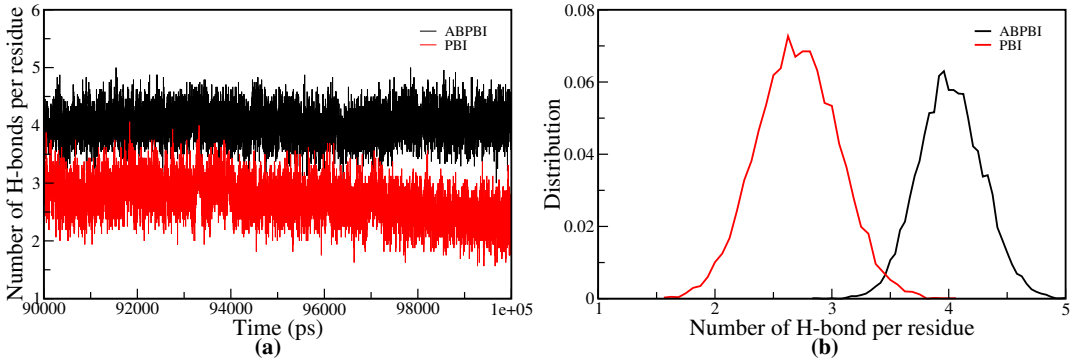

FIGURE 5.13: Number of hydrogen bonds formation and b) distribution of hydrogen bonds between backbone atoms of both PBI and ABPBI chain with PA per benzimidazole.

rings. We calculated the number of such H-bonds along the ABPBI chain and plotted the distribution of this number in Figure 5.14. It is evident that there are maximum six

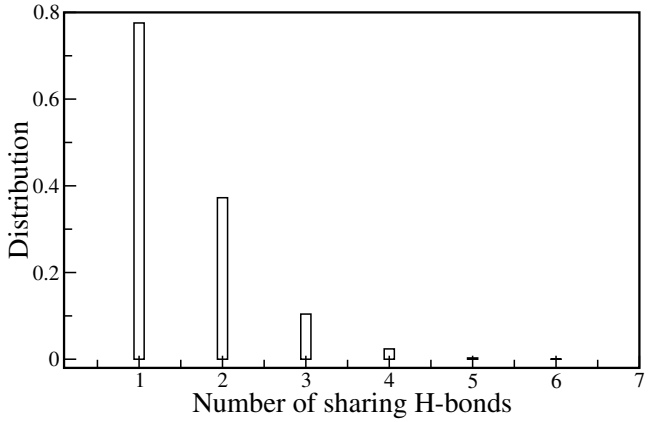

FIGURE 5.14: Distribution of sharing hydrogen bonds for ABPBI in PA solvated system.

such H-bonds can form along a single ABPBI chain but the probability is very less. We can see in Figure 5.14 that number of sharing-bonds varies from one to six. Presence of these sharing H-bonds in PA doped ABPBI makes the chain less flexible compared to PA doped PBI.

5.5 Conclusions

Detailed structural analysis of ABPBI and PBI single chain in melt as well as in PA were carried out using classical MD simulations. The end-to-end distance and radius of gyration shows both the chains get elongated in presence of PA compared to their corresponding melt system which proves that PA serves as a good solvent for both ABPBI and PBI. PA doped ABPBI chain is observed to become more stretched compared to

PA doped PBI system. The nature of the chain conformations are different for PA doped ABPBI and PBI which is revealed from local as well as global arrangement of chain segments. Curvature formation along the chain is also characterized. The role of the solvent on the chain backbone structuring is analyzed for PA doped ABPBI and PBI chain. The arrangements of PA molecules along the backbone confirm that ABPBI has more PA absorbing capacity than PBI. The H-bonding interaction between various atoms of polymer backbone and the atoms of PA molecules were computed along the polymer chain. The number of H-bonding is more in case of ABPBI chain compared to PBI chain. Some H-bonds are shared between neighboring benzimidazole moieties, which give extra stability and stiffness to ABPBI. The conformational properties of the single polymer chains obtained in this work provide insight to explain the experimental findings about proton conduction. All these understanding will equip us further to develop an efficient membrane for fuel cell.

Chapter 6

Proton transport mechanism of imidazole, triazole and phosphoric acid mixtures from *ab initio* molecular dynamics simulations

6.1 Introduction

For designing a new membrane for PEMFC with enhanced proton conductivity, a detailed understanding of the nature of proton transport through its components is necessary. In this context, the quantitative estimation of two types of proton transport mechanisms (Grotthuss and vehicular) would be useful which gives us an idea about the rate of proton transport in the membrane. Therefore, in this chapter, we have used AIMD to study the Grotthuss hopping of proton which is beyond the scope of classical MD. In the earlier chapters, we had investigated structural, dynamical and conformational properties of imidazole based systems. In the present chapter, we have explored the role of triazole in proton transport. We have carried out detail investigation on the PA-triazole mixture to know whether triazole can act as a better membrane material than imidazole.

Imidazole and imidazole based polymer in presence of acidic solvent were vastly studied [180–183] as a membrane material for fuel cell. The conductivity of liquid imidazole is as high as 10^{-3} $S\ cm^{-1}$ at 90 °C and imidazole based polymer in PA doped state is used as a potential membrane for fuel cell. [182] Addition of PBI to neat PA reduces its conductivity to a significant extent but increases the thermal as well as chemical

stability which makes the PA doped PBI an efficient membrane material. However, the electrochemical stability of imidazole group appears to be insufficient for fuel cell applications. [31] 1H-1,2,3 triazole has attracted recent research interest as an alternative heterocyclic compound to be used in PEMFC for its high electrochemical stability and better proton conductivity in PA doped state than imidazole. [184–186] 1H-1,2,3 triazole has a tautomer (2H-1,2,3 triazole) which can be formed by inter or intra-molecular proton transfer. [187] Besides, 1H-1,2,3 triazole is more acidic (pK_{a1}=1.17, pK_{a2}=9.26) than imidazole (pK_{a1}=7.18, pK_{a2}=14.52) [188] which influences proton conductivity of triazole based solid polyelectrolyte membrane. A study by Zhou et al. revealed considerable increase in conductivity in case of vinyl based polymer when the heterocyclic group imidazole was replaced by triazole. [189] 1H-1,2,3 triazole has been tethered to a number of polymeric backbones such as polyacrylate, [190] polyphosphazene, polysiloxane [191] to increase the mobility where proton conductivity strongly depends on the mobility and the density of charge carrier. Introduction of N-phenyl 1,2,4 triazole group in PBI was found to help in overcoming the limited solubility of the polymer and improve thermal stability, water absorption, oxidation resistance of the acid doped PBI. [192] The polymer membrane based on acid doped triazole functional group shows high conductivity even at lower PA doping ratio. But, the poor mechanical strength of triazole functionalized membrane limits its usage as a PEM for fuel cell. [193, 194] Therefore, several groups are trying to synthesize a membrane where triazole is used as a dopant to acidic polymers. [185, 195, 196] Hazarika et al. [194] synthesized blend of polyvinyl triazole (PVT) and PBI where they observed that proton conductivity of the blend is higher than neat PBI and it increases as the concentration of PVT increases. Potrekar et al. [192] prepared PBI tethered with N-phenyl 1,2,4 triazole group by high temperature solution polymerization in polyphosphoric acid (PPA). The membrane exhibits high thermal stability, good mechanical strength and good proton conductivity.

For designing a new membrane for PEMFC with enhanced proton conductivity, a detailed understanding of the nature of proton transport through its components is necessary. Extensive research work have been performed using different theoretical approaches to understand the proton conduction mechanism and its relation to structural arrangement of system constituents. Mane et al. investigated the potential of N-cage-H_2 along with i) PA ii) imidazole and iii) triazole molecules by using density functional theory (DFT) and Møller−Plesset (MP2) calculations. They suggested that 1,2,3 triazole is the most feasible molecule among the three, acting as an effective counterpart of N-cage-H_2 for proton transfer. [186] Shuo et al. determined energy barrier for different proton transport pathways within PA doped PBI. Zhu et al. investigated the H-bonding network within neat and PA solvated PBI by examining radial distribution (RDF) plots between different proton donor and acceptor sites. [189] In our earlier study, we reported

the structural insight of PA doped Benzimidazole (BI) at different solvation level and its relationship with the mobility of PA by performing all atomistic Molecular Dynamics (MD) simulations with classical force fields. [160, 175] We also established a direct correlation between structural and dynamical heterogeneity of BI as well as PA. [176] But classical force field based MD fails to deal with the bond breaking and forming phenomenon. Therefore, it prevented us from quantifying Grotthuss like proton transport mechanism. In this respect, first-principle MD is the most reliable one to understand proton transport mechanism within H-bonding network. There are very few first principle MD studies on PA doped high temperature membrane materials till date. [101, 102] Vilčiauskas et al. [101] studied microscopic mechanism accountable for high proton conductivity in liquid PA using *ab intio* MD. The study revealed that interplay between long polarizable H-bonded chain and frustrated H-bonding network is responsible for high proton conductivity in liquid PA. They also simulated PA doped imidazole system [101] and compared it with liquid PA systems to understand the proton transport mechanism in more realistic system. Authors addressed local structure, dynamics, energetics in their work and established a relation of these properties to long range proton transport.

The objective of this work is to investigate the potential of triazole (TRZ) as a replacement to imidazole (IMD) and also the possibility of using PA-IMD-TRZ ternary system in place of PA-IMD system from first-principle MD. In this study, we have performed Car-Parrinnelo MD (CPMD) on PA melt, PA solvated imidazole (PA-IMD), PA solvated triazole (PA-TRZ) and PA solvated equi-mixture of both imidazole and triazole (PA-IMD-TRZ) systems. Our aim is to provide fundamental atomistic level understanding of proton transfer in these mixtures. We intend to address complex dynamics of protons which follow the vehicular motion of system constituents and also hop along the H-bonded network (Grotthuss mechanism). We investigated the structural arrangement of system constituents, various types of possible H-bonding arrangements and proton transfer probability. We also estimated the contribution of Grotthuss as well as vehicular mechanism of proton transport for these systems. In Grotthuss mechanism, two types of proton transports (shuttling and hopping) were observed for all the systems. Contribution of these proton transfers are different in different systems which creates the difference in rate of proton transports and in turn proton conductivity. To the best of our knowledge, this is the first account where proton transport mechanism in PA doped triazole is being explored and how the presence of TRZ in PA doped IMD system influence the proton dynamics has been investigated. The comparative proton dynamics in these systems will help in designing new membrane material with improved proton conductivity.

6.2 Computational Details

We performed first principle MD simulation on PA melt, PA-IMD, PA-TRZ and PA-IMD-TRZ systems. We used CPMD code [197] for all the simulations. The simulation box of PA melt system consists of 50 PA molecules. In case of both PA-IMD and PA-TRZ systems, 32 PA molecules were mixed with 16 IMD/16 TRZ molecules to make the IMD/TRZ to PA ratio 1:2. PA-IMD-TRZ system comprised of 8 molecules each of IMD and TRZ and 32 PA molecules. In order to obtain well equilibrated initial structure for CPMD run, we carried out classical MD simulation on randomly placed molecules in a simulation box for 100 ns using Gromacs-4.6.3. [198, 199] The final structure of classical MD was used to perform equilibriation CPMD run for 12 ps in canonical ensemble (NVT) using Noose-Hoover thermostat at 400K. After the equilibration run, the system was set for production run in microcanonical ensemble (NVE) for 60 ps. The snapshots of each of the equilibrated system (i.e., PA-melt, PA-IMD, PA-TRZ, PA-IMD-TRZ) are given in Figure 6.1. Electronic structure calculation was performed using Kohn-

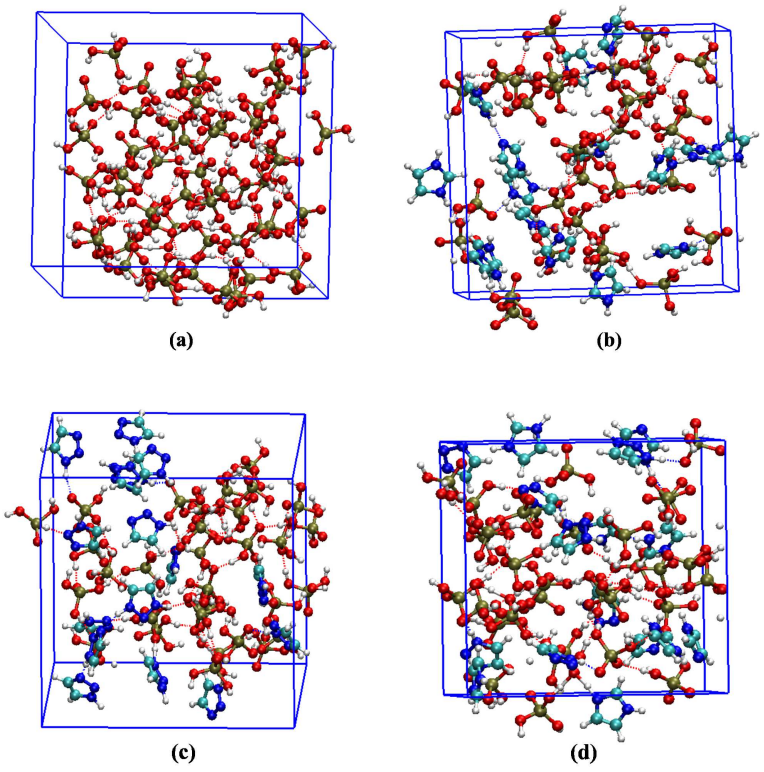

FIGURE 6.1: Snapshots of equilibrated structure for (a) PA melt, (b) PA + IMD, (c) PA + TRZ and (d) PA + IMD + TRZ systems.

Sham (KS) formulation within plane wave basis. We used BLYP functional which was already proven to be a good descriptor of structural and dynamical properties for PA and IMD. [101, 102] The plane-wave expansion of the KS orbitals was truncated at a kinetic

energy of 85 Ry. Core electrons were treated using semi-local norm-conserving Martins-Troullier pseudopotentials. The equation of motion was solved using Verlet algorithm with timestep of 5 a.u and with a fictitious electron mass of 500 a.u. Following atomic masses for the nuclei were used: 2 amu for Hydrogen, 12 amu for Carbon, 14 amu for Nitrogen, 16 amu for Oxygen and 31 amu for Phosphorus. The simulation details implemented in this study is adapted from the work of Vilčiauskas et al. for PA melt system. [101]

6.3 Results and Discussion

There are several possibilities of H-bonding complex formation due to the dissociation of IMD, TRZ and PA molecules in these mixtures of PA-IMD, PA-TRZ and PA-IMD-TRZ. The formation and dissociation of such types of H-bonding complexes play a vital role in short and long range proton transport. Hence, understanding the time evolution of the arrangements of various atoms/molecules in the system is essential to deal with the proton transport phenomenon. Since, proton is transported mostly through the H-bonds created by the dissociation of PA [93] in the membrane, we have studied structural arrangement of PA atoms in all the systems. To understand the effect of IMD and TRZ both separately as well as together on the arrangement of PA, we have plotted RDF between different atoms of PA in three systems (PA-IMD, PA-TRZ and PA-IMD-TRZ) and compared with that in PA melt system. We plotted RDFs between Phosphorous-Phosphorous (P-P), Oxygen-Oxygen (O-O) and Hydrogen-Hydrogen (H-H) atoms depicted in Figures 6.2(a), 6.2(b), and 6.2(c) respectively. We can observe in Figure 6.2(a) that the peak positions are shifted to lower value for PA-IMD, PA-TRZ and PA-IMD-TRZ systems compared to PA melt. This indicates that PA molecules come near to each other in presence of IMD and TRZ molecules in the system. The peak heights in these systems reflect the structuring of P atoms which also increases in the presence of IMD or TRZ. Figures 6.2(b) and 6.2(c) show that the nature of the RDF plots for O and H atoms are same for all the systems. However, the peak heights are in the same order as in the RDFs of P atoms [Figure 6.2(a)]. Therefore, considering the probability of various atoms of PA molecules arranging among themselves, PA-IMD-TRZ system is more similar to PA melt compared to PA-IMD and PA-TRZ systems. Since PA melt system serves as a benchmark for proton transport, structural arrangement-wise PA-IMD-TRZ system is expected to be a better candidate among all the three systems (under study) for using as a proton conducting system.

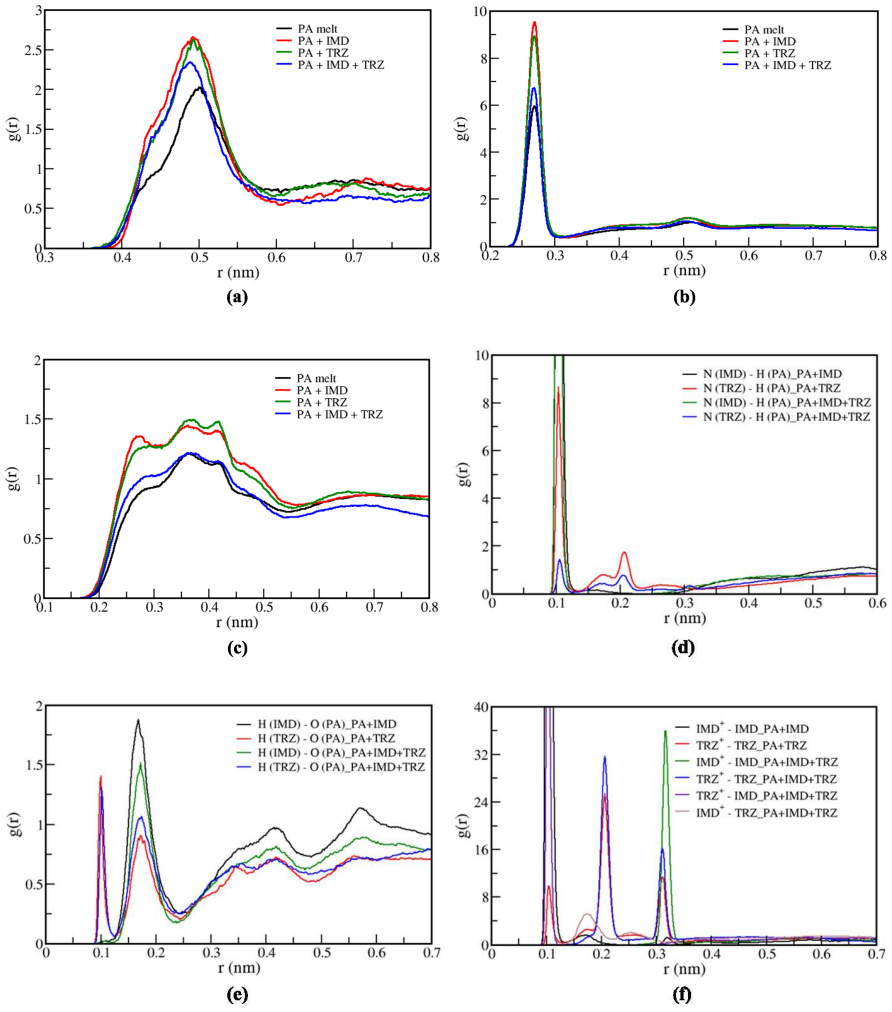

FIGURE 6.2: RDF of (a) P-P, (b) O-O and (c) H-H atoms of PA molecules RDF between (d) imine N of IMD/TRZ and H of PA, (e) O of PA and amine H of IMD/TRZ and (f) amine H of IMD/TRZ and imine N of IMD/TRZ.

In a good proton conducting system, proton is transported readily through the system constituents via transient H-bonds (H-bonds) formed between them. Hence, the constituent compounds should have the ability to take as well as give back protons easily. Therefore, to investigate the nature of the H-bond formation and to get an idea about the possibility of complete proton transfer from one atom to another, we have plotted RDFs between various proton donor and acceptor sites in these systems. There are two types of H-bonding interactions in between PA and IMD or TRZ: 1) PA can transfer proton to imine N of IMD/TRZ, and 2) amine H of IMD/TRZ can be transferred to O atom of PA. The RDFs between imine N and H of PA; amine H of IMD/TRZ, and O of PA are plotted in Figures 6.2(d), and 6.2(e) respectively. The peaks at 0.1 nm (N-H covalent bonding distance) in Figure 6.2(d) reveal the probability of complete proton transfer from PA to Imine N of IMD or TRZ in all the three systems. However, the peak heights indicate that probability of this type of proton transfer is much higher in case of

IMD than TRZ. Besides, for TRZ, the probability of complete proton transfer is much lesser in PA-IMD-TRZ system compared to PA-TRZ system. From the visualization of the trajectory, it has been found that proton is transported readily in the optimizaion step from PA to IMD which was also reported in the earlier study by Vilčiauskas et al. [102] In this work, most of the IMD molecules (13 out of 16 in PA-IMD system, 6 out of 8 in PA-IMD-TRZ system) were observed to get protonated in the optimization step whereas fewer TRZ molecules get protonated (6 out of 16 in PA-TRZ system and 2 out of 8 in PA-IMD-TRZ system). From Figure 6.2(d), we can infer that IMD is better proton acceptor compared to TRZ which attributes to its high proton affinity (-240.031 Kcal/mol) as referred by Mautner et al. [200] But, we can observe in Figure 6.2(e) that amine H of IMD does not get transferred to O atoms of PA whereas that of TRZ gets transferred to PA in both PA-TRZ as well as PA-IMD-TRZ systems. Therefore, Figure 6.2(e) indicates that there is a possibility of back transfer of proton from TRZ to PA but not from IMD. However, proton can also be transferred from IMD^+ to IMD; IMD^+ to TRZ; TRZ^+ to TRZ, and TRZ^+ to IMD. Therefore, we have plotted RDF between amine Hs and imine Ns of IMD/TRZ for all the three systems in Figure 6.2(f). We can observe in Figure 6.2(f) that two highly probable proton transfers can occur: i) from IMD^+ to IMD in PA-IMD system, and ii) from TRZ^+ to IMD in PA-IMD-TRZ system. However, there are less probabilities of proton transfer from TRZ^+ to TRZ. There is no proton transfer from IMD^+ to IMD; TRZ^+ to TRZ in PA-IMD-TRZ system. This is possibly due to the presence of less number of IMD and TRZ molecules (8 each) in the system.

We have checked further whether these proton transfers are complete transfer from donor to acceptor (hopping) or 'back and forth' motion of protons (shuttling) between donors and acceptors. In this study, for PA-IMD system, we can observe that one of the imidazole molecule takes proton from a imidazolium cation via forming imidazole-H-imidaole complex. Initially it was shuttling and then (at 45 ps), it gets completely transferred from one imidazole (IMD1) to another imidazole molecules (IMD2). We have plotted the distance of this particular proton from the two Ns of IMD1 and IMD2 in Figure 6.3(a). It is clear from the Figure that the proton was initially bonded to N of IMD1, it was going back and forth (shuttling) in between IMD1 and IMD2 for some time and then completely transferred to N of IMD2. The complex formation and back and forth proton transfer between two imidazole units was observed by Vilčiauskas et al. [102] Additionally we observed complete proton transfer from one IMD to another because of our long time trajectory, which can eventually attributes to the long range proton transport. On the other hand, in PA-TRZ and PA-IMD-TRZ systems, apart from PA to TRZ, proton transfer from TRZ^+ to PA has been observed. Figure 6.3(b) shows the distance of the proton from N (donor) of TRZ and from O (acceptor) of PA as

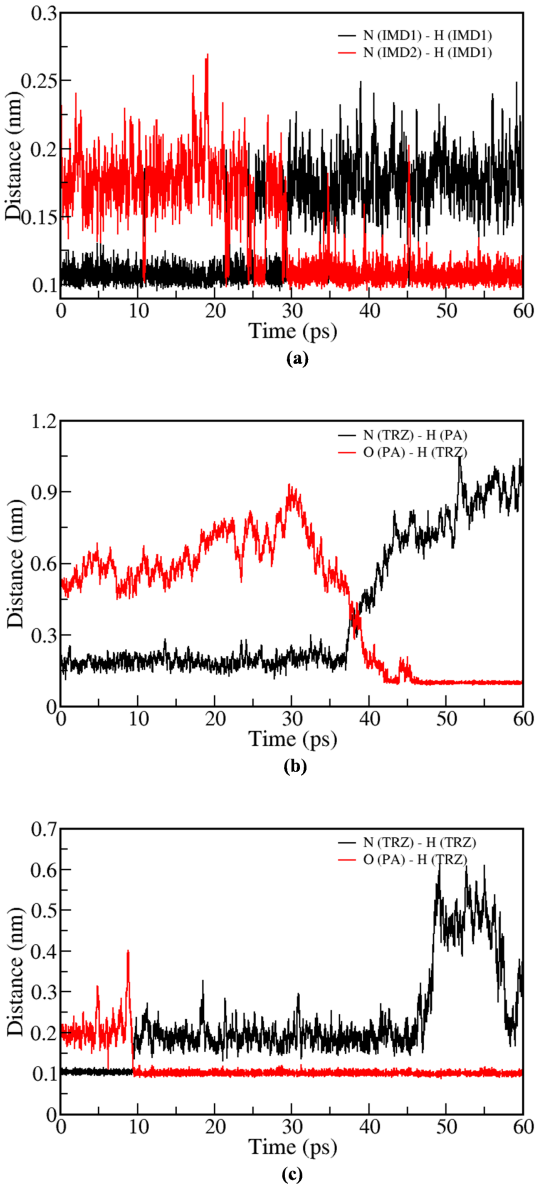

FIGURE 6.3: Distance of a given proton from a) two imidazole molecules in PA-IMD system b) imine N of TRZ and O atom of PA in PA-TRZ system c) imine N of TRZ and O atom of PA in PA-IMD-TRZ system.

a function of time for PA-TRZ system. In this case, proton has traveled larger distance from its initial position. This type of proton transfer also directly contributes towards long range proton transport. Similarly, Figure 6.3(c) shows proton transfer from TRZ to PA in case of PA-IMD-TRZ system. The movie of this particular proton transfer shows intermolecular tautomerization is taking place. One of the proton from PA transferrers to N2 of TRZ, electron density gets shifted to N1 and it takes proton from PA. This kind of proton transfer can induce several other proton transfers in the surrounding. Therefore, it can assist in long range proton transport. Hence, the study indicates that TRZ has higher contribution towards long range proton transport compared to IMD.

Since our motivation is to find proton conduction in these mixtures, we analyzed dynamical properties of the system constituents. We calculated self-diffusion coefficient of PA, IMD and TRZ for all the four systems and compared them to understand the role of these constituent molecules in proton transport. We plotted mean square displacement (MSD) and from the slope of the linear part of MSD, calculated diffusion coefficients by using Einstein's equation. The diffusion coefficient of protons (H^+) of only PA molecules which get transported through vehicular as well as Grotthuss mechanism are listed in Table 6.1 for all four systems. Diffusion coefficients of H^+ in PA

TABLE 6.1: Diffusion coefficients (10^{-6} cm^2/s) of H^+, P and ratio (H^+ / P) for PA melt, PA-IMD, PA-TRZ and PA-IMD-TRZ systems.

Element	PA melt	PA-IMD	PA-TRZ	PA-IMD-TRZ
H^+	4.14	4.02	4.07	3.21
P	0.87	1.80	1.34	0.96
raio(H^+ / P)	4.76	2.23	3.03	3.34

phase for PA melt and PA-IMD system are in good agreement with the value reported by Vilčiauskas et al. [102] We can see from Table 6.1 that the diffusion coefficient of H^+ of PA are almost same in PA melt, PA-IMD and PA-TRZ systems. But it is lower in case of PA-IMD-TRZ system. We have also calculated the diffusion coefficient values of P which represent only vehicular motion in the system are given in Table 6.1. The larger diffusion coefficient values of P reveal that in case of PA-IMD system, vehicular motion plays the vital role. From Table 6.1, it is also evident that in case of PA-TRZ system, vehicular motion also has significant contribution. On the other hand, the smaller values of diffusion coefficients for P in PA melt and PA-IMD-TRZ systems indicate substantial amount of Grotthuss like proton diffusion. To quantify the role of structural diffusion, we have taken the ratio of diffusion coefficients of H^+ and P for all the four systems and reported in Table 6.1. Structural diffusion is maximum in case of PA melt which is obvious. Comparing all the systems, structural diffusion in PA phase are in the order of: PA melt > PA-IMD-TRZ > PA-TRZ > PA-IMD. In PA-IMD-TRZ system, structural protons diffusion in PA phase is higher possibly due to the arrangement of various atoms of PA, which are similar to that of PA melt system [Figures 6.2(a), 6.2(b), and 6.2(c)]. Now to understand the contribution of IMD and TRZ in proton transport, we calculated diffusion coefficients of center of mass (COM) of IMD and TRZ. Diffusion coefficient of IMD in PA-IMD system is 1.8×10^{-6} cm^2/s whereas TRZ in PA-TRZ system is 1.1×10^{-6} cm^2/s, which is lower than IMD. But in PA-IMD-TRZ system, COM diffusion of both IMD and TRZ decreases to 1.3×10^{-6} cm^2/s and 0.67×10^{-6} cm^2/s respectively. These COM diffusions are the contribution of IMD and TRZ to vehicular mechanism of proton transport. To quantitatively estimate the contribution of overall systems toward vehicular and Grotthuss mechanism of proton transfer, we have calculated total diffusion

coefficients (from total MSD) of P of PA and COM of IMD/TRZ which represent vehicular motion; and H^+ of PA and IMD/TRZ which represent both vehicular and structural diffusion. The ratio of these two diffusion coefficients will help us in estimating the contribution from structural diffusion. All the values are listed in Table 6.2. Contribution

TABLE 6.2: Diffusion coefficients (10^{-6} cm^2/s) of COM of IMD/TRZ + P, H^+ of IMD/TRZ and PA and ratio of these two.

Element	PA-IMD	PA-TRZ	PA-IMD-TRZ
H^+	4.21	4.93	2.7
COM of IMD/TRZ + P	1.80	1.17	0.91
ratio (H^+ / P)	2.34	4.21	2.97

of the three systems (except PA-melt) towards structural diffusion are in the order of PA-TRZ > PA-IMD-TRZ > PA-IMD. But in case of PA-IMD-TRZ system, diffusion coefficients of system constituents (both vehicular and Grotthuss) are slower than other systems. However, the ratio indicates that structural diffusion plays the major role in PA-IMD-TRZ system. Structural diffusion increases in PA-TRZ system by 44% and by 21% in PA-IMD-TRZ system compared to PA-IMD system. Therefore, we can expect that mixing TRZ in PA or in PA-IMD will make the system more efficient for proton conduction. IMD and TRZ are observed to contribute to the proton transport in two ways: i) long range translational motion and ii) intermolecular proton transfer between adjacent molecules. In IMD or TRZ based polymer systems, long range translative motion becomes no longer possible due to immobilization of these molecules. Therefore, intermolecular proton transfer i.e. structural diffusion will only contribute to the proton conduction. The results indicate that the presence of both IMD and TRZ reduces the vehicular motion but the structural diffusion plays the vital role.

To understand the origin of slow structural proton diffusion in PA-IMD system, we investigated the nature of the structural proton transfer. There are two types of structural proton transfer that can occur in these systems as described in the report by Choe et al. for water [63]; i) constructive and ii) non-constructive. The schematic for constructive and non-constructive proton transport in PA phase are shown in Figure 6.4. In non-constructive proton transport, proton moves from one PA molecule to the next neighbouring PA molecule temporarily and after some time it comes back to the first PA molecule. In constructive proton transport, proton hops from one PA molecule to the next available PA molecule permanently and from the second to the third neighbouring PA molecule and so on. As an evidence, we analyzed the trajectory to find O atoms of PA molecules connected to the proton, which shuttles and hops as a function of simulation time. We plotted indices of these PA molecules chosen for three random protons for PA-IMD, PA-TRZ and PA-IMD-TRZ systems separately in Figures 6.5(a), 6.5(b), and 6.5(c). It is evident from these Figures that the protons were initially connected

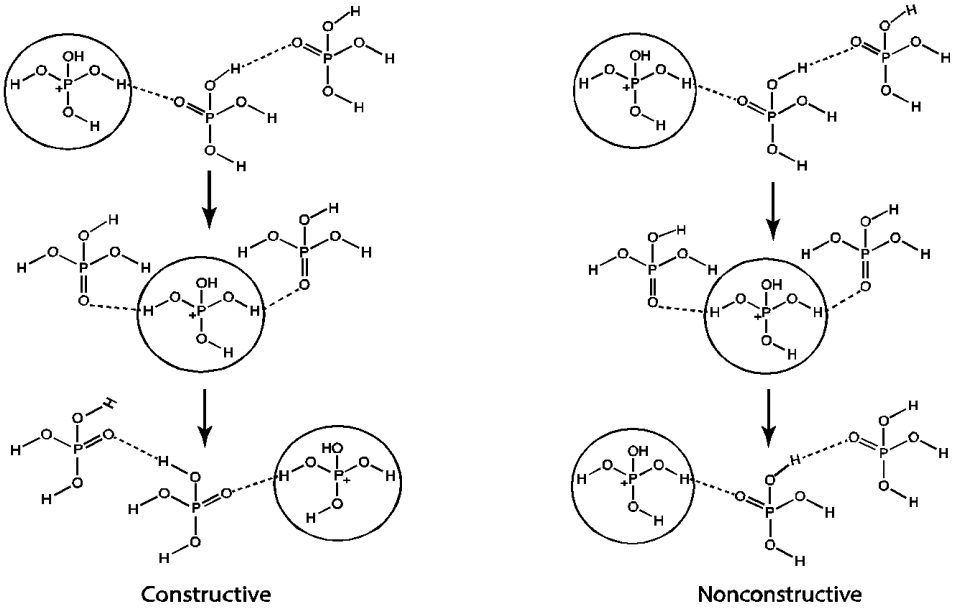

FIGURE 6.4: Schematic of constructive and nonconstructive proton transport.

with one O atom of a PA molecule and shuttle between other O atoms of different PA molecules. However, from Figures 6.5(d), 6.5(e), and 6.5(f), we can observe constructive motion in the same three systems where proton is shuttling between O atoms and finally get hopped to different PAs. This kind of structural diffusion contributes to the long range proton transport.

To quantitatively estimate the contribution of these two types of proton transfers in the four systems under study, we have calculated number of hopping of all the protons of PA, IMD and TRZ during 60 ps of simulation. In Table 6.3, we have listed numbers of hopping in PA melt, PA-IMD, PA-TRZ and PA-IMD-TRZ systems, which shows that the number of hopping is maximum in PA melt followed by PA-TRZ system.

TABLE 6.3: Number of hopping in PA melt, PA-IMD, PA-TRZ and PA-IMD-TRZ systems.

PA melt	PA-IMD	PA-TRZ	PA-IMD-TRZ
210	112	186	141

In PA-IMD system number of hopping is the least. Therefore, shuttling plays a major role in PA-IMD system which contributes only to the short range proton dynamics. Addition of TRZ increases the long range proton transport compared to PA-IMD system.

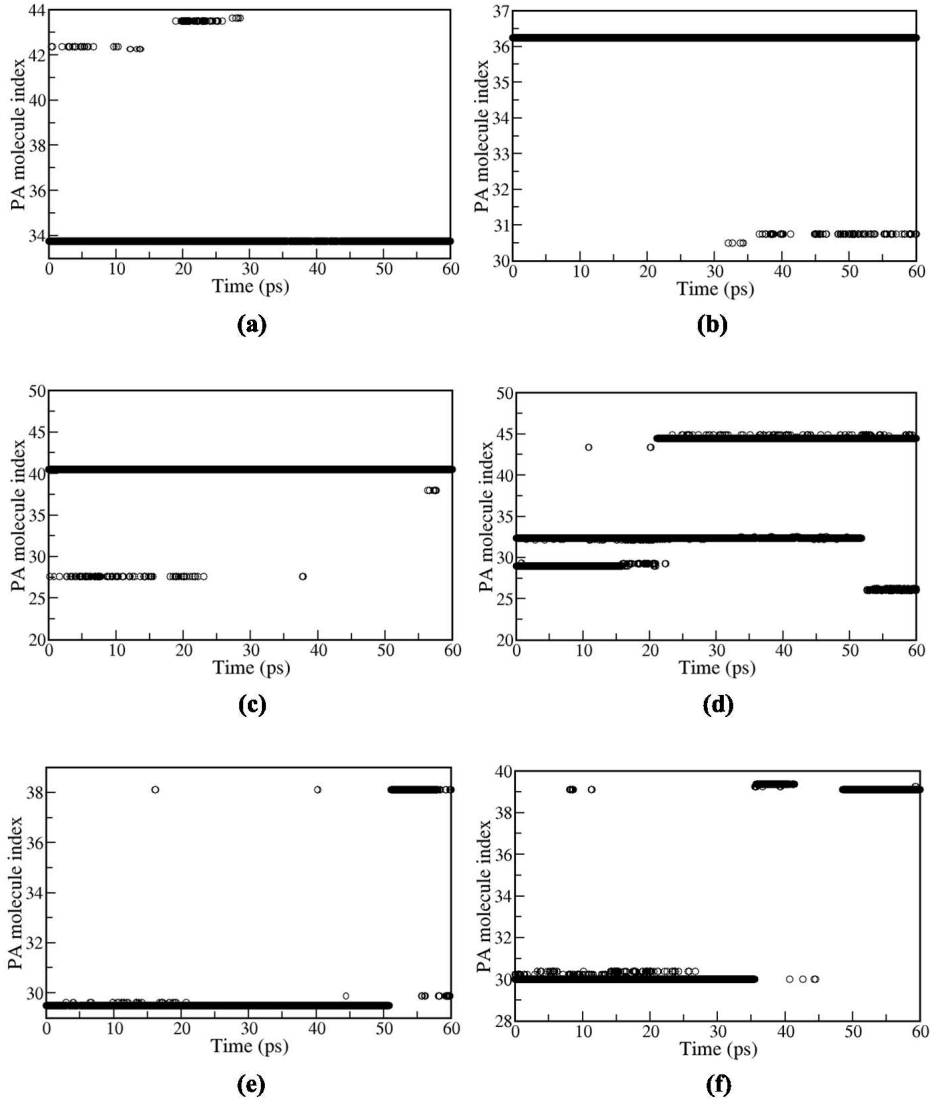

FIGURE 6.5: Evidence of non-constructive (a, b and c) and constructive (d, e and f) proton transport.

6.4 Conclusions

Ab initio molecular dynamics simulations were performed to understand the mechanism and role of triazole in proton transport. Unlike imidazole, triazole can accept and donate back protons through formation of transient h-bonds. Our simulations for the first time reveal that triazole actively takes part in proton transport via Grotthuss type of mechanism. When we add triazole in imidazole-phosphoric acid mixture, we observe increase in structural diffusion of proton towards total proton transport. As a result of higher structural proton diffusion, rate of total proton transfer increases. From our MD simulations we have observed increase in proton transfer due to structural diffusion by 44%, if we add TRZ in PA in place of IMD. We also simulated mixtures where triazole

is added in PA doped imidazole system. In this case we observed that structural proton diffusion increases by 21% compared to PA doped IMD system. This is much less than the PA-TRZ system. However, constituting only triazole based polymer is synthetically challenging and one may end up with mechanically less stable membrane. So triazole may be added in phosphoric acid doped imidazole based membrane which will help in enhancement of structural proton diffusion hence better proton conductivity.

Since, proton transport in immobilized PA doped heterocyclic based polymer system relies on structural diffusion, the findings of this study have a significant contribution towards fuel cell community. The results highlight the possibility of use of highly proton conducting proposed triazole based PEMs. Our simulations will help in designing efficient membrane with improved proton conductivity which can work at higher temperature. Further investigation on triazole based polymer, copolymer or blends of imidazole and triazole doped with PA may lead to a new potential membrane with favorable properties which possibly emerge as potential PEMFC for high temperature fuel cell.

Chapter 7

Quantum chemical calculations of proton affinity and proton transport activation energy barrier of various N-containing heterocyclic compounds in presence of PA

7.1 Introduction

From chapter 6, it is evident that PA doped triazole is a better candidate as a membrane material than PA doped imidazole. This is due to the fact that imidazole is a very good proton acceptor but do not donate back proton to PA which attributes to its high proton affiity. On the other hand, triazole takes as well as gives back proton to PA readily. To be a good proton conductor it must accept and donate back proton readily. Therefore, we explored other potential N-containing aromatic heterocycles which has significant proton affinity. In the present chapter, we have calculated proton affinity, interaction energy between PA and a large number of N-containing aromatic heterocyclic compounds. We have also calculated proton transport activation energy barrier for PA to these compounds and the back process. From energy barrier we will set the possibility of proton transfer from PA to these heterocyclic compounds and vice versa. This will help us in proposing new promising membrane material.

Very few computational studies are reported for understanding the fundamental of proton transfer process of N-containing heterocyclic compounds which can be used as a membrane material in presence of PA in high temperature PEMFC. Mautner et. al. reported the gas phase proton affinities of a series of azole compounds calculated at Møller−Plesset (MP2)/6-31G(d,p) level. [200] Authors have shown that the protonation sites are N3 in imidazole and oxazole and N4 in 1,2,4-triazole, the alternate protonation sites of N1, O, and N2, respectively, being less favorable by 53, 57, and 13 kcal/mol. The gas phase proton affinity calculations by Subbaraman et. al. for different substituted triazole molecules have shown that electron-donating groups have lesser effect on proton affinity than electon-withdrawng group. [201] Authors concluded that 4,5-dicyano-1H-[1,2,3]-triazole is a possible proton transport facilitator. Mane et. al. [186] calculated the free energies for the protonated phosphoric acid (PA), imidazole and 1,2,3-triazole system using density functional theory (DFT) at MP2 level. The free energy values are in following order: imidazole (ΔG = -224.7 Kcal/mol) >1,2,3-triazole (ΔG = -213.8 Kcal/mol) >PA (ΔG = -197.1 Kcal/mol). Vilčiauskas et al. [202] reported the proton transfer energetics in PA clusters using *ab initio* electronic structure calculations. Authors had given some indication of decrease in energy barrier for proton transfer and charge separation on increase in the system's size. They have also stated that proton transport in neat PA is facilitated by the rearrangement of molecules which lower the activation energy barrier and endothermicities for charge separation. Recently, Kreuer et al. studied that imidazole, benzimidazole and pyrazole can conduct proton like water when ionized. Therefore, these materials are good candidates for fuel cell membrane.

The aim of the present study is to examine the proton transfer properties of all possible N-contaning heterocyclic compounds. We have calculated gas phase proton affinity of the heterocyclic compounds which are the basic unit in a PEM. Since these heterocyclic based polymer conducts proton in presence of PA, we have been motivated to consider cases where PA interacts with these compounds. It is important to know how the varying molecular structure of different N-containing heterocyclic compounds effects the interaction energy. However, attention was paid to one type of (N-type) hydrogen bonding the complex may form and their interaction energy were calculated and compared. We have also investigated the proton transfer energetics in these compounds in presence of PA with *ab initio* electronic structure calculations. The chapter is organized as follows: first section contains the methodology used to calculate proton affinity, interaction energy of the complex and proton transfer energetics. The method section is followed by discussion describing these properties of various N-containing heterocyclic compounds and how we can tune these properties to get better proton conductivity in turn more efficiency of the fuel cell.

Calculation of proton affinity The proton affinity of a substrate (A) is written as the difference between electronic energy of the protonated substrate (AH^+) and the neutral substrate (A).

$$A + H^+ = AH^+ \tag{7.1}$$

Zero-point energy (ZPE) was considered here. Therefore, PA was defined here as

$$Proton\ affinity = \Delta E^{electronic} - \Delta ZPE \tag{7.2}$$

For all the model systems (including all the substituents), proton affinity values were calculated and compared.

Calculation of interaction energy Interaction energy (E_{int}) between two molecules A and B was defined as the difference between the optimized energy of the complex (AB) and the sum of the optimized energy of individual compounds (A and B).

$$E_{int} = E_{AB} - (E_A + E_B) \tag{7.3}$$

ZPE corrections and basis set superposition error (BSSE) calculations were done and incorporated to obtain the corrected interaction energy.

Calculation of energy barrier for proton transfer Energy barrier for proton transfer from PA molecule to the substrate were calculated by determining the potential energy surface (PES). The PES scan method was used as implemented in gaussian09. In this method, a hydrogen atom was transfered from PA molecule to substrate with 0.02 Å in each step. In each step, geometry was optimized using M06 functional with 6-311g(d,p) basis set under the distance constrained of neighbouring N atoms of different heterocyclic compounds and O atoms of PA.

All the electronic structure calculations were performed using Gaussian 09 code. [203] Proton affinity of simple and substituted N-containing heterocyclic units were calculated by optimizing the geometry of neutral ring and charged ring using M06 functional and 6-311g (d, p) basis set. ZPE values were also calculated and considered while comparing proton affinities for all the structures. The energy barrier for proton transfer from PA to the heterocyclic units were determined using the potential energy surface (PES) scan method as implemented in Gaussian 09 code. Before scanning the potential energy surface, all the heterocyclic units with phosphoric acid were optimized using M06/6-311g (d, p) level and scanning started from the optimized distance. A hydrogen atom was transferred from PA to N-containing heterocyclic unit and vice-versa with an increment of 0.02 Å distance and the transition structures at each point of the scan was optimized

at the M06/6-311g (d, p) level. This is performed by constraining the distance between donor O atom of the PA and acceptor N-atom of the heterocyclic unit for all structures.

7.2 Results and Discussion

7.2.1 Proton affinity

In HT-PEMFC, PA is used as a solvent and proton conduction occurs through acid-base interaction. PA donates proton to the acceptor sites of the base (in this case bare N of the heterocyclic compounds). Therefore, the compounds with basic sites having sufficient proton accepting capacity can take proton from PA. This is why we have taken imidazole, triazole, pyrazole, oxazole, thiazole and pyridine as a membrane material compounds which have one N free that can take proton from PA. We have also considered 1,2,3-1H triazole, 1,2,4-1H triazole and 1,2,4 oxadiazole with two basic N atoms acting as a proton acceptor. We calculated the capacity of each N to associate proton. Apart from these compounds, 1,2,3-2H triazole, 1,2,4-4H triazole and 1,3,4 oxadiazole were studied which have two equivalent N atoms that acts as basic sites. Proton transport is strongly dependent on the proton accepting capacity of the basic sites (bare N in this study) from the donor sites of the acid as well as back donating capacity to acid. Therefore, for all the model systems, we calculated proton affinities which gave us an idea about the extent of proton transport from PA to different N-containing heterocyclic compounds and indirectly the reverse path. The proton affinities of all these model systems are listed in Table 7.1. We can see in Table 7.1 that imidazole has the highest proton affinity (-224.648 Kcal/mol). This is the reason it was found to take proton from PA in the optimization step but did not give it back to PA as discussed in chapter 6 as well. [102] As a result, long range proton transport gets affected. Hence, our focus is to find a compound which has somewhat lower proton affinity compared to imidazole but not too low so that both way proton transfer occurs. We can find in Table 7.1 that N2 position of 1,2,3triazole-1H and 1,2,3-triazole-2-H, tetrazole and all oxadiazole compounds have very low proton affinity. Except these compounds, all the other heterocyclic compounds under study have considerable amount of proton affinity (10-20 Kcal/mol lower than Imidazole). Therefore, these compounds associate proton not as strongly like imidazole. As a result, these compounds have the possibilities to donate back the proton to PA like 1,2,3-1H triazole as presented in chapter 6.

TABLE 7.1: Proton affinity (kcal/mol) of all N-containing Heterocyclic Unit at the M06/6-311g(d,p) level

Heterocyclic Unit	Chemical structure	E_{elec} (a.u)	E_{elec}+ZPE (a.u)	E_{elec}+H (a.u)	Proton affinity (kcal/mol)
Imidazole	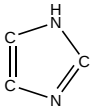	-226.113	-226.042	-226.037	-224.271
Imidazole cation	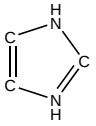	-226.484	-226.400	-226.395	
1-2-3-triazole-1-H	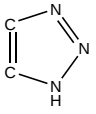	-242.120	-242.061	-242.057	-200.901
1-2-3-triazole-1-H cation(at N2)	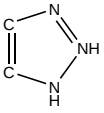	-242.454	-242.382	-242.377	
1-2-3-triazole-1-H	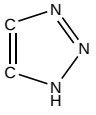	-242.120	-242.061	-242.057	-212.546
1-2-3-triazole-1-H cation(at N3)	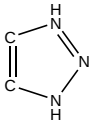	-242.473	-242.400	-242.395	
1-2-3-triazole-2-H	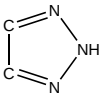	-242.128	-242.069	-242.064	-196.193
1-2-3-triazole-2-H cation	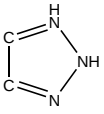	-242.454	-242.382	-242.377	
1-2-4-triazole-1-H	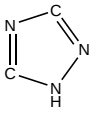	-242.150	-242.091	-242.086	-200.564
1-2-4-triazole-1-H cation(at N2)	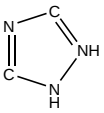	-242.482	-242.411	-242.406	

Heterocyclic Unit	Chemical structure	E_{elec} (a.u)	E_{elec}+ZPE (a.u)	E_{elec}+H (a.u)	Proton affinity (kcal/mol)
1-2-4-triazole-1-H	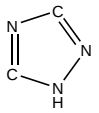	-242.150	-242.091	-242.086	-210.467
1-2-4-triazole-1-H cation(at N4)	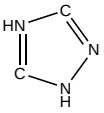	-242.499	-242.426	-242.421	
1-2-4-triazole-4-H	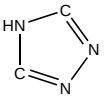	-242.138	-242.079	-242.075	-217.745
1-2-4-triazole-4-H cation	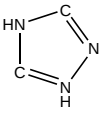	-242.499	-242.426	-242.421	
1-3-4-oxadiazole	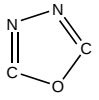	-262.001	-261.955	-261.950	-199.671
1-3-4-oxadiazole cation	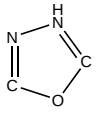	-262.333	-262.273	-262.268	
1-2-4-oxidiazole		-261.991	-261.944	-261.940	-187.963
1-2-4-oxadiazole cation(at N2)	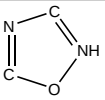	-262.303	-262.244	-262.239	
1-2-4-oxadiazole	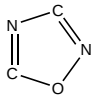	-261.991	-261.944	-261.940	191.474
1-2-4-oxadiazole cation(at N4)	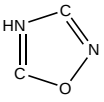	-262.309	-262.250	-262.245	

Heterocyclic Unit	Chemical structure	E_{elec} (a.u)	E_{elec}+ZPE (a.u)	E_{elec}+H (a.u)	Proton affinity (kcal/mol)
Pyrazole	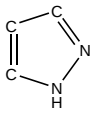	-226.095	-226.024	-226.019	-212.852
Pyrazole cation	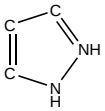	-226.447	-226.363	-226.358	
Oxazole		-245.975	-245.916	-245.912	-207.471
Oxazole cation	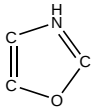	-246.319	-246.247	-246.242	
Thiazole	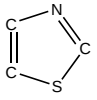	-568.954	-568.899	-568.894	-213.586
Thiazole cation	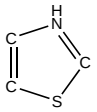	-569.308	-569.240	-569.235	
Pyridine	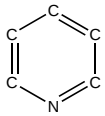	-248.149	-248.061	-248.056	-220.744
Pyridine cation	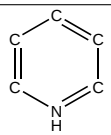	-248.515	-248.413	-248.408	

7.2.2 Interaction energy

Since N-containing heterocyclic compound based membranes transport proton in presence of PA, it is important to understand the interaction energy between these compounds and PA. Table 7.2 lists calculated gas phase interaction energy between all the N-containing heterocyclic compounds and PA molecules. Optimized geometry of PA and hetrocyclic compounds intearacting are shown in Figure 7.1. There are two types of H-bonding interactions between PA and these heterocyclic compounds where: i) N atom of these heterocyclic compounds acts as proton donor and O atom of PA acts as an acceptor and cases where ii) O atom of PA acts as proton donor and N atom of

heterocyclic compounds acts as acceptor. In this study, we have calculated interaction energy based on H-bonding interaction where N atom of heterocyclic compounds act as an acceptor. Li et. al. reported that this type of interaction is stronger among the above mentioned two types of interactions. [178] A more negative energy value in Table 7.2 reflects a stronger interaction. It is evident from Table 7.2 that imidazole has higher interaction energy with PA which points to its high proton affinity. We can clearly see from Table 7.1 and Table 7.2 that interaction energy (where bare N of heterocyclic compounds act as an proton acceptor) between N-containing heterocyclic compounds and PA depends on the proton affinity of the bare N.

TABLE 7.2: Interaction energy (kcal/mol) of all N-containing Heterocyclic Unit at the M06/6-311g(d,p) level.

Heterocyclic Unit	E_{elec} (a.u)	$E_{elec+ZPE}$ (a.u)	$E_{elec+ZPE+BSSE}$ (a.u)	E_{int} (kcal/mol)
PA	-644.1083	-644.0588	——	——
Imidazole	-226.1135	-226.0426	——	——
Imidazole —— PA	-870.2493	-870.1270	-870.1230	13.6
1-2-3-triazole -1-H	-242.1206	-242.0617	——	——
1-2-3-triazole 1-H at N3 —— PA	-886.2509	-886.1401	-886.1367	10.2
1-2-3-triazole 1-H at N2 —— PA	-886.2544	-886.1438	-886.1400	12.2
1-2-3-triazole 2-H	-242.1288	-242.0692	—-	—-
1-2-3-triazole 2-H——PA	-886.2588	-886.1477	-886.1442	10.2
1-2-4-triazole 1-H	-242.1505	-242.0909	——	——
1-2-4-triazole 1-H at N4 —— PA	-886.2822	-886.1705	-886.1669	10.8
1-2-4-triazole 1-H at N2 —— PA	-886.2829	-886.1712	-886.1672	10.9
1-2-4-triazole 4-H	-242.1388	-242.0799	——	——
1-2-4-triazole 4-H —— PA	-886.2719	-886.1612	-886.1577	11.9
Pyrazole	-226.0952	-226.0243	——	——
Pyrazole —— PA	-870.2310	-870.1081	-870.1040	13.1
Oxazole	-245.9752	-245.9167	——	——
Oxazole —— PA	-890.1051	-889.9950	-889.9916	10.1
Thiazole	-568.9545	-568.8997	——	——
Thiazole —— PA	-1213.0884	-1212.9820	-1212.9781	12.3
Pyridine	-248.1497	-248.0618	——	——
Pyridine —— PA	-892.2839	-892.1443	-892.1403	12.4
Tetrazole	-258.1521	-258.1052	——	——
Tetrazole —— PA	-902.2805	-902.1818	-902.1781	8.8

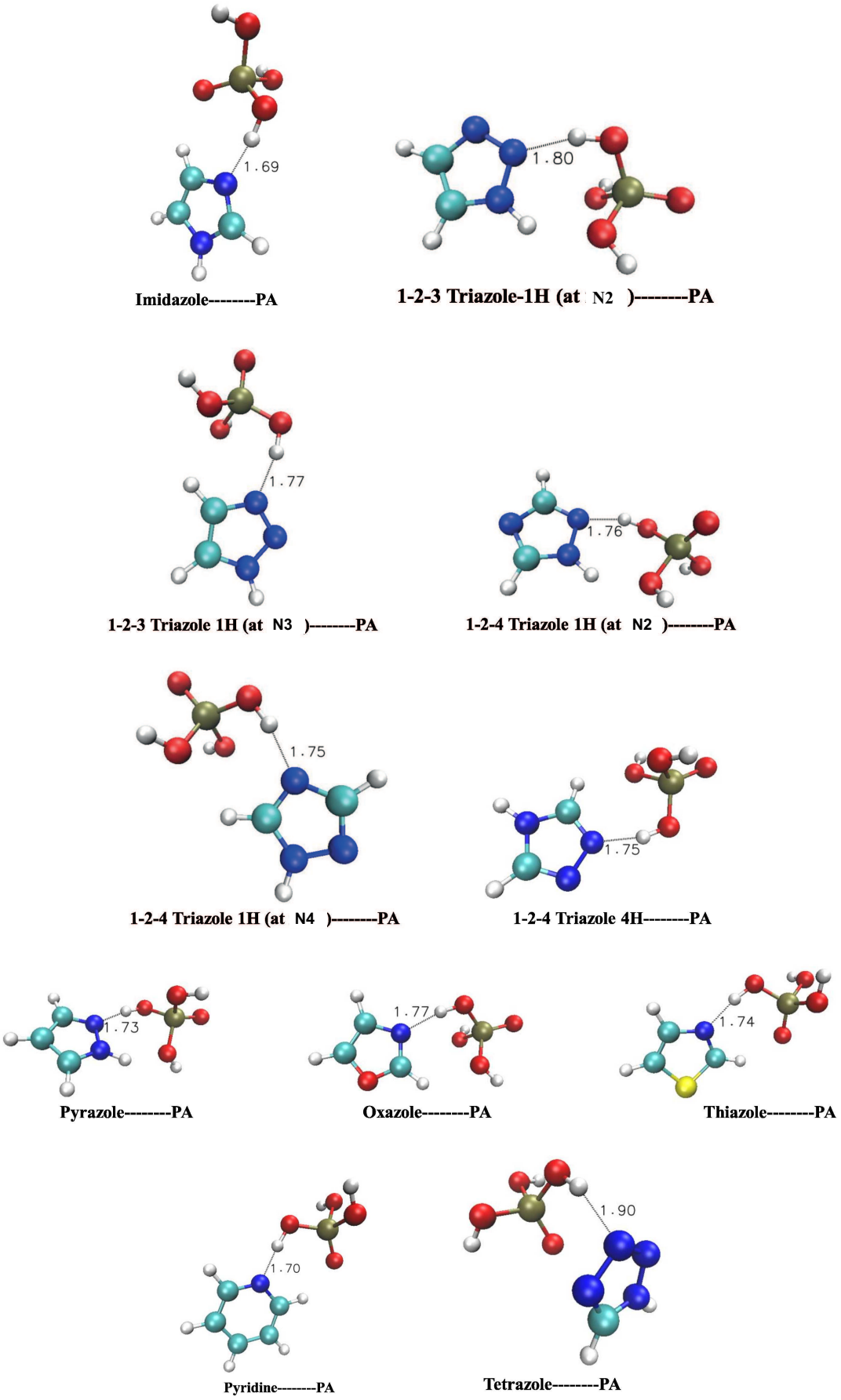

FIGURE 7.1: Optimized geometry of N-containing heterocyclic compounds interacting with PA.

7.2.3 Energy barrier for proton transport

Pair of PA and various N-containing heterocyclic compounds were optimized using the methodology described in the previous section. These optimized conformations, confirmed by vibrational frequency analysis, were used as a starting structure for proton transfer energy barrier calculations. Potential energy surface scan were performed along the proton transfer coordinates maintaining the constraint distance between N of heterocyclic compounds and O of PA. The energy profile of the proton transfer obtained by the above mentioned technique along with starting and final conformations are shown in Figure 7.2. Since a novel proton conducting material take as well as give back the proton readily to PA, we calculated the proton transport activation energy barrier for proton transfer from PA to all the N-conatining heterocyclic compounds as well as protonated compounds to PA. These compounds must not have too high activation barrier for proton transport in both directions to be used in HT-PEMFCs. Table 7.3 summarizes the energy barriers for proton transport pathways between various N-containing heterocyclic compounds and PA. Table 7.3 indicates that energy barrier for proton transport from PA to heterocyclic compounds entirely depend on proton affinity of the corresponding compound. As the proton affinity increases, proton transport activation energy decreases. Therefore, for imidazole and pyridine, which have high proton affinity, energy required for proton transfer from PA to these compounds are lower. However, energy barrier for the proton transfer in reverse path i.e. from protonated imidazole/pyridine to PA is higher compared to other compounds under study. Chapter 6 already demonstrated that imidazole takes proton from PA readily but imidazole cation does not back transfer proton to PA whereas 1,2,3-1H triazole takes as well as give back to PA using N3. Hence, this compound can act as a reference. we can observe in Table 7.3 that except imidazole and pyridine all the compounds under consideration have low energy barrier for proton transport from cation compound to PA than PA to these compounds. From the Table 7.3, we can see that apart from 1,2,3-1H triazole at N3, 1,2,3-1H triazole at N2, 1,2,4triazole-4H can act as a promising membrane materials.

TABLE 7.3: Energy barrier (kcal/mol) of all the N-containing heterocyclic compounds at the M06/6-311g(d,p) level

Heterocyclic compound	Energy barrier (kcal/mol)
PA ⟶ Imidazole	12.5
Imidazole cation ⟶ PA	15.7
PA ⟶ 1-2-3-triazole -1-H (at N2)	19.9
1-2-3-triazole -1-H (at N2) cation ⟶ PA	7.9
PA ⟶ 1-2-3-triazole -1-H (at N3)	20.1
1-2-3-triazole -1-H (at N3) cation ⟶ PA	7.9
PA ⟶ 1-2-4-triazole -1-H (at N2)	17.9
1-2-4-triazole -1-H (at N2) cation ⟶ PA	11.2
PA ⟶ 1-2-4-triazole -1-H (at N4)	18.3
1-2-4-triazole -1-H (at N4) cation ⟶ PA	10.3
PA ⟶ 1-2-4-triazole -4-H	16.7
1-2-4-triazole -4-H cation ⟶ PA	7.6
PA ⟶ Pyrazole	14.8
Pyrazole cation ⟶ PA	16.4
PA ⟶ Oxazole	19.9
Oxazole cation ⟶ PA	9.0
PA ⟶ Thiazole	15.5
Thiazole cation ⟶ PA	12.3
PA ⟶ Pyridine	11.9
Pyridine cation ⟶ PA	12.1
PA ⟶ Tetrazole	30.5
Tetrazole cation ⟶ PA	14.2

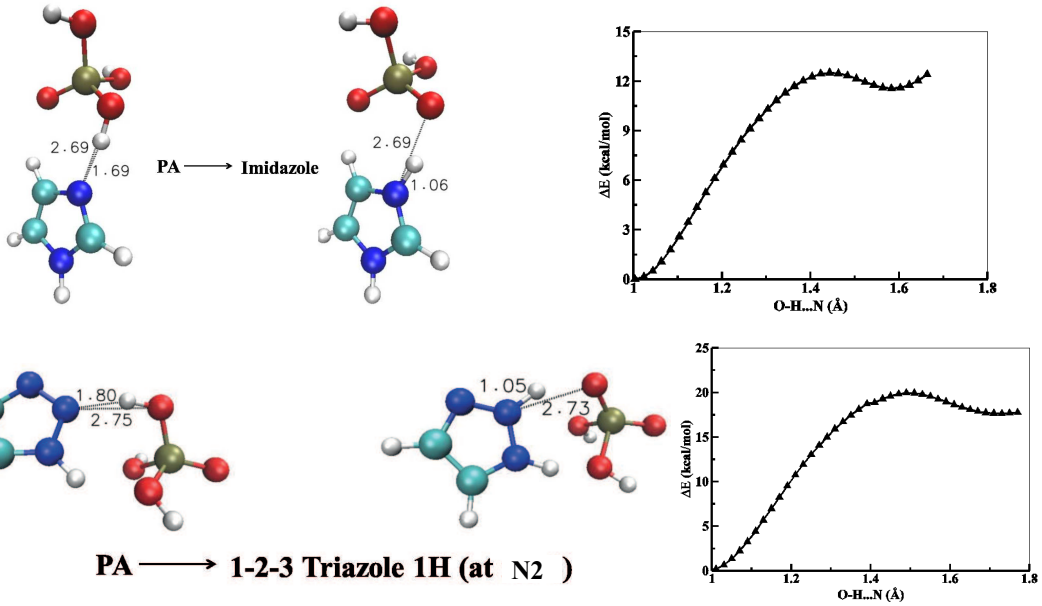

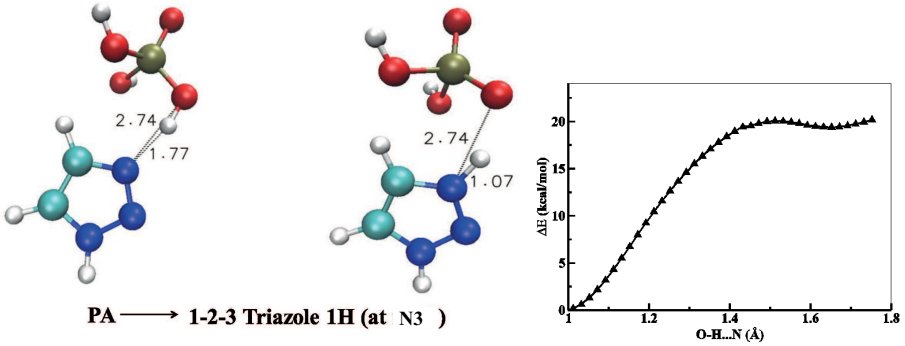

PA ⟶ 1-2-3 Triazole 1H (at N3)

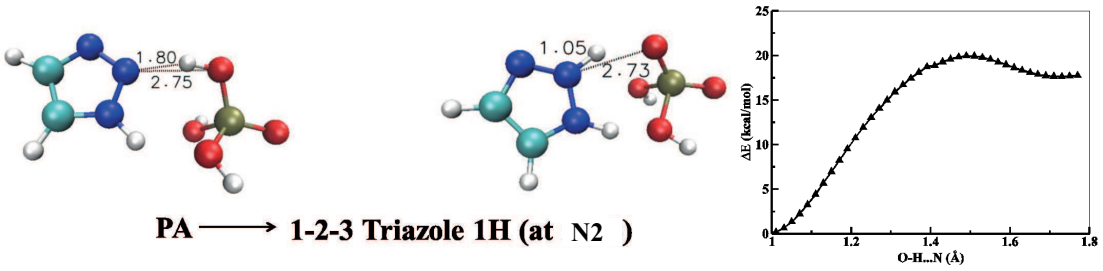

PA ⟶ 1-2-3 Triazole 1H (at N2)

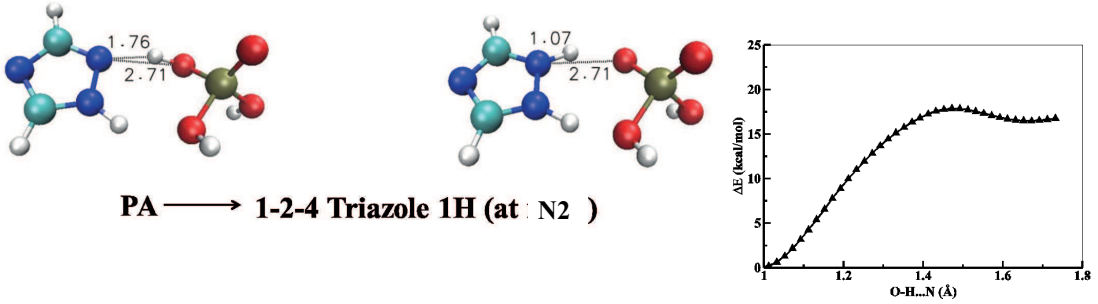

PA ⟶ 1-2-4 Triazole 1H (at N2)

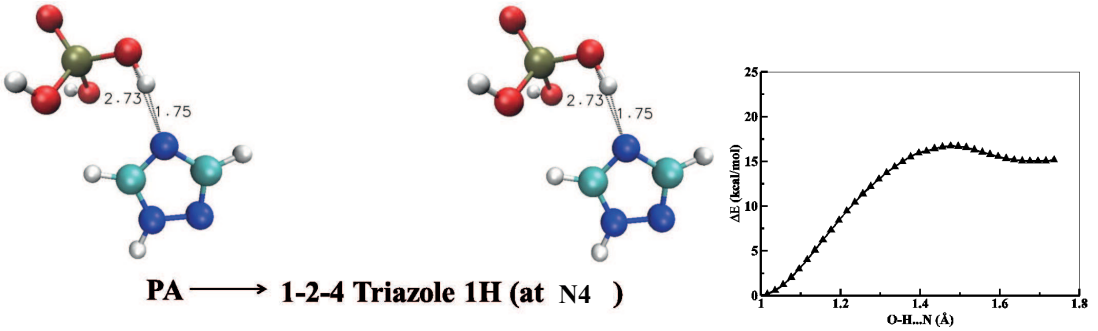

PA ⟶ 1-2-4 Triazole 1H (at N4)

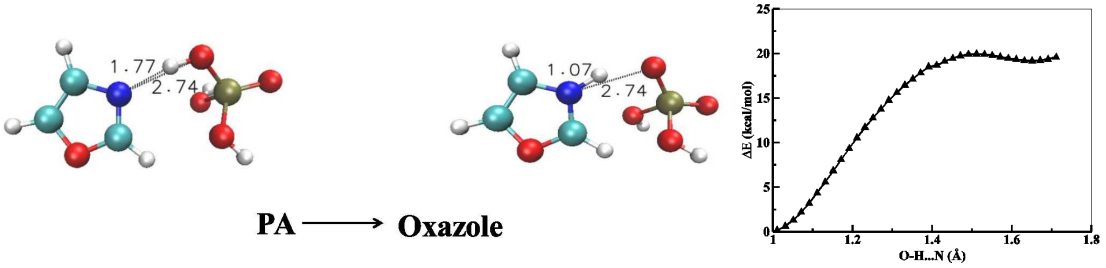

PA ⟶ Oxazole

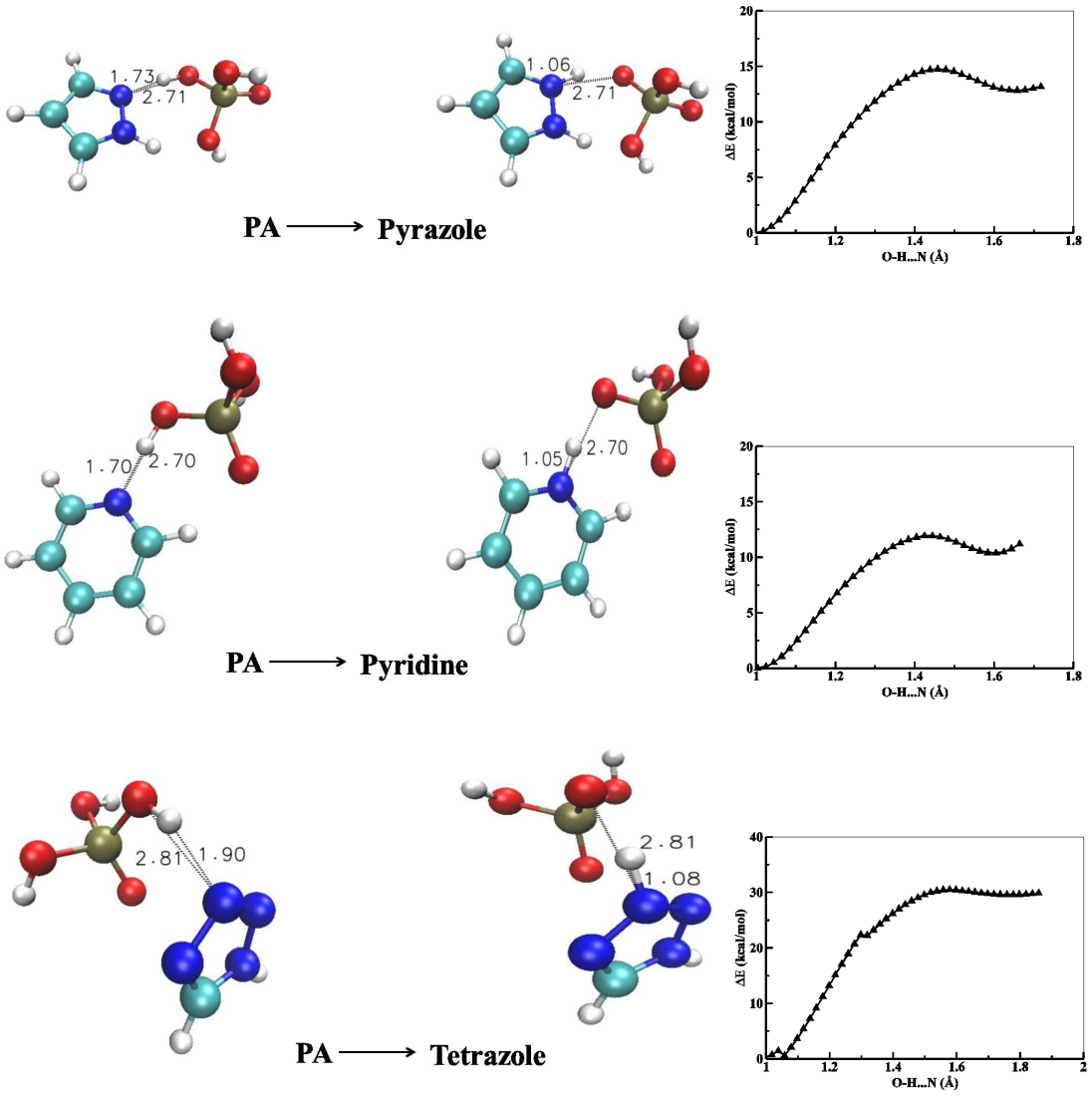

FIGURE 7.2: Energy barrier for proton transport from PA to N-containing aromatic heterocyclic compounds.

7.3 Conclusions

In this chapter, DFT based QM calculations using M06/6-311g(d,p) were performed to calculate gas-phase proton affinity, interaction energy, and energy barriers for different PT pathways between N-containing aromatic heterocyclic compounds and PA. Based on these results, following conclusions are made.

calculated gas-phase proton affinities, including ZPE corrections show that imidazole and pyridine have high proton affinity, 1,2,3-triazole-1H at N2, 1,2,4-triazole-1H at N2, all oxadiazole compounds and tetrazole have significantly low proton affinity. Rest of the compounds including 1,2,3-triazole-1H at N3, 1,2,4-triazole-1H at N4, pyrazole, oxazole and thiazole can be chosen as a membrane material based on their proton affinity. This

is due to the fact that larger the proton affinity of a compound, more prone it is to accept a proton and it is more difficult to dissociate the proton from the protonated compound.

Gas-phase interaction energy between PA and N-containing aromatic heterocyclic compounds suggest that hydrogen bond between H atom of PA and bare N atom of imidazole, pyrazole, thiazole and pyridine are the major interaction pattern at low PA doping level. For rest of the compounds under consideration have moderate strength of thi sparticular H-bond.

The calculated energy barriers for proton transport pathways from PA to N-containing aromatic heterocyclic compounds as well as protonated compounds to PA indicated that proton affinity is the governing factor for proton transfer process. Lower the energy barrier, easier the proton transport. The results suggested that 1,2,3-1H triazole protonated at N3, 1,2,3-1H triazole protonated at N2, 1,2,4triazole-4H can serve as potential membrane material in HT-PEMFC.

Chapter 8

Conclusions

In this thesis, with the aim of designing potential membrane materials for the high temperature PEMFC, various N-containing aromatic heterocycle based compounds in presence of PA were explored using a combination of classical MD, *ab initio* MD and DFT based QM methodology. The chapters in the thesis are organized such that starting from the understanding of existing membrane, we move to predict new better materials in terms of proton conductivity. However, all the systems under consideration are based on PA doped N-containing aromatic heterocycles.

In chapter 3 and 4, research is carried out on BI-PA mixtures at various doping levels of PA using classical MD. The results indicate that the mixtures do not phase separate which is because of several types of H-bonds formation between BI and PA. However, BI molecules are observed to form clusters. Detailed analysis of cluster size distribution reveals that at higher PA doping level, small BI clusters are connected through PA molecules. Since the contribution of PA towards proton transfer is more compared to BI, this structure forms favourable H-bonding path through which proton can easily transport. Highly ordered H-bonding network is observed to form in all the PA doping levels which restricts the intramolecular motion of BI. It was found that at higher PA doping level, BI molecules prefer to arrange in a parallel fashion among themselves which is absent at low PA concentration. Experimental data shows that with increase in the PA doping level, proton conductivity of the membrane increases. Therefore, the parallel arrangement is possibly the favourable orientation for formation of extended proton transport (PT) path (H-bonding network). All these structural level understanding helps in addressing proton transfer in a PEMFC. This study can be useful as a benchmark for exploring other membrane materials based on examining the PT path.

The investigation in chapter 4, is focused on the dynamical properties of BI-PA mixtures and how it changes with the amount of PA. Since classical MD can not deal with the

Grotthuss mechanism of PT, this study presents contribution of vehicular motion of BI as well as PA and the influence of PA doping level. The estimation of self-diffusion coefficients of BI and PA as a function of PA amount indicates the anomalous nature of vehicular motion. The reason behind this irregular diffusion of BI and PA are found to be structural heterogeneity in the BI-PA mixture which turns out due to the different types of H-bond formation. This study demonstrates the bridging H-bond formation between BI and PA which is found to be responsible for the slower diffusivity of BI and PA. The simulation study established the fact that diffusivity of BI as well as PA molecules in BI-PA mixture are spatially heterogeneous where different regions of varying mobility are observed in the system. This is due to the structural heterogeneity as a result of different types of H-bonds formation in the system. Different microscopic picture of dynamic heterogeneity (DH) and its qualitative as well as quantitative estimation with varying PA doping level are examined. The total DH present in the system can be originated from H-bonding, confinement and to some extent temperature. However, the study in chapter 4 only considered the contribution of H-bonding since, in this type of system, contribution of H-bonding is expected to be greater. Therefore, this chapter provides understanding of the heterogeneity in dynamics which originates from the inhomogeneous distribution of complex structural arrangements, are because of frequent H-bond breaking and making. This type of frequent rearrangement of H-bonds favors the PT. The stability of these H-bonds are examined and found to be very less which confirms the presence of transient H-bonds which serve as a path for proton hopping.

We have extended the structural investigation from BI to PBI in chapter 5 which enable us to understand the microscopic structure behind the experimentally observed properties of PA doped PBI system. This chapter reveals the effect of different structures of polybenzimidazoles (PBI and ABPBI) on proton conductivity. This chapter of the thesis presents detailed structural analysis of ABPBI and PBI, two most promising membrane materials of polybenzimidazole family, in melt as well as in PA using classical MD. The study shows that PA serves as a good solvent for both ABPBI and PBI. This is because both the ABPBI and PBI chains get elongated compared to their melt system in presence of PA as indicated from the end-to-end (R_{ee}) distance and radius of gyration (R_g) data. Different nature of curvature formation in case of ABPBI and PBI are established. Different nature of chain conformation causes different PA uptaking capacities of ABPBI and PBI which is observed from experiment. The arrangement of PA molecules along the backbone confirms that ABPBI has more PA absorbing capacity compared to PBI. The H-bonding interaction between polymer backbone atoms and PA were investigated which reveals the fact that number of H-bonding is more in case of ABPBI than PBI. Some PA molecules share H-bonds with two adjacent benzimidazole moieties in case of ABPBI which is absent in PBI. This type of sharing H-bonds make the ABPBI chain

more rigid. Thus, the conformational properties of the single polymer chains obtained in this work provide insight to explain the experimental findings including PA absorbing capacity, mechanical strength of polybenzimidazole chains.

So, in chapter 3 and 5 we explained structural and conformational properties of PA doped imidazole based systems. This has equipped us with fundamental understanding of structural arrangement, stability and formation of H-bonding network, which serves as proton transfer path. We explained vehicular motion of proton carriers (BI and PA) in chapter 4. After gaining all these informations our interest focuses to understand the Grotthuss mechanism of PT. Since classical MD can not deal with bond breaking and forming phenomenon, we performed *ab initio* MD to quantify Grotthuss hopping mechanism. Apart from estimating the PT mechanism in PA doped imidazole based system, we investigated the potential of triazole as a replacement of imidazole and also the possibility of using PA-imidazole-triazole ternary system in place of PA-imidazole system. The result indicates that unlike imidazole, triazole can accept and donate back proton through the formation of H-bonds. Therefore, triazole actively takes part in Grotthuss mechanism. Upon addition of triazole in PA-IMD mixture, structural diffusion is observed to increase. It is found that proton transfer due to structural diffusion increases by 44%, if we replace imidazole by triazole and by 21% if we add triazole in PA doped imidazole system. This is much less than the PA-triazole system. However, constituting only triazole based polymer is synthetically challenging and one may end up with mechanically less stable membrane. So, triazole may be added in phosphoric acid doped imidazole based membrane which will help in enhancement of structural proton diffusion hence better proton conductivity. Since, PT in immobilized PA doped heterocyclic compounds based polymer system relies on structural diffusion, the findings of this study have a significant contribution towards fuel cell community. The results highlight the possibility of using highly proton conducting proposed triazole based PEMs. Our simulations will help in designing efficient membrane with improved proton conductivity which can work at higher temperature. Further investigation on triazole based polymer, copolymer or blends of imidazole and triazole doped with PA may lead to a new potential membrane with favorable properties which possibly emerge as potential PEM for high temperature fuel cell.

In chapter 6, we searched for other potential N-containing aromatic heterocycles which has a significant proton affinity (but not too high like imidazole). Thus, using DFT based QM methodologies, we calculated proton affinity, interaction energy between PA and heterocycles and PT activation energy barrier from PA to these compounds and also the back process. From energy barrier, we can predict whether the proton transfer is possible in both directions for a given heterocyclic compound. The results indicate that 1,2,3-triazole-1H at N3, 1,2,4-triazole-1H at N4, pyrazole, oxazole and thiazole can be

chosen as a membrane material based on their proton affinity. However, proton transfer activation energy barrier is too high for pyrazole, oxazole and thiazole. Since, lower the energy barrier, easier the PT, the result suggests that 1,2,3-1H triazole protonated at N3, 1,2,3-1H triazole protonated at N2, 1,2,4triazole-4H can serve as potential membrane material in HT-PEMFC. We can even tune these properties further by adding various electron withdrawing or donating substituents to the heterocyclic compounds in order to get improved conductivity. Thus, overall the thesis presents an account of research exploring the possibility of using a large number of PA-doped N-containing aromatic heterocycle based compounds as a membrane material for high temperature PEMFC.

Bibliography

[1] Akihiro Yamasaki. An overview of co2 mitigation options for global warming-emphasizing co2 sequestration options. *Journal of Chemical Engineering of Japan*, 36(4):361–375, 2003.

[2] CE Milliken and RC Ruhl. Low cost, high efficiency reversible fuel cell systems. In *Proceedings of the 2002 US DOE Hydrogen Program Review, NREL/CP-610-32405*, pages 1–14, 2002.

[3] Jung-Min Kwon, Eung-Ho Kim, Bong-Hwan Kwon, and Kwang-Hee Nam. High-efficiency fuel cell power conditioning system with input current ripple reduction. *Industrial Electronics, IEEE Transactions on*, 56(3):826–834, 2009.

[4] A. Emadi, K. Rajashekara, S.S. Williamson, and S.M. Lukic. Topological overview of hybrid electric and fuel cell vehicular power system architectures and configurations. *Vehicular Technology, IEEE Transactions on*, 54(3):763–770, May 2005. ISSN 0018-9545. doi: 10.1109/TVT.2005.847445.

[5] A Boudghene Stambouli and E Traversa. Fuel cells, an alternative to standard sources of energy. *Renewable and Sustainable Energy Reviews*, 6(3):295 – 304, 2002. ISSN 1364-0321. doi: http://dx.doi.org/10.1016/S1364-0321(01)00015-6. URL http://www.sciencedirect.com/science/article/pii/S1364032101000156.

[6] Frano Barbir and Teresa Gomez. Efficiency and economics of proton exchange membrane (pem) fuel cells. *International Journal of Hydrogen Energy*, 21(10): 891–901, 1996.

[7] Kwi Seong Jeong and Byeong Soo Oh. Fuel economy and life-cycle cost analysis of a fuel cell hybrid vehicle. *Journal of Power Sources*, 105(1):58–65, 2002.

[8] Isa Bar-On, Randy Kirchain, and Richard Roth. Technical cost analysis for pem fuel cells. *Journal of Power Sources*, 109(1):71–75, 2002.

[9] Tushar V Choudhary and DW Goodman. Co-free fuel processing for fuel cell applications. *Catalysis Today*, 77(1):65–78, 2002.

[10] KD Kreuer. On the development of proton conducting polymer membranes for hydrogen and methanol fuel cells. *Journal of membrane science*, 185(1):29–39, 2001.

[11] Jung-Ho Wee. Applications of proton exchange membrane fuel cell systems. *Renewable and Sustainable Energy Reviews*, 11(8):1720 – 1738, 2007. ISSN 1364-0321. doi: http://dx.doi.org/10.1016/j.rser.2006.01.005. URL http://www.sciencedirect.com/science/article/pii/S1364032106000281.

[12] B. Kohlstruck. Applications with proton exchange membrane (pem) fuel cells for a deregulated market place. In *Electricity Distribution, 2001. Part 1: Contributions. CIRED. 16th International Conference and Exhibition on (IEE Conf. Publ No. 482)*, volume 4, pages 5 pp. vol.4–, 2001. doi: 10.1049/cp:20010838.

[13] *ASSESSMENT OF HYDROGEN-FUELED PROTON EXCHANGE MEMBRANE FUEL CELLS FOR DISTRIBUTED GENERATION AND COGENERATION*, 2000.

[14] F. Barbir and T. Gómez. Efficiency and economics of proton exchange membrane (pem) fuel cells. *International Journal of Hydrogen Energy*, 22(10–11): 1027 – 1037, 1997. ISSN 0360-3199. doi: http://dx.doi.org/10.1016/S0360-3199(96)00175-9. URL http://www.sciencedirect.com/science/article/pii/S0360319996001759.

[15] Nikhil H Jalani. *Development of nanocomposite polymer electrolyte membranes for higher temperature PEM fuel cells*. PhD thesis, WORCESTER POLYTECHNIC INSTITUTE, 2006.

[16] Nobuko Kariya, Atsushi Fukuoka, and Masaru Ichikawa. Zero-co2 emission and low-crossover 'rechargeable' pem fuel cells using cyclohexane as an organic hydrogen reservoir. *Chemical Communications*, -(6):690–691, 2003.

[17] A. Iulianelli, P. Ribeirinha, A. Mendes, and A. Basile. Methanol steam reforming for hydrogen generation via conventional and membrane reactors: A review. *Renewable and Sustainable Energy Reviews*, 29(0):355 – 368, 2014. ISSN 1364-0321. doi: http://dx.doi.org/10.1016/j.rser.2013.08.032. URL http://www.sciencedirect.com/science/article/pii/S1364032113005728.

[18] A. Heinzel, B. Vogel, and P. Hübner. Reforming of natural gas—hydrogen generation for small scale stationary fuel cell systems. *Journal of Power Sources*, 105(2):202 – 207, 2002. ISSN 0378-7753. doi: http://dx.doi.org/10.1016/S0378-7753(01)00940-5. URL http://www.sciencedirect.com/science/article/pii/S0378775301009405. 7th Ulmer Elektrochemische Tage.

[19] Yun Wang, Ken S. Chen, Jeffrey Mishler, Sung Chan Cho, and Xavier Cordobes Adroher. A review of polymer electrolyte membrane fuel cells: Technology, applications, and needs on fundamental research. *Applied Energy*, 88(4):981 – 1007, 2011. ISSN 0306-2619. doi: http://dx.doi.org/10.1016/j.apenergy.2010.09.030. URL http://www.sciencedirect.com/science/article/pii/S0306261910003958.

[20] Shanhai Ge, Baolian Yi, and Pingwen Ming. Experimental determination of electro-osmotic drag coefficient in nafion membrane for fuel cells. *Journal of The Electrochemical Society*, 153(8):A1443–A1450, 2006.

[21] Luísa A Neves, Pedro J Sebastião, Isabel M Coelhoso, and João G Crespo. Proton NMR Relaxometry Study of Nafion Membranes Modified with Ionic Liquid Cations. *J. Phys. Chem. B*, 115(27):8713–8723, 2011. doi: 10.1021/jp111238m. URL http://dx.doi.org/10.1021/jp111238m.

[22] R Devanathan, A Venkatnathan, and M Dupuis. Atomistic Simulation of Nafion Membrane. 2. Dynamics of Water Molecules and Hydronium Ions. *J. Phys. Chem. B*, 111(45):13006–13013, 2007. doi: 10.1021/jp0761057. URL http://dx.doi.org/10.1021/jp0761057.

[23] May Jean Cheah, Ioannis G Kevrekidis, and Jay Benziger. Effect of Interfacial Water Transport Resistance on Coupled Proton and Water Transport Across Nafion. *J. Phys. Chem. B*, 115(34):10239–10250, 2011. doi: 10.1021/jp204785t. URL http://dx.doi.org/10.1021/jp204785t.

[24] G. Suresh, Y.M. Scindia, A.K. Pandey, and A. Goswami. Self-diffusion coefficient of water in nafion-117 membrane with different monovalent counterions: a radiotracer study. *Journal of Membrane Science*, 250(1–2):39 – 45, 2005. ISSN 0376-7388. doi: http://dx.doi.org/10.1016/j.memsci.2004.10.013. URL http://www.sciencedirect.com/science/article/pii/S0376738804007082.

[25] Qingfeng Li, Chao Pan, Jens Oluf Jensen, Pernille Noyé, and Niels J Bjerrum. Cross-linked polybenzimidazole membranes for fuel cells. *Chem. Mater.*, 19(3): 350–352, 2007.

[26] Li Qingfeng, H.A. Hjuler, and N.J. Bjerrum. Phosphoric acid doped polybenzimidazole membranes: Physiochemical characterization and fuel cell applications. *J. Appl. Electrochem.*, 31(7):773–779, 2001. ISSN 0021-891X. doi: 10.1023/A:1017558523354. URL http://dx.doi.org/10.1023/A%3A1017558523354.

[27] M. Mamlouk and K. Scott. Phosphoric acid-doped electrodes for a pbi polymer membrane fuel cell. *International Journal of Energy Research*, 35(6):507–519,

2011. ISSN 1099-114X. doi: 10.1002/er.1708. URL http://dx.doi.org/10.1002/er.1708.

[28] Ram Devanathan. Recent developments in proton exchange membranes for fuel cells. *Energy Environ. Sci.*, 1:101–119, 2008. doi: 10.1039/B808149M. URL http://dx.doi.org/10.1039/B808149M.

[29] David E. Moilanen, D. B. Spry, and M. D. Fayer. Water dynamics and proton transfer in nafion fuel cell membranes. *Langmuir*, 24(8):3690–3698, 2008. doi: 10.1021/la703358a. URL http://dx.doi.org/10.1021/la703358a. PMID: 18220436.

[30] Satish G Kandlikar, Zijie Lu, and Thomas A Trabold. Current status and fundamental research needs in thermal management within a pemfc stack,". *in ASME Journal of Fuel Cells Science and Technology*, 2008.

[31] C Yang, P Costamagna, S Srinivasan, J Benziger, and A B Bocarsly. Approaches and Technical Challenges to High Temperature Operation of Proton Exchange Membrane Fuel Cells. *J. Power Sources*, 103(1):1–9, 2001. ISSN 0378-7753. doi: http://dx.doi.org/10.1016/S0378-7753(01)00812-6. URL http://www.sciencedirect.com/science/article/pii/S0378775301008126.

[32] Sanjiv Malhotra and Ravindra Datta. Membrane-supported nonvolatile acidic electrolytes allow higher temperature operation of proton-exchange membrane fuel cells. *Journal of The Electrochemical Society*, 144(2):L23–L26, 1997.

[33] KT Adjemian, SJ Lee, S Srinivasan, J Benziger, and AB Bocarsly. Silicon oxide nafion composite membranes for proton-exchange membrane fuel cell operation at 80-140 c. *Journal of the Electrochemical Society*, 149(3):A256–A261, 2002.

[34] R Savinell, E Yeager, D Tryk, U Landau, J Wainright, D Weng, K Lux, M Litt, and C Rogers. A polymer electrolyte for operation at temperatures up to 200 c. *Journal of the Electrochemical Society*, 141(4):L46–L48, 1994.

[35] Marc Doyle, Susan K Choi, and Grant Proulx. High-temperature proton conducting membranes based on perfluorinated ionomer membrane-ionic liquid composites. *Journal of the Electrochemical Society*, 147(1):34–37, 2000.

[36] S.M.J Zaidi, S.D Mikhailenko, G.P Robertson, M.D Guiver, and S Kaliaguine. Proton conducting composite membranes from polyether ether ketone and heteropolyacids for fuel cell applications. *Journal of Membrane Science*, 173(1):17 – 34, 2000. ISSN 0376-7388. doi: http://dx.doi.org/10.1016/S0376-7388(00)00345-8. URL http://www.sciencedirect.com/science/article/pii/S0376738800003458.

[37] Robert F Savinell and Morton H Litt. Proton conducting polymers used as membranes, June 11 1996. US Patent 5,525,436.

[38] Y-I Park, J-D Kim, and M Nagai. Increase of proton conductivity in amorphous phosphate–nafion membranes. *Journal of materials science letters*, 19(18):1621–1623, 2000.

[39] Mark Andrew Harmer and Qun Sun. Sol-gel derived porous microcomposite of perfluorinated ion-exchange polymer and metal oxide, October 26 2004. US Patent 6,809,218.

[40] KT Adjemian, S Srinivasan, J Benziger, and AB Bocarsly. Investigation of pemfc operation above 100 c employing perfluorosulfonic acid silicon oxide composite membranes. *Journal of power sources*, 109(2):356–364, 2002.

[41] Ronghuan He, Qingfeng Li, Jens Oluf Jensen, and Niels J. Bjerrum. Doping phosphoric acid in polybenzimidazole membranes for high temperature proton exchange membrane fuel cells. *Journal of Polymer Science Part A: Polymer Chemistry*, 45(14):2989–2997, 2007. ISSN 1099-0518. doi: 10.1002/pola.22053. URL http://dx.doi.org/10.1002/pola.22053.

[42] Q. Li, R. He, J.O. Jensen, and N.J. Bjerrum. Pbi-based polymer membranes for high temperature fuel cells – preparation, characterization and fuel cell demonstration. *Fuel Cells*, 4(3):147–159, 2004. ISSN 1615-6854. doi: 10.1002/fuce.200400020. URL http://dx.doi.org/10.1002/fuce.200400020.

[43] Minal More, Anurag Prakash Sunda, and Arun Venkatnathan. Polymer chain length, phosphoric acid doping and temperature dependence on structure and dynamics of an abpbi [poly (2, 5-benzimidazole)] polymer electrolyte membrane. *RSC Advances*, 4(38):19746–19755, 2014.

[44] Ronghuan He, Qingfeng Li, Anders Bach, Jens Oluf Jensen, and Niels J Bjerrum. Physicochemical properties of phosphoric acid doped polybenzimidazole membranes for fuel cells. *J. Membr. Sci.*, 277(1):38–45, 2006.

[45] Anthony Wereta, Matatjahu T Gehatia, and Donald R Wiff. Morphological and physical property effects for solvent cast films of poly-2, 5 (6) benzimidazole. *Polym. Eng. Sci.*, 18(3):204–209, 1978.

[46] Juan Antonio Asensio, Salvador Borrós, and Pedro Gómez-Romero. Polymer electrolyte fuel cells based on phosphoric acid-impregnated poly (2, 5-benzimidazole) membranes. *J. Electrochem. Soc.*, 151(2):A304–A310, 2004.

[47] JS Wainright, J-T Wang, D Weng, RF Savinell, and M Litt. Acid-doped polybenzimidazoles: A new polymer electrolyte. *J. Electrochem. Soc.*, 142(7):L121–L123, 1995.

[48] Qingfeng Li, Ronghuan He, Rolf W. Berg, Hans A. Hjuler, and Niels J. Bjerrum. Water uptake and acid doping of polybenzimidazoles as electrolyte membranes for fuel cells. *Solid State Ionics*, 168(1–2):177 – 185, 2004. ISSN 0167-2738. doi: http://dx.doi.org/10.1016/j.ssi.2004.02.013. URL http://www.sciencedirect.com/science/article/pii/S0167273804000967.

[49] M Litt, R Ameri, Y Wang, R Savinell, and J Wainwright. Polybenzimidazoles/phosphoric acid solid polymer electrolytes: mechanical and electrical properties. In *MRS Proceedings*, volume 548, page 313. Cambridge Univ Press, 1998.

[50] Ronghuan He, Quantong Che, and Baoying Sun. The acid doping behavior of polybenzimidazole membranes in phosphoric acid for proton exchange membrane fuel cells. *Fibers and Polymers*, 9(6):679–684, 2008. ISSN 1229-9197. doi: 10.1007/s12221-008-0107-0. URL http://dx.doi.org/10.1007/s12221-008-0107-0.

[51] Jingwei Hu, Huamin Zhang, Yunfeng Zhai, Gang Liu, and Baolian Yi. 500 h Continuous Aging Life Test on PBI/H3PO4 High-Temperature {PEMFC}. *International Journal of Hydrogen Energy*, 31(13):1855–1862, 2006. ISSN 0360-3199. doi: http://dx.doi.org/10.1016/j.ijhydene.2006.05.001. URL http://www.sciencedirect.com/science/article/pii/S0360319906001662.

[52] Ronghuan He, Qingfeng Li, Gang Xiao, and Niels J Bjerrum. Proton Conductivity of Phosphoric Acid Doped Polybenzimidazole and Its Composites with Inorganic Proton Conductors. *J. Membr. Sci.*, 226(1–2):169–184, 2003. ISSN 0376-7388. doi: http://dx.doi.org/10.1016/j.memsci.2003.09.002. URL http://www.sciencedirect.com/science/article/pii/S0376738803004216.

[53] David Mecerreyes, Hans Grande, Oscar Miguel, Estibalitz Ochoteco, Rebeca Marcilla, and Igor Cantero. Porous Polybenzimidazole Membranes Doped with Phosphoric Acid: Highly Proton-Conducting Solid Electrolytes. *Chem. Mater.*, 16(4):604–607, 2004. doi: 10.1021/cm034398k. URL http://dx.doi.org/10.1021/cm034398k.

[54] Lixiang Xiao, Haifeng Zhang, Eugene Scanlon, LS Ramanathan, Eui-Won Choe, Diana Rogers, Tom Apple, and Brian C Benicewicz. High-temperature polybenzimidazole fuel cell membranes via a sol-gel process. *Chem. Mater.*, 17(21):5328–5333, 2005.

[55] Tae-Ho Kim, Tae-Wook Lim, and Jong-Chan Lee. High-temperature fuel cell membranes based on mechanically stable para-ordered polybenzimidazole prepared by direct casting. *Journal of Power Sources*, 172(1):172 – 179, 2007. ISSN 0378-7753. doi: http://dx.doi.org/10.1016/j.jpowsour.2007.07.040. URL http://www.sciencedirect.com/science/article/pii/S0378775307015194. {ACS} San Francisco 2006 Fuel and Cell Symposium. American Chemical Society National Meeting. San Francisco, {CA} Sept 10-14 2006.

[56] J. A. Asensio and P. Gómez-Romero. Recent developments on proton conducting poly(2,5-benzimidazole) (abpbi) membranes for high temperature polymer electrolyte membrane fuel cells. *Fuel Cells*, 5(3):336–343, 2005. doi: 10.1002/fuce.200400081. URL http://dx.doi.org/10.1002/fuce.200400081.

[57] Hongwei Zhang and Pei Kang Shen. Recent development of polymer electrolyte membranes for fuel cells. *Chem. Rev.*, 112(5):2780–2832, 2012.

[58] P Stonehart. Electrocatalyst Advances for Hydrogen Oxidation in Phosphoric Acid Fuel Cells. *International Journal of Hydrogen Energy*, 9(11):921–928, 1984. ISSN 0360-3199. doi: http://dx.doi.org/10.1016/0360-3199(84)90157-5. URL http://www.sciencedirect.com/science/article/pii/0360319984901575.

[59] Qingfeng Li, Ronghuan He, Ji-An Gao, Jens Oluf Jensen, and Niels J Bjerrum. The co poisoning effect in pemfcs operational at temperatures up to 200 c. *J. Electrochem. Soc.*, 150(12):A1599–A1605, 2003.

[60] Der-Tau Chin and HowardH. Chang. On the conductivity of phosphoric acid electrolyte. *Journal of Applied Electrochemistry*, 19(1):95–99, 1989. ISSN 0021-891X. doi: 10.1007/BF01039396. URL http://dx.doi.org/10.1007/BF01039396.

[61] Milton Kerker and Wilton F. Espenscheid. Transference number of phosphoric acid by the e.m.f. method. *Journal of the American Chemical Society*, 80(4): 776–779, 1958. doi: 10.1021/ja01537a005. URL http://dx.doi.org/10.1021/ja01537a005.

[62] Noam Agmon. The grotthuss mechanism. *Chemical Physics Letters*, 244(5–6):456 – 462, 1995. ISSN 0009-2614. doi: http://dx.doi.org/10.1016/0009-2614(95)00905-J. URL http://www.sciencedirect.com/science/article/pii/000926149500905J.

[63] Yoong-Kee Choe, Eiji Tsuchida, Tamio Ikeshoji, Shunsuke Yamakawa, and Shiaki Hyodo. Nature of proton dynamics in a polymer electrolyte membrane, nafion: a first-principles molecular dynamics study. *Phys. Chem. Chem. Phys.*, 11:

3892–3899, 2009. doi: 10.1039/B819535H. URL http://dx.doi.org/10.1039/B819535H.

[64] Ryan Jorn and Gregory A. Voth. Mesoscale simulation of proton transport in proton exchange membranes. *The Journal of Physical Chemistry C*, 116(19): 10476–10489, 2012. doi: 10.1021/jp300040w. URL http://dx.doi.org/10.1021/jp300040w.

[65] Daan Frenkel and Berend Smit. Chapter 1 - introduction. In Daan Frenkel and Berend Smit, editors, *Understanding Molecular Simulation (Second Edition)*, pages 1 – 6. Academic Press, San Diego, second edition edition, 2002. ISBN 978-0-12-267351-1. doi: http://dx.doi.org/10.1016/B978-012267351-1/50003-1. URL http://www.sciencedirect.com/science/article/pii/B9780122673511500031.

[66] Matt K. Petersen and Gregory A. Voth. Characterization of the solvation and transport of the hydrated proton in the perfluorosulfonic acid membrane nafion. *The Journal of Physical Chemistry B*, 110(37):18594–18600, 2006. doi: 10.1021/jp062719k. URL http://dx.doi.org/10.1021/jp062719k. PMID: 16970488.

[67] D. Seeliger, C. Hartnig, and E. Spohr. Aqueous pore structure and proton dynamics in solvated nafion membranes. *Electrochimica Acta*, 50(21):4234 – 4240, 2005. ISSN 0013-4686. doi: http://dx.doi.org/10.1016/j.electacta.2005.03.071. URL http://www.sciencedirect.com/science/article/pii/S0013468605006055. Electrified Interfaces Selection of Papers from The 10th International Conference (ICEI 2004) 11-16 July 2004, Spa, Belguim.

[68] Shulu Feng and Gregory A. Voth. Proton solvation and transport in hydrated nafion. *The Journal of Physical Chemistry B*, 115(19):5903–5912, 2011. doi: 10.1021/jp2002194. URL http://dx.doi.org/10.1021/jp2002194. PMID: 21510678.

[69] Ram Devanathan, Arun Venkatnathan, Roger Rousseau, Michel Dupuis, Tomaso Frigato, Wei Gu, and Volkhard Helms. Atomistic simulation of water percolation and proton hopping in nafion fuel cell membrane. *The Journal of Physical Chemistry B*, 114(43):13681–13690, 2010. doi: 10.1021/jp103398b. URL http://dx.doi.org/10.1021/jp103398b. PMID: 20860379.

[70] Myvizhi Esai Selvan, David J. Keffer, and Shengting Cui. Reactive molecular dynamics study of proton transport in polymer electrolyte membranes. *The Journal of Physical Chemistry C*, 115(38):18835–18846, 2011. doi: 10.1021/jp203443c. URL http://dx.doi.org/10.1021/jp203443c.

[71] Detlef W. M. Hofmann, Liudmila Kuleshova, Bruno D'Aguanno, Vito Di Noto, Enrico Negro, Fosca Conti, and Michele Vittadello. Investigation of water structure in nafion membranes by infrared spectroscopy and molecular dynamics simulation. *The Journal of Physical Chemistry B*, 113(3):632–639, 2009. doi: 10.1021/jp806761h. URL http://dx.doi.org/10.1021/jp806761h. PMID: 19113878.

[72] Swati Vartak, Ata Roudgar, Anatoly Golovnev, and Michael Eikerling. Collective proton dynamics at highly charged interfaces studied by ab initio metadynamics. *The Journal of Physical Chemistry B*, 117(2):583–588, 2013.

[73] Yoong-Kee Choe, Eiji Tsuchida, Tamio Ikeshoji, Shunsuke Yamakawa, and Shi-aki Hyodo. Nature of proton dynamics in a polymer electrolyte membrane, nafion: a first-principles molecular dynamics study. *Physical Chemistry Chemical Physics*, 11(20):3892–3899, 2009.

[74] Guillermo A Luduena, Thomas D Kühne, and Daniel Sebastiani. Mixed grotthuss and vehicle transport mechanism in proton conducting polymers from ab initio molecular dynamics simulations. *Chemistry of Materials*, 23(6):1424–1429, 2011.

[75] Samad Ahadian, Hiroshi Mizuseki, and Yoshiyuki Kawazoe. Effects of hydration level, temperature, side chain and backbone flexibility of the polymer on the proton transfer in short-side-chain perfluorosulfonic acid membranes at low humidity conditions. *Journal of Membrane Science*, 369(1):339–349, 2011.

[76] E. Spohr, P. Commer, and A. A. Kornyshev. Enhancing proton mobility in polymer electrolyte membranes: lessons from molecular dynamics simulations. *The Journal of Physical Chemistry B*, 106(41):10560–10569, 2002. doi: 10.1021/jp020209u. URL http://dx.doi.org/10.1021/jp020209u.

[77] Seung Soon Jang, Valeria Molinero, Tahir Çağn, and William A. Goddard. Nanophase-segregation and transport in nafion 117 from molecular dynamics simulations: effect of monomeric sequence. *The Journal of Physical Chemistry B*, 108(10):3149–3157, 2004. doi: 10.1021/jp036842c. URL http://dx.doi.org/10.1021/jp036842c.

[78] Nick P. Blake, Greg Mills, and Horia Metiu. Dynamics of h2o and na+ in nafion membranes. *The Journal of Physical Chemistry B*, 111(10):2490–2494, 2007. doi: 10.1021/jp066473v. URL http://dx.doi.org/10.1021/jp066473v. PMID: 17298089.

[79] Shengting Cui, Junwu Liu, Myvizhi Esai Selvan, Stephen J. Paddison, David J. Keffer, and Brian J. Edwards. Comparison of the hydration and diffusion of

protons in perfluorosulfonic acid membranes with molecular dynamics simulations. *The Journal of Physical Chemistry B*, 112(42):13273–13284, 2008. doi: 10.1021/jp8039803. URL http://dx.doi.org/10.1021/jp8039803.

[80] Pavel V. Komarov, Igor N. Veselov, Peter P. Chu, and Pavel G. Khalatur. Mesoscale simulation of polymer electrolyte membranes based on sulfonated poly(ether ether ketone) and nafion. *Soft Matter*, 6:3939–3956, 2010. doi: 10.1039/B921369D. URL http://dx.doi.org/10.1039/B921369D.

[81] Stephen J. Paddison and James A. Elliott. Molecular modeling of the short-side-chain perfluorosulfonic acid membrane. *The Journal of Physical Chemistry A*, 109(33):7583–7593, 2005. doi: 10.1021/jp0524734. URL http://dx.doi.org/10.1021/jp0524734. PMID: 16834128.

[82] Stephen J. Paddison and James A. Elliott. The effects of backbone conformation on hydration and proton transfer in the 'short-side-chain' perfluorosulfonic acid membrane. *Solid State Ionics*, 177(26–32):2385 – 2390, 2006. ISSN 0167-2738. doi: http://dx.doi.org/10.1016/j.ssi.2006.03.015. URL http://www.sciencedirect.com/science/article/pii/S0167273806001597. Solid State Ionics 15: Proceedings of the 15th International Conference on Solid State Ionics, Part {II}.

[83] Vassiliki-Alexandra Glezakou, Michel Dupuis, and Christopher J. Mundy. Acid/base equilibria in clusters and their role in proton exchange membranes: computational insight. *Phys. Chem. Chem. Phys.*, 9:5752–5760, 2007. doi: 10.1039/B709752B. URL http://dx.doi.org/10.1039/B709752B.

[84] Mehmet A Ilhan and Eckhard Spohr. Ab initio molecular dynamics of proton networks in narrow polymer electrolyte pores. *Journal of Physics: Condensed Matter*, 23(23):234104, 2011. URL http://stacks.iop.org/0953-8984/23/i=23/a=234104.

[85] A. Roudgar, S.P. Narasimachary, and M. Eikerling. Ab initio study of surface-mediated proton transfer in polymer electrolyte membranes. *Chemical Physics Letters*, 457(4–6):337 – 341, 2008. ISSN 0009-2614. doi: http://dx.doi.org/10.1016/j.cplett.2008.04.016. URL http://www.sciencedirect.com/science/article/pii/S0009261408004946.

[86] Jessica M. J. Swanson, C. Mark Maupin, Hanning Chen, Matt K. Petersen, Jiancong Xu, Yujie Wu, and Gregory A. Voth. Proton solvation and transport in aqueous and biomolecular systems: insights from computer simulations. *The Journal of Physical Chemistry B*, 111(17):4300–4314, 2007. doi: 10.1021/jp070104x. URL http://dx.doi.org/10.1021/jp070104x. PMID: 17429993.

[87] Matt K. Petersen, Feng Wang, Nick P. Blake, Horia Metiu, and Gregory A. Voth. Excess proton solvation and delocalization in a hydrophilic pocket of the proton conducting polymer membrane nafion. *The Journal of Physical Chemistry B*, 109(9):3727–3730, 2005. doi: 10.1021/jp044535g. URL http://dx.doi.org/10.1021/jp044535g. PMID: 16851417.

[88] Shingo Urata, Jun Irisawa, Akira Takada, Wataru Shinoda, Seiji Tsuzuki, and Masuhiro Mikami. Molecular dynamics simulation of swollen membrane of perfluorinated ionomer. *The Journal of Physical Chemistry B*, 109(9):4269–4278, 2005. doi: 10.1021/jp046434o. URL http://dx.doi.org/10.1021/jp046434o. PMID: 16851491.

[89] Shengting Cui, Junwu Liu, Myvizhi Esai Selvan, David J. Keffer, Brian J. Edwards, and William V. Steele. A molecular dynamics study of a nafion polyelectrolyte membrane and the aqueous phase structure for proton transport. *The Journal of Physical Chemistry B*, 111(9):2208–2218, 2007. doi: 10.1021/jp066388n. URL http://dx.doi.org/10.1021/jp066388n. PMID: 17288476.

[90] James T. Wescott, Yue Qi, Lalitha Subramanian, and T. Weston Capehart. Mesoscale simulation of morphology in hydrated perfluorosulfonic acid membranes. *The Journal of Chemical Physics*, 124(13):134702, 2006. doi: http://dx.doi.org/10.1063/1.2177649. URL http://scitation.aip.org/content/aip/journal/jcp/124/13/10.1063/1.2177649.

[91] Kourosh Malek, Michael Eikerling, Qianpu Wang, Zhongsheng Liu, Shoko Otsuka, Ken Akizuki, and Mitsutaka Abe. Nanophase segregation and water dynamics in hydrated nafion: Molecular modeling and experimental validation. *The Journal of Chemical Physics*, 129(20):204702, 2008. URL http://scitation.aip.org/content/aip/journal/jcp/129/20/10.1063/1.3000641.

[92] James A Elliott and Stephen J Paddison. Modelling of morphology and proton transport in pfsa membranes. *Physical chemistry chemical physics*, 9(21):2602–2618, 2007.

[93] Y-L Ma, JS Wainright, MH Litt, and RF Savinell. Conductivity of pbi membranes for high-temperature polymer electrolyte fuel cells. *J. Electrochem. Soc.*, 151(1): A8–A16, 2004.

[94] Qingfeng Li, Jens Oluf Jensen, Robert F Savinell, and Niels J Bjerrum. High temperature proton exchange membranes based on polybenzimidazoles for fuel cells. *Prog. Polym. Sci.*, 34(5):449–477, 2009.

[95] Juan Antonio Asensio, Eduardo M. Sanchez, and Pedro Gomez-Romero. Proton-conducting membranes based on benzimidazole polymers for high-temperature pem fuel cells. a chemical quest. *Chem. Soc. Rev.*, 39:3210–3239, 2010. doi: 10.1039/B922650H. URL http://dx.doi.org/10.1039/B922650H.

[96] Jordan Mader, Lixiang Xiao, ThomasJ. Schmidt, and BrianC. Benicewicz. Polybenzimidazole/acid complexes as high-temperature membranes. In GüntherG. Scherer, editor, *Fuel Cells II*, volume 216 of *Advances in Polymer Science*, pages 63–124. Springer Berlin Heidelberg, 2008. ISBN 978-3-540-69763-3. doi: 10.1007/12˙2007˙129. URL http://dx.doi.org/10.1007/12_2007_129.

[97] Shuo Li. *Molecular simulation of phosphoric acid-doped polybenzimidazoles as high-temperature proton exchange membranes*. PhD thesis, University of Cincinnati, 2011.

[98] Shuo Li, JR Fried, and John Colebrook. Molecular simulations of poly (2, 5-benzimidazole): Effect of water concentration, phosphoric acid doping, and temperature on hydrogen bonding and vehicular diffusion. *Polym. Eng. Sci.*, 53(3): 597–608, 2013.

[99] Anurag Prakash Sunda, Minal More, and Arun Venkatnathan. A molecular investigation of the nanostructure and dynamics of phosphoric–triflic acid blends of hydrated abpbi [poly (2, 5-benzimidazole)] polymer electrolyte membranes. *Soft Matter*, 9(4):1122–1132, 2013.

[100] Suhua Zhu, Liuming Yan, Dongfang Zhang, and Qingxia Feng. Molecular dynamics simulation of microscopic structure and hydrogen bond network of the pristine and phosphoric acid doped polybenzimidazole. *Polymer*, 52(3):881–892, 2011.

[101] Linas Vilčiauskas, Mark E Tuckerman, Gabriel Bester, Stephen J Paddison, and Klaus-Dieter Kreuer. The mechanism of proton conduction in phosphoric acid. *Nature chemistry*, 4(6):461–466, 2012.

[102] Linas Vilčiauskas, Mark E Tuckerman, Jan P Melchior, Gabriel Bester, and Klaus-Dieter Kreuer. First principles molecular dynamics study of proton dynamics and transport in phosphoric acid/imidazole (2: 1) system. *Solid State Ionics*, 252: 34–39, 2013.

[103] Erwin Schrödinger. Quantization as an eigenvalue problem. *Annalen der Physik*, 79(4):361–376, 1926.

[104] M. Born and R. Oppenheimer. Zur quantentheorie der molekeln. *Annalen der Physik*, 389(20):457–484, 1927. ISSN 1521-3889. doi: 10.1002/andp.19273892002. URL http://dx.doi.org/10.1002/andp.19273892002.

[105] Douglas R Hartree. The wave mechanics of an atom with a non-coulomb central field. part ii. some results and discussion. In *Mathematical Proceedings of the Cambridge Philosophical Society*, volume 24, pages 111–132. Cambridge Univ Press, 1928.

[106] J. C. Slater. Note on hartree's method. *Phys. Rev.*, 35:210–211, Jan 1930. doi: 10.1103/PhysRev.35.210.2. URL http://link.aps.org/doi/10.1103/PhysRev.35.210.2.

[107] V Fock. Z. physik 61, 126 (1930); jc slater. *Phys. Rev*, 35:210, 1930.

[108] J. C. Slater. The theory of complex spectra. *Phys. Rev.*, 34:1293–1322, Nov 1929. doi: 10.1103/PhysRev.34.1293. URL http://link.aps.org/doi/10.1103/PhysRev.34.1293.

[109] L. H. Thomas. The calculation of atomic fields. *Mathematical Proceedings of the Cambridge Philosophical Society*, 23:542–548, 1 1927. ISSN 1469-8064. doi: 10.1017/S0305004100011683. URL http://journals.cambridge.org/article_S0305004100011683.

[110] Enrico Fermi. Un metodo statistico per la determinazione di alcune priorieta dell'atome. *Rend. Accad. Naz. Lincei*, 6(602-607):32, 1927.

[111] P. Hohenberg and W. Kohn. Inhomogeneous electron gas. *Phys. Rev.*, 136:B864–B871, Nov 1964. doi: 10.1103/PhysRev.136.B864. URL http://link.aps.org/doi/10.1103/PhysRev.136.B864.

[112] W. Kohn and L. J. Sham. Self-consistent equations including exchange and correlation effects. *Phys. Rev.*, 140:A1133–A1138, Nov 1965. doi: 10.1103/PhysRev.140.A1133. URL http://link.aps.org/doi/10.1103/PhysRev.140.A1133.

[113] M. C. Payne, M. P. Teter, D. C. Allan, T. A. Arias, and J. D. Joannopoulos. Iterative minimization techniques for *ab initio* total-energy calculations: molecular dynamics and conjugate gradients. *Rev. Mod. Phys.*, 64:1045–1097, Oct 1992. doi: 10.1103/RevModPhys.64.1045. URL http://link.aps.org/doi/10.1103/RevModPhys.64.1045.

[114] Mark E Tuckerman, P Jeffrey Ungar, Tycho von Rosenvinge, and Michael L Klein. Ab initio molecular dynamics simulations. *The Journal of Physical Chemistry*, 100 (31):12878–12887, 1996.

[115] Dominik Marx and Jurg Hutter. Ab initio molecular dynamics: Theory and implementation. *Modern methods and algorithms of quantum chemistry*, 1:301–449, 2000.

[116] R. Car and M. Parrinello. Unified approach for molecular dynamics and density-functional theory. *Phys. Rev. Lett.*, 55:2471–2474, Nov 1985. doi: 10.1103/PhysRevLett.55.2471. URL http://link.aps.org/doi/10.1103/PhysRevLett.55.2471.

[117] Douglas A. Gibson, Irina V. Ionova, and Emily A. Carter. A comparison of car—parrinello and born—oppenheimer generalized valence bond molecular dynamics. *Chemical Physics Letters*, 240(4):261 – 267, 1995. ISSN 0009-2614. doi: http://dx.doi.org/10.1016/0009-2614(95)00537-E. URL http://www.sciencedirect.com/science/article/pii/000926149500537E.

[118] G Galli and A Pasquarello. First-principles molecular dynamics. In *Computer Simulation in Chemical Physics*, pages 261–313. Springer, 1993.

[119] William L Jorgensen, David S Maxwell, and Julian Tirado-Rives. Development and testing of the opls all-atom force field on conformational energetics and properties of organic liquids. *JACS*, 118(45):11225–11236, 1996.

[120] George A. Kaminski, Richard A. Friesner, Julian Tirado-Rives, and William L. Jorgensen. Evaluation and reparametrization of the opls-aa force field for proteins via comparison with accurate quantum chemical calculations on peptides. *The Journal of Physical Chemistry B*, 105(28):6474–6487, 2001. doi: 10.1021/jp003919d. URL http://dx.doi.org/10.1021/jp003919d.

[121] B. R. Brooks, C. L. Brooks, A. D. Mackerell, L. Nilsson, R. J. Petrella, B. Roux, Y. Won, G. Archontis, C. Bartels, S. Boresch, A. Caflisch, L. Caves, Q. Cui, A. R. Dinner, M. Feig, S. Fischer, J. Gao, M. Hodoscek, W. Im, K. Kuczera, T. Lazaridis, J. Ma, V. Ovchinnikov, E. Paci, R. W. Pastor, C. B. Post, J. Z. Pu, M. Schaefer, B. Tidor, R. M. Venable, H. L. Woodcock, X. Wu, W. Yang, D. M. York, and M. Karplus. Charmm: The biomolecular simulation program. *Journal of Computational Chemistry*, 30(10):1545–1614, 2009. ISSN 1096-987X. doi: 10.1002/jcc.21287. URL http://dx.doi.org/10.1002/jcc.21287.

[122] Bernard R. Brooks, Robert E. Bruccoleri, Barry D. Olafson, David J. States, S. Swaminathan, and Martin Karplus. Charmm: A program for macromolecular energy, minimization, and dynamics calculations. *Journal of Computational Chemistry*, 4(2):187–217, 1983. ISSN 1096-987X. doi: 10.1002/jcc.540040211. URL http://dx.doi.org/10.1002/jcc.540040211.

[123] Chris Oostenbrink, Alessandra Villa, Alan E. Mark, and Wilfred F. Van Gunsteren. A biomolecular force field based on the free enthalpy of hydration and solvation: The gromos force-field parameter sets 53a5 and 53a6. *Journal*

of Computational Chemistry, 25(13):1656–1676, 2004. ISSN 1096-987X. doi: 10.1002/jcc.20090. URL http://dx.doi.org/10.1002/jcc.20090.

[124] Yong Duan, Chun Wu, Shibasish Chowdhury, Mathew C. Lee, Guoming Xiong, Wei Zhang, Rong Yang, Piotr Cieplak, Ray Luo, Taisung Lee, James Caldwell, Junmei Wang, and Peter Kollman. A point-charge force field for molecular mechanics simulations of proteins based on condensed-phase quantum mechanical calculations. *Journal of Computational Chemistry*, 24(16):1999–2012, 2003. ISSN 1096-987X. doi: 10.1002/jcc.10349. URL http://dx.doi.org/10.1002/jcc.10349.

[125] Mike P Allen and Dominic J Tildesley. *Computer simulation of liquids*. Oxford university press, 1989.

[126] R Leach Andrew. Molecular modelling: principles and applications, 2001.

[127] R.W Hockney, S.P Goel, and J.W Eastwood. Quiet high-resolution computer models of a plasma. *Journal of Computational Physics*, 14(2):148 – 158, 1974. ISSN 0021-9991. doi: http://dx.doi.org/10.1016/0021-9991(74)90010-2. URL http://www.sciencedirect.com/science/article/pii/0021999174900102.

[128] Berk Hess. P-lincs: a parallel linear constraint solver for molecular simulation. *Journal of Chemical Theory and Computation*, 4(1):116–122, 2008. doi: 10.1021/ct700200b. URL http://dx.doi.org/10.1021/ct700200b.

[129] Berk Hess, Henk Bekker, Herman J. C. Berendsen, and Johannes G. E. M. Fraaije. Lincs: A linear constraint solver for molecular simulations. *Journal of Computational Chemistry*, 18(12):1463–1472, 1997. ISSN 1096-987X. doi: 10.1002/(SICI)1096-987X(199709)18:12¡1463::AID-JCC4¿3.0.CO;2-H. URL http://dx.doi.org/10.1002/(SICI)1096-987X(199709)18:12<1463::AID-JCC4>3.0.CO;2-H.

[130] Jean-Paul Ryckaert, Giovanni Ciccotti, and Herman J.C Berendsen. Numerical integration of the cartesian equations of motion of a system with constraints: molecular dynamics of n-alkanes. *Journal of Computational Physics*, 23(3):327 – 341, 1977. ISSN 0021-9991. doi: http://dx.doi.org/10.1016/0021-9991(77)90098-5. URL http://www.sciencedirect.com/science/article/pii/0021999177900985.

[131] Herman JC Berendsen, J Pl M Postma, Wilfred F van Gunsteren, ARHJ DiNola, and JR Haak. Molecular dynamics with coupling to an external bath. *J. Chem. Phys.*, 81(8):3684–3690, 1984.

[132] Shuichi Nosé. A unified formulation of the constant temperature molecular dynamics methods. *The Journal of Chemical Physics*, 81(1):511–519, 1984. URL http://scitation.aip.org/content/aip/journal/jcp/81/1/10.1063/1.447334.

[133] William G. Hoover. Canonical dynamics: Equilibrium phase-space distributions. *Phys. Rev. A*, 31:1695–1697, Mar 1985. doi: 10.1103/PhysRevA.31.1695. URL http://link.aps.org/doi/10.1103/PhysRevA.31.1695.

[134] Giovanni Bussi, Davide Donadio, and Michele Parrinello. Canonical sampling through velocity rescaling. *The Journal of Chemical Physics*, 126(1):014101, 2007. doi: http://dx.doi.org/10.1063/1.2408420. URL http://scitation.aip.org/content/aip/journal/jcp/126/1/10.1063/1.2408420.

[135] David Van Der Spoel, Erik Lindahl, Berk Hess, Gerrit Groenhof, Alan E Mark, and Herman JC Berendsen. Gromacs: fast, flexible, and free. *J. Comput. Chem.*, 26(16):1701–1718, 2005.

[136] Berk Hess, Carsten Kutzner, David Van Der Spoel, and Erik Lindahl. Gromacs 4: algorithms for highly efficient, load-balanced, and scalable molecular simulation. *J. Chem. Theory Comput.*, 4(3):435–447, 2008.

[137] William L Jorgensen and Julian Tirado-Rives. The opls [optimized potentials for liquid simulations] potential functions for proteins, energy minimizations for crystals of cyclic peptides and crambin. *JACS*, 110(6):1657–1666, 1988.

[138] M. J. Frisch, G. W. Trucks, H. B. Schlegel, G. E. Scuseria, M. A. Robb, J. R. Cheeseman, G. Scalmani, V. Barone, B. Mennucci, G. A. Petersson, H. Nakatsuji, M. Caricato, X. Li, H. P. Hratchian, A. F. Izmaylov, J. Bloino, G. Zheng, J. L. Sonnenberg, M. Hada, M. Ehara, K. Toyota, R. Fukuda, J. Hasegawa, M. Ishida, T. Nakajima, Y. Honda, O. Kitao, H. Nakai, T. Vreven, J. A. Montgomery, Jr., J. E. Peralta, F. Ogliaro, M. Bearpark, J. J. Heyd, E. Brothers, K. N. Kudin, V. N. Staroverov, R. Kobayashi, J. Normand, K. Raghavachari, A. Rendell, J. C. Burant, S. S. Iyengar, J. Tomasi, M. Cossi, N. Rega, J. M. Millam, M. Klene, J. E. Knox, J. B. Cross, V. Bakken, C. Adamo, J. Jaramillo, R. Gomperts, R. E. Stratmann, O. Yazyev, A. J. Austin, R. Cammi, C. Pomelli, J. W. Ochterski, R. L. Martin, K. Morokuma, V. G. Zakrzewski, G. A. Voth, P. Salvador, J. J. Dannenberg, S. Dapprich, A. D. Daniels, Ö. Farkas, J. B. Foresman, J. V. Ortiz, J. Cioslowski, and D. J. Fox. Gaussian 09 Revision A.1, 2009. Gaussian Inc. Wallingford CT 2009.

[139] Curt M Breneman and Kenneth B Wiberg. Determining atom-centered monopoles from molecular electrostatic potentials. the need for high sampling density in formamide conformational analysis. *J. Comput. Chem.*, 11(3):361–373, 1990.

[140] John G Kirkwood. Theory of solutions of molecules containing widely separated charges with special application to zwitterions. *J. Chem. Phys.*, 2(7):351–361, 1934.

[141] Lars Onsager. Electric moments of molecules in liquids. *JACS*, 58(8):1486–1493, 1936.

[142] Liuming Yan, Suhua Zhu, Xiaobo Ji, and Wencong Lu. Proton hopping in phosphoric acid solvated nafion membrane: a molecular simulation study. *The Journal of Physical Chemistry B*, 111(23):6357–6363, 2007. doi: 10.1021/jp071005m. URL http://dx.doi.org/10.1021/jp071005m. PMID: 17518491.

[143] Santosh C. Kumbharkar, Prasad B. Karadkar, and Ulhas K. Kharul. Enhancement of gas permeation properties of polybenzimidazoles by systematic structure architecture. *Journal of Membrane Science*, 286(1–2):161 – 169, 2006. ISSN 0376-7388. doi: http://dx.doi.org/10.1016/j.memsci.2006.09.030. URL http://www.sciencedirect.com/science/article/pii/S0376738806006375.

[144] Hans Sillescu. Heterogeneity at the glass transition: a review. *Journal of Non-Crystalline Solids*, 243(2–3):81 – 108, 1999. ISSN 0022-3093. doi: http://dx.doi.org/10.1016/S0022-3093(98)00831-X. URL http://www.sciencedirect.com/science/article/pii/S002230939800831X.

[145] M. D. Ediger. Spatially heterogeneous dynamics in supercooled liquids. *Annual Review of Physical Chemistry*, 51(1):99–128, 2000. doi: 10.1146/annurev.physchem.51.1.99. URL http://dx.doi.org/10.1146/annurev.physchem.51.1.99. PMID: 11031277.

[146] Zhonghan Hu and Claudio J. Margulis. Heterogeneity in a room-temperature ionic liquid: Persistent local environments and the red-edge effect. *Proceedings of the National Academy of Sciences of the United States of America*, 103(4):831–836, 2006. doi: 10.1073/pnas.0507364103. URL http://www.pnas.org/content/103/4/831.abstract.

[147] Y. Rahmani, K. van der Vaart, B. van Dam, Z. Hu, V. Chikkadi, and P. Schall. Dynamic heterogeneity in hard and soft sphere colloidal glasses. *Soft Matter*, 8:4264–4270, 2012. doi: 10.1039/C2SM25267H. URL http://dx.doi.org/10.1039/C2SM25267H.

[148] M Scott Shell, Pablo G Debenedetti, and Frank H Stillinger. Dynamic heterogeneity and non-gaussian behaviour in a model supercooled liquid. *Journal of Physics: Condensed Matter*, 17(49):S4035, 2005.

[149] C. M. Roland, D. Fragiadakis, D. Coslovich, S. Capaccioli, and K. L. Ngai. Correlation of nonexponentiality with dynamic heterogeneity from four-point dynamic susceptibility 4(t) and its approximation t(t). *The Journal of Chemical Physics*, 133(12):124507, 2010. doi: http://dx.doi.org/10.1063/1.3481355. URL http://scitation.aip.org/content/aip/journal/jcp/133/12/10.1063/1.3481355.

[150] Yongxiang Gao and Maria L. Kilfoil. Intermittent and spatially heterogeneous single-particle dynamics close to colloidal gelation. *Phys. Rev. E*, 79:051406, May 2009. doi: 10.1103/PhysRevE.79.051406. URL http://link.aps.org/doi/10.1103/PhysRevE.79.051406.

[151] Daniele Coslovich, Lukas Strauss, and Gerhard Kahl. Hopping and microscopic dynamics of ultrasoft particles in cluster crystals. *Soft Matter*, 7:2127–2137, 2011. doi: 10.1039/C0SM00545B. URL http://dx.doi.org/10.1039/C0SM00545B.

[152] J. Habasaki, K. L. Ngai, and Y. Hiwatari. Molecular dynamics study of cage decay, near constant loss, and crossover to cooperative ion hopping in lithium metasilicate. *Phys. Rev. E*, 66:021205, Aug 2002. doi: 10.1103/PhysRevE.66.021205. URL http://link.aps.org/doi/10.1103/PhysRevE.66.021205.

[153] Walter Kob, Claudio Donati, Steven J. Plimpton, Peter H. Poole, and Sharon C. Glotzer. Dynamical heterogeneities in a supercooled lennard-jones liquid. *Phys. Rev. Lett.*, 79:2827–2830, Oct 1997. doi: 10.1103/PhysRevLett.79.2827. URL http://link.aps.org/doi/10.1103/PhysRevLett.79.2827.

[154] Claudio Donati, Jack F. Douglas, Walter Kob, Steven J. Plimpton, Peter H. Poole, and Sharon C. Glotzer. Stringlike cooperative motion in a supercooled liquid. *Phys. Rev. Lett.*, 80:2338–2341, Mar 1998. doi: 10.1103/PhysRevLett.80.2338. URL http://link.aps.org/doi/10.1103/PhysRevLett.80.2338.

[155] Donna N. Perera and Peter Harrowell. Relaxation dynamics and their spatial distribution in a two-dimensional glass-forming mixture. *The Journal of Chemical Physics*, 111(12):5441–5454, 1999. URL http://scitation.aip.org/content/aip/journal/jcp/111/12/10.1063/1.479804.

[156] Ryoichi Yamamoto and Akira Onuki. Heterogeneous diffusion in highly supercooled liquids. *Phys. Rev. Lett.*, 81:4915–4918, Nov 1998. doi: 10.1103/PhysRevLett.81.4915. URL http://link.aps.org/doi/10.1103/PhysRevLett.81.4915.

[157] Sharon C Glotzer. Spatially heterogeneous dynamics in liquids: insights from simulation. *Journal of Non-Crystalline Solids*, 274(1–3):342 – 355, 2000. ISSN 0022-3093. doi: http://dx.doi.org/10.1016/S0022-3093(00)00225-8. URL http://

www.sciencedirect.com/science/article/pii/S0022309300002258. Physics of Non-Crystalline Solids 9.

[158] K. Karatasos and M. Krystallis. Dynamics of counterions in dendrimer polyelectrolyte solutions. *The Journal of Chemical Physics*, 130(11):114903, 2009. doi: http://dx.doi.org/10.1063/1.3088849. URL http://scitation.aip.org/content/aip/journal/jcp/130/11/10.1063/1.3088849.

[159] Ludovic Berthier and Robert L. Jack. Structure and dynamics of glass formers: Predictability at large length scales. *Phys. Rev. E*, 76:041509, Oct 2007. doi: 10.1103/PhysRevE.76.041509. URL http://link.aps.org/doi/10.1103/PhysRevE.76.041509.

[160] Swagata Pahari, Chandan Kumar Choudhury, Prithvi Raj Pandey, Minal More, Arun Venkatnathan, and Sudip Roy. Molecular dynamics simulation of phosphoric acid doped monomer of polybenzimidazole: a potential component polymer electrolyte membrane of fuel cell. *J. Phys. Chem. B*, 116(24):7357–7366, 2012.

[161] Stéphane AH Spieser, Bas R Leeflang, Loes MJ Kroon-Batenburg, and Jan Kroon. A force field for phosphoric acid: comparison of simulated with experimental data in the solid and liquid state. *J. Phys. Chem. A*, 104(31):7333–7338, 2000.

[162] Hossein Ali Karimi-Varzaneh, Florian Muller-Plathe, Sundaram Balasubramanian, and Paola Carbone. Studying long-time dynamics of imidazolium-based ionic liquids with a systematically coarse-grained model. *Phys. Chem. Chem. Phys.*, 12: 4714–4724, 2010. doi: 10.1039/B925780B. URL http://dx.doi.org/10.1039/B925780B.

[163] Li Qingfeng, Hans A Hjuler, and Niels J Bjerrum. Oxygen reduction on carbon supported platinum catalysts in high temperature polymer electrolytes. *Electrochim. Acta*, 45(25):4219–4226, 2000.

[164] David Aili, Lars N Cleemann, Qingfeng Li, Jens Oluf Jensen, Erik Christensen, and Niels J Bjerrum. Thermal curing of pbi membranes for high temperature pem fuel cells. *J. Mater. Chem.*, 22(12):5444–5453, 2012.

[165] Miaomiao Han, Gang Zhang, Zhongguo Liu, Shuang Wang, Mingyu Li, Jing Zhu, Hongtao Li, Yang Zhang, Christopher M Lew, and Hui Na. Cross-linked polybenzimidazole with enhanced stability for high temperature proton exchange membrane fuel cells. *J. Mater. Chem.*, 21(7):2187–2193, 2011.

[166] Juan Antonio Asensio, Salvador Borrós, and Pedro Gómez-Romero. Enhanced conductivity in polyanion-containing polybenzimidazoles. improved materials for

proton-exchange membranes and pem fuel cells. *Electrochem. Commun.*, 5(11): 967–972, 11 2003. doi: http://dx.doi.org/10.1016/j.elecom.2003.09.007. URL http://www.sciencedirect.com/science/article/pii/S1388248103002492.

[167] Juan Antonio Asensio, Salvador Borrós, and Pedro Gómez-Romero. Proton-conducting polymers based on benzimidazoles and sulfonated benzimidazoles. *J. Polym. Sci., Part A: Polym. Chem.*, 40(21):3703–3710, 2002.

[168] J-T Wang, RF Savinell, J Wainright, M Litt, and H Yu. A h2o2 fuel cell using acid doped polybenzimidazole as polymer electrolyte. *Electrochim. Acta*, 41(2): 193–197, 1996.

[169] Juan Antonio Asensio, Salvador Borrós, and Pedro Gómez-Romero. Proton-conducting membranes based on poly (2, 5-benzimidazole)(abpbi) and phosphoric acid prepared by direct acid casting. *J. Membr. Sci.*, 241(1):89–93, 2004.

[170] Suwen Wang, Feilong Dong, and Zhongfang Li. Proton-conducting membrane preparation based on sio2-riveted phosphotungstic acid and poly (2, 5-benzimidazole) via direct casting method and its durability. *Journal of Materials Science*, 47(11):4743–4749, 2012.

[171] Liliana A Diaz, Graciela C Abuin, and Horacio R Corti. Water and phosphoric acid uptake of poly [2, 5-benzimidazole](abpbi) membranes prepared by low and high temperature casting. *J. Power Sources*, 188(1):45–50, 2009.

[172] Patrick E Cassidy. *Thermally stable polymers, synthesis and properties*. Marcel Dekker, 1980.

[173] Santosh C Kumbharkar and Ulhas K Kharul. New n-substituted abpbi: Synthesis and evaluation of gas permeation properties. *J. Membr. Sci.*, 360(1):418–425, 2010.

[174] SR Samms, S Wasmus, and RF Savinell. Thermal stability of proton conducting acid doped polybenzimidazole in simulated fuel cell environments. *J. Electrochem. Soc.*, 143(4):1225–1232, 1996.

[175] Minal More, Swagata Pahari, Sudip Roy, and Arun Venkatnathan. Characterization of the structures and dynamics of phosphoric acid doped benzimidazole mixtures: a molecular dynamics study. *J. Mol. Model.*, 19(1):109–118, 2013.

[176] Swagata Pahari and Sudip Roy. Evidence and characterization of dynamic heterogeneity in binary mixtures of phosphoric acid and benzimidazole. *J. Chem. Phys.*, 139(15):154701, 2013.

[177] Rupesh S Bhavsar, Sandip B Nahire, Mrunali S Kale, Shubhangi G Patil, Pradnya P Aher, Ritesh A Bhavsar, and Ulhas K Kharul. Polybenzimidazoles based on 3, 3-diaminobenzidine and aliphatic dicarboxylic acids: Synthesis and evaluation of physicochemical properties toward their applicability as proton exchange and gas separation membrane material. *J. Appl. Polym. Sci.*, 120(2):1090–1099, 2011.

[178] Shuo Li, J R Fried, John Colebrook, and Jonathan Burkhardt. Molecular Simulations of Neat, Hydrated, and Phosphoric Acid-Doped Polybenzimidazoles. Part 1: Poly (2, 2-M-Phenylene-5, 5-Bibenzimidazole)(PBI), Poly (2, 5-Benzimidazole)(ABPBI), and Poly (p-Phenylene Benzobisimidazole)(PBDI). *Polymer*, 51(23):5640–5648, 2010.

[179] W-F Hwang, DR Wiff, C Verschoore, GE Price, TE Helminiak, and WW Adams. Solution processing and properties of molecular composite fibers and films. *Polym. Eng. Sci.*, 23(14):784–788, 1983.

[180] M F H Schuster, W H Meyer, M Schuster, and K D Kreuer. Toward a New Type of Anhydrous Organic Proton Conductor Based on Immobilized Imidazole. *Chem. Mater.*, 16(2):329–337, 2004. doi: 10.1021/cm021298q. URL http://dx.doi.org/10.1021/cm021298q.

[181] W Münch, K. D Kreuer, W Silvestri, J Maier, and G Seifert. The diffusion mechanism of an excess proton in imidazole molecule chains: first results of an ab initio molecular dynamics study. *Solid State Ionics*, 145(1–4):437–443, 12 2001. doi: http://dx.doi.org/10.1016/S0167-2738(01)00941-9. URL http://www.sciencedirect.com/science/article/pii/S0167273801009419.

[182] A Kawada, A R McGhie, and M M Labes. Protonic Conductivity in Imidazole Single Crystal. *J. Chem. Phys.*, 52(6):3121–3125, 1970.

[183] K D Kreuer, A Fuchs, M Ise, M Spaeth, and J Maier. Imidazole and Pyrazole-Based Proton Conducting Polymers and Liquids. *Electrochim. Acta*, 43(10–11):1281–1288, 1998. ISSN 0013-4686. doi: http://dx.doi.org/10.1016/S0013-4686(97)10031-7. URL http://www.sciencedirect.com/science/article/pii/S0013468697100317.

[184] Meilin Liu, Zhen Zhou, Siwen Li, Yuelan Zhang, and Wen Li. Recent Development in Heterocycles-Based Proton Exchange Membranes (PEMs). *Meeting Abstracts*, MA2006-01(24):849, 2006. URL http://ma.ecsdl.org/content/MA2006-01/24/849.abstract.

[185] Siwen Li, Zhen Zhou, Yuelan Zhang, Meilin Liu, and Wen Li. 1H-1,2,4-Triazole: An Effective Solvent for Proton-Conducting Electrolytes. *Chem. Mater.*, 17(24):

5884–5886, 2005. doi: 10.1021/cm0515092. URL http://dx.doi.org/10.1021/cm0515092.

[186] Manoj V Mane, Arun Venkatnathan, Kamalika Ghatak, and Kumar Vanka. Exploring the Potential of Doped Zero-Dimensional Cages for Proton Transfer in Fuel Cells: A Computational Study. *J. Phys. Chem. B*, 116(32):9803–9811, 2012. doi: 10.1021/jp303884p. URL http://dx.doi.org/10.1021/jp303884p.

[187] Guntram Rauhut. Modulation of Reaction Barriers by Generating Reactive Intermediates: Double Proton Transfer Reactions. *Phys. Chem. Chem. Phys.*, 5 (5):791–800, 2003. doi: 10.1039/B208960B. URL http://dx.doi.org/10.1039/B208960B.

[188] Javier Catalan and Jose Elguero. Basicity and Acidity of Azoles. volume 41 of *Advances in Heterocyclic Chemistry*, pages 187–274. Academic Press, 1987. doi: http://dx.doi.org/10.1016/S0065-2725(08)60162-2. URL http://www.sciencedirect.com/science/article/pii/S0065272508601622.

[189] Zhen Zhou, Siwen Li, Yuelan Zhang, Meilin Liu, and Wen Li. Promotion of Proton Conduction in Polymer Electrolyte Membranes by 1H-1,2,3-Triazole. *J. Am. Chem. Soc.*, 127(31):10824–10825, 2005. doi: 10.1021/ja052280u. URL http://dx.doi.org/10.1021/ja052280u.

[190] Surangkhana Martwiset, Richard C Woudenberg, Sergio Granados-Focil, Ozgur Yavuzcetin, Mark T Tuominen, and E Bryan Coughlin. Intrinsically Conducting Polymers and Copolymers Containing Triazole Moieties. *Solid State Ionics*, 178(23–24):1398–1403, 2007. ISSN 0167-2738. doi: http://dx.doi.org/10.1016/j.ssi.2007.07.005. URL http://www.sciencedirect.com/science/article/pii/S0167273807002354.

[191] Sergio Granados-Focil, Richard C Woudenberg, Ozgur Yavuzcetin, Mark T Tuominen, and E Bryan Coughlin. Water-Free Proton-Conducting Polysiloxanes: A Study on the Effect of Heterocycle Structure. *Macromolecules*, 40(24):8708–8713, 2007. doi: 10.1021/ma071715q. URL http://dx.doi.org/10.1021/ma071715q.

[192] R A Potrekar, M P Kulkarni, R A Kulkarni, and S P Vernekar. Polybenzimidazoles Tethered with N-Phenyl 1,2,4-Triazole Units as Polymer Electrolytes for Fuel Cells. *J. Polym. Sci., Part A: Polym. Chem.*, 47(9):2289–2303, 2009. ISSN 1099-0518. doi: 10.1002/pola.23310. URL http://dx.doi.org/10.1002/pola.23310.

[193] Sevim Ünügür Çelik, Ayhan Bozkurt, and Seyed Saeid Hosseini. Alternatives toward proton conductive anhydrous membranes for fuel

cells: Heterocyclic protogenic solvents comprising polymer electrolytes. *Progress in Polymer Science*, 37(9):1265–1291, 9 2012. doi: http://dx.doi.org/10.1016/j.progpolymsci.2011.11.006. URL http://www.sciencedirect.com/science/article/pii/S0079670011001316.

[194] Mousumi Hazarika and Tushar Jana. Proton Exchange Membrane Developed from Novel Blends of Polybenzimidazole and Poly(vinyl-1,2,4-Triazole). *ACS Appl. Mater. Interfaces*, 4(10):5256–5265, 2012. doi: 10.1021/am301185b. URL http://dx.doi.org/10.1021/am301185b.

[195] Mariela L Ponce, Dominique Gomes, and Suzana P Nunes. One-Pot Synthesis of High Molecular Weight Sulfonated Poly(oxadiazole-triazole) Copolymers for Proton Conductive Membranes. *J. Membr. Sci.*, 319(1-2):14–22, July 2008. ISSN 0376-7388. doi: 10.1016/j.memsci.2008.03.031.

[196] M L Ponce, M Boaventura, D Gomes, A Mendes, L M Madeira, and S P Nunes. Proton Conducting Membranes Based on Benzimiclazole Sulfonic Acid Doped Sulfonated Poly(oxadiazole-Triazole) Copolymer for Low Humidity Operation. *Fuel Cells*, 8(3-4):209–216, July 2008. ISSN 1615-6846. doi: 10.1002/fuce.200800012.

[197] *CPMD, Version 3.13*. Max-Planck-Institut für Festkörperforschung and IBM Zurich Research Laboratory, 2010.

[198] Berk Hess, Carsten Kutzner, David van der Spoel, and Erik Lindahl. GROMACS 4: Algorithms for Highly Efficient, Load-Balanced, and Scalable Molecular Simulation. *J. Chem. Theory Comput.*, 4(3):435–447, 2008. doi: 10.1021/ct700301q. URL http://pubs.acs.org/doi/abs/10.1021/ct700301q.

[199] David Van Der Spoel, Erik Lindahl, Berk Hess, Gerrit Groenhof, Alan E Mark, and Herman J C Berendsen. GROMACS: Fast, Flexible, and Free. *J. Comput. Chem.*, 26(16):1701–1718, 2005. ISSN 1096-987X. doi: 10.1002/jcc.20291. URL http://dx.doi.org/10.1002/jcc.20291.

[200] Michael Meot-Ner, Joel F Liebman, and Janet E Del Bene. Proton Affinities of Azoles: Experimental and Theoretical Studies. *J. Org. Chem.*, 51(7):1105–1110, 1986. doi: 10.1021/jo00357a031. URL http://dx.doi.org/10.1021/jo00357a031.

[201] R Subbaraman, H Ghassemi, and T Zawodzinski Jr. Triazole and Triazole Derivatives As Proton Transport Facilitators in Polymer Electrolyte Membrane Fuel Cells. *Solid State Ionics*, 180(20–22):1143–1150, 2009. ISSN 0167-2738. doi: http://dx.doi.org/10.1016/j.ssi.2009.05.018. URL http://www.sciencedirect.com/science/article/pii/S0167273809001878.

[202] Linas Vilciauskas, Stephen J Paddison, and Klaus-Dieter Kreuer. Ab Initio Modeling of Proton Transfer in Phosphoric Acid Clusters. *J. Phys. Chem. A*, 113(32): 9193–9201, 2009. doi: 10.1021/jp903005r. URL http://dx.doi.org/10.1021/jp903005r.

[203] M J Frisch, G W Trucks, H B Schlegel, G E Scuseria, M A Robb, J R Cheeseman, G Scalmani, V Barone, B Mennucci, G A Petersson, H Nakatsuji, M Caricato, X Li, H P Hratchian, A F Izmaylov, J Bloino, G Zheng, J L Sonnenberg, M Hada, M Ehara, K Toyota, R Fukuda, J Hasegawa, M Ishida, T Nakajima, Y Honda, O Kitao, H Nakai, T Vreven, J A Montgomery Jr., J E Peralta, F Ogliaro, M Bearpark, J J Heyd, E Brothers, K N Kudin, V N Staroverov, R Kobayashi, J Normand, K Raghavachari, A Rendell, J C Burant, S S Iyengar, J Tomasi, M Cossi, N Rega, J M Millam, M Klene, J E Knox, J B Cross, V Bakken, C Adamo, J Jaramillo, R Gomperts, R E Stratmann, O Yazyev, A J Austin, R Cammi, C Pomelli, J W Ochterski, R L Martin, K Morokuma, V G Zakrzewski, G A Voth, P Salvador, J J Dannenberg, S Dapprich, A D Daniels, Ö Farkas, J B Foresman, J V Ortiz, J Cioslowski, and D J Fox. Gaussian09 {R}evision {D}.01, 2009.

Publications

1. Evidence and characterization of dynamic heterogeneity in binary mixtures of phosphoric Acid and benzimidazole, **S. Pahari**, and S. Roy*, J. Chem. Phys, 139, 154701-154706 (2013).

2. Characterization of structure and dynamics of phosphoric acid doped benzimidazole mixtures: a molecular dynamics study, M. More, **S. Pahari**, and S. Roy, and A. Venkatanathan*, J. Mol. Model, 19, 109 - 118 (2013).

3. Molecular dynamics simulation of phosphoric acid doped monomer of polybenzimidazole:a potential component of polymer electrolyte membrane of fuel cell, **S. Pahari**, C. K. Choudhury, P. R. Pandey, M. More, A. Venkatanathan, and S. Roy*, J. Phys. Chem B, 116, 7357-7366 (2012).

4. Proton transport mechanism of imidazole, triazole and phosphoric acid mixtures from *ab initio* molecular dynamics simulations, **S. Pahari***, and S. Roy* (communicated).

5. Conformational and structural properties of PA doped Polybenzimidazoles: A polyelectrolyte membrane for fuel cell, **S. Pahari***, and S. Roy* (communicated).

6. Quantum chemical investigation on proton transfar in Phosphoric acid doped N-containing heterocyclic compounds for designing potential membrane materials for fuel cell S. Biswas, S. Roy, and **S. Pahari*** (manuscript in preparation).

7. The polymer force field: Development and parameterization of forcefield parameters for polymers-I, C. K. Choudhury, S. Chakraborty, **S. Pahari**, S. Biswas, and S. Roy* (manuscript in preparation).